# Wiring up pre-characterized single nitrogen-vacancy centers in nanodiamonds by 3D laser lithography

Zur Erlangung des akademischen Grades eines

DOKTORS DER NATURWISSENSCHAFTEN

von der Fakultät für Physik des

Karlsruher Instituts für Technologie (KIT)

genehmigte
Dissertation

von

M.Sc. Qiang Shi

| | |
|---|---|
| Tag der mündlichen Prüfung: | 30.6.2017 |
| Referent: | Prof. Dr. Martin Wegener |
| Korreferent: | Prof. Dr. Carsten Rockstuhl |

# Abbreviations

| | |
|---|---|
| NV | nitrogen-vacancy |
| ND | nanodiamond |
| HBT | Hanbury-Brown and Twiss |
| DLW | direct laser writing |
| STED | stimulated emission depletion |
| ODMR | optically detected magnetic resonance |
| ESR | electronic-spin-resonant |
| AFM | atomic force microscope |
| 2PA | two-photon absorption |
| 1PA | one-photon absorption |
| PETA | pentaerythritol triacrylate |
| PETTA | pentaerythritol tetraacrylate |
| TMPTA | trimethylolpropane triacrylate |
| PDMS | polydimethylsiloxane |
| DETC | 7-diethylamino-3-thenoylcoumarin |
| cw | continuous-wave |
| NA | numerical aperture |
| EMCCD | electron multiplying charge coupled device |
| APD | avalanche photodiode |
| CCD | charge coupled device |
| PDMD | polarization-dependent fluorescence intensity modulation depth |

# 1. Introduction

Since the beginning of the twentieth century, the emerging of the quantum mechanics theory [1] has changed the concept of light at a fundamental level. Photons are found to be capable of being on-demand generated and manipulated with high precision and predictions [2], and carrying information with much higher speed than electronic devices. In the future, optical and photonic devices are expected to have higher performance and possess potentials in wide fields and even to replace the electronic counterparts.

To date, the theory of quantum mechanics has heavily extended the scope of the property of objects and made it possible to clarify what was hard to be understood with the classical theory, such as instantaneously connecting two separate objects with quantum entanglement [3] and superposition of a single object. Harnessing quantum properties of a system such as manipulating quantum bits of a single photon has a promising implementation for information storing and processing [4]. With the method of the quantum key distribution, information can be exchanged in a more secret and secure manner [4]. The greatly exciting innovation of quantum computer [5], which is believed to perform much faster than the classical computer alone with the quantum algorithms [6], can be achieved. It provides solutions to problems that are not able to be solved by the classical computer. Moreover, quantum theory extends the ability of people to describe a physical system with much higher resolution, sensitivity, and accuracy such as phase measurements with trapped ions [7], magnetometry with cold atomic ensembles [8-10], which is called quantum metrology [11].

To practically enjoy the benefits of quantum, especially the quantum optical, technology, crucial requirements have to be fulfilled. Ideally, the generation of single photons should be on demand with high quantum efficiency and certain initial states. Additionally, optical components such as mirrors, beam splitters, detectors, and fibers in the macroscopic world are required to be built and aligned in the form of their counterparts in the quantum mechanical world. The development of lithography techniques has realized fabrication of micro-scale quantum-photonic components [12-15]. However, building a three-dimensional (3D) hybrid system that contains single-photon sources and the on-demand-fabricated quantum-photonic components is still a remaining task.

This thesis deals with the implementation problem of combining hybrid quantum-photonic components with well-characterized single-photon sources. The method and experiments presented in this work exhibit high fabrication yield and photon collection efficiency due to the optimized working procedure. The single-photon sources are spatially fixed and pre-characterized which enables on-demand fabrication of quantum-photonic components with individual coupling.

In Chapter 2, the concept of photons with the quantum mechanical theory is introduced. This concept is used throughout the whole thesis. The definition of single photons and the single-photon source is explained starting from the photon distribution statistic and the indistinguishability of photons, followed by the types of single-photon sources. In the experimental point of view, the detection scheme of single-photon emission is shown. Specifically, the NV center in nanodiamonds (NDs) is introduced as the single-photon source used in this work. Besides, the commonly used method for 3D mapping of emitters, the laser scanning confocal fluorescence microscope, is introduced. Afterwards, direct laser writing (DLW) technique enables fabrication of nearly arbitrarily shaped 3D structures is demonstrated.

Chapter 3 demonstrates the integrated setup for fabrication of 3D quantum components with pre-characterized single NV centers at desired positions. The method to combine and align the laser scanning confocal fluorescence microscope with the DLW technique is demonstrated. This integrated setup offers ultra-high accuracy to on-demand integrate single-photon sources to the quantum components. Exemplary experiments of characterizing NV centers in photoresist, including 3D localization of NV center, the second-order correlation measurement, photoluminescence (PL) saturation measurement and the determination of NV center dipole orientations, are demonstrated.

Chapter 4 solves a fundamental problem of the background fluorescence from the polymer structure where single-photon emitters are embedded. The background signal is a killer for the single-photon emission and is heavily impeding the practical application of the single-photon source [16-17]. Here, a recipe of a photoresist showing low background fluorescence intensity both before and after being polymerized is achieved.

Chapter 5 shows a hybrid micro-antenna with improved capability to efficiently collect single photons from embedded single NV centers by its functionality of redistribution of the emission pattern. However, a problem arises in the structure. The background fluorescence influences the characterization of detected single-photon emission, and the redistribution of emission pattern restricts the collection efficiency in the confocal scheme. Another design with the hemispherical shape hybrid antenna is demonstrated later in this chapter, which exhibits both improved collection efficiency of single NV centers and low background level under confocal detection scheme.

In Chapter 6, experiments of integrating well-aligned laser-written polymer waveguides to quantum-components fabricated by another platform with embedded single-photon sources are demonstrated. In the first experiment, the pre-fabricated $Si_3N_4$ waveguides are interconnected by a laser written polymer waveguide. Within the polymer waveguide, a single NV center is embedded on-demand. A similar method is used to couple NV centers into the tapered fiber in the later experiment. In both experiments, post-characterization of NV centers show distinct single-photon emission.

In Chapter 7, functional laser-written quantum-photonic components are introduced. In a particular design, single-photon emission from an embedded single NV center is effectively guided and collected from the structure and the design realizes on-chip photon stream splitting and background fluorescence filtering. The other structure acting as an integrated single-photon source network wires up more than one single NV centers and offers multiple inputs and outputs for selectively pumping individual NV centers and collecting single photons.

In the last chapter, Chapter 8, the experiments and techniques in this work is reviewed and a brief outlook is given.

# 2. Fundamentals

This work aims at a method to access single-photon sources with laser written microstructures. The scope of this work involves some fundamental concepts that are not frequently used in our daily life. Thus, this thesis starts with the introduction of them and the explaining why they are important in our point of view.

## 2.1. Single photons

What is a photon? A photon is an elementary excitation of a single mode of the quantized electromagnetic field [18]. Originally, the word "photon" refers to light. In 1900, the father of the quantum physics, Max Planck introduced energy quanta to describe the radiation of a blackbody. In 1905, the concept of light quantum (German: das Lichtquant) was adopted by Einstein to explain the photoelectric effect [19-21], which makes the application of solar power possible. In 1916, the American physicist Leonard T. Troland created the word *photon*. In short, photons are the fundamental particles of light with a unique property that they are both wave and particle. Unlike other elementary particles, photons have some characteristics specifying themselves:

- They travel with a constant velocity of $c = 2.9979\times10^8\ \mathrm{m/s}$ in vacuum.
- They have no rest mass and electric charge.
- They can interact as particles with electrons and other particles, such as Compton effect.
- They can interfere with themselves.
- They carry discrete amounts of energy and momentum according to

$$E = hv,$$

$$p = \frac{h}{\lambda}, \tag{2.1.1}$$

where $h$ is Planck`s constant, $v$ is the frequency of the light and $\lambda$ is wavelength.

The introduction of photons is an extension to the classical theory of electrodynamics and opens the door to the quantum physics. Although the classical theories can be used to explain many phenomena in electrodynamics, the introduction of quantum physics can explain more subtle effects such as photon anti-bunching (see section 2.1.2), electron-positron annihilation effect and the photoelectric effect.

### 2.1.1. Photon Statistics

Generally, the number of particles in a given system is assumed to be a fixed number. This assumption is valid for particles with non-zero mass and breaks down for photons. When counting photons, the average count rate is determined by the light intensity but the photon number distributions depend on the photon source. The photon probability distribution describes how a light source emits photons. According to such statistics, photon sources can be divided into three categories, namely thermal light sources, coherent light sources and single-photon sources.

The world people see in our daily life is generally lightened by photons from thermal or chaotic light sources such as the sun or light bulbs. Thermal light sources, as the name implies, create photons by a thermal process, in which many tightly packed atoms are emitting photons independently. Each excited atom returns to a lower energy state and emits one photon with some certain energy. For a thermal light source, the probability distribution for the detection of $n$ photons $p(n)$ in a certain time period follows the Bose-Einstein distribution [22-24]:

$$p(n) = \frac{\bar{n}^n}{(1+\bar{n})^{(1+n)}}, \tag{2.1.2}$$

where $\bar{n}$ is the average photon number in the certain time period.

Lasers, on the contrary, produce photons in a more uniform way in space and time. The emitted photons possess the same wavelength and a defined phase relationship. The photon number for the coherent photon state distribution follows a Poisson distribution [22-23]:

$$p(n) = \frac{\bar{n}^n e^{-\bar{n}}}{n!}. \tag{2.1.3}$$

Photons from thermal sources like an incandescent light bulb prefer to propagate in groups and the temporal fluctuation is large. Whereas, the coherent photon state from lasers fluctuates less with random spacing. These lead to a lack of ability of experimentally inspecting at the single photon level. The production of photon streams, in which the photons are completely separated, is crucial for quantum information processing especially in the field of the quantum photonic. Such a non-classical photon state is called a single-photon state (Figure 2.1). Unlike the classical light states, it possesses extraordinary properties that can be well explained by the quantum theory. A more quantitative description of photon sources will be given in the following sections.

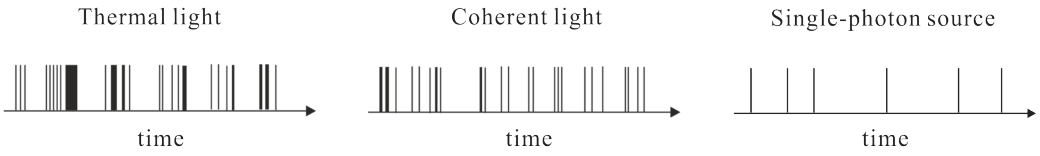


**Figure 2.1 Photon-arrival distribution as a function of time** for thermal light, coherent light and single-photon source.

## 2.1.2. Correlation functions

Studying the behavior of photons, one may specify the problem: if one has detected one photon at time $t_0$, how likely is it to detect another photon at time $t_0 + t$? It should be known if there is any correlation between the two successive photons. To answer this question, it is necessary to introduce the concepts of first- and second-order correlation functions.

**First-order correlation functions:**

To understand the first-order correlation, one can take a close look at Young`s double slit experiment. If a coherent (the degree of correlation between two or more light sources can be quantified by the concept of coherence) light source illuminates two slits, an interference fringe pattern emerges at the image screen behind it. The electric field at position $r_1$ and time $t_1$ is denoted by $\vec{E}(r_1, t_1)$. Thus, the superposition electric fields $\vec{E}(r, t)$ at time $t$ given by the propagation distance from the two slits $r_1$ and $r_2$ to the given point $r$ on the screen, can be expressed as:

$$\vec{E}(r, t) = \vec{E}_1(r_1, t_1) + \vec{E}_2(r_2, t_2). \tag{2.1.4}$$

And the measured intensity of the electric field is:

$$\langle I(r, t)\rangle \propto \langle \left|\vec{E}(r, t)\right|^2 \rangle = \langle \left|\vec{E}_1(r_1, t_1)\right|^2 \rangle + \langle \left|\vec{E}_2(r_2, t_2)\right|^2 \rangle \tag{2.1.5}$$

$$+2Re[\langle E_1^*(r_1, t_1) E_2(r_2, t_2)\rangle],$$

where $\langle \vec{E} \rangle$ indicates the time average of a measured electric field. The first two terms represent the unrelated intensities from the two slits whereas the third term corresponds to the correlation of the electric fields from two slits and hence, determines the visibility of the fringes. The normalized third term is called the first-order correlation function

$g^{(1)}(r_1, r_2, \tau)$, where $\tau$ is the time difference between $t_1$ and $t_2$:

$$g^{(1)}(r_1, r_2, \tau) = \frac{\langle E_1^*(r_1, t) E_2(r_2, t+\tau)\rangle}{\langle E_1^*(r_1, t)\rangle \langle E_2(r_2, t+\tau)\rangle}. \tag{2.1.6}$$

The situation can be simplified either by performing the measurement at the same time i.e. $\tau = 0$, or by measuring the two fields at different times but at the same position i.e. $r_1 = r_2$. In the former case, one gets the spatial first-order correlation function: $g^{(1)}(r_1, r_2, \tau) = g^{(1)}(r_1, r_1)$, while in the latter case, the temporal first-order correlation function is obtained: $g^{(1)}(r_1, r_2, \tau) = g^{(1)}(\tau)$.

The physical meaning of the first-order correlation function can be understood by defining the visibility of the interference fringes：

$$\mathrm{V} = \frac{I_{max} - I_{min}}{I_{max} + I_{min}}. \tag{2.1.7}$$

Given fixing light sources, according to equation (2.1.5) and equation (2.1.7), the visible intensity of the interference fringe pattern varies in the range between $\pm 2|\langle E_1^*(r_1, t) E_2(r_2, t+\tau)\rangle|$ which corresponds to the definition of the first-order correlation. Therefore,

$$\mathrm{V} \propto \left| g^{(1)}(r_1, r_2, \tau) \right|, \tag{2.1.8}$$

i.e. the visibility of the fringes is proportional to the magnitude of the first-order correlation function. The visibility takes values in the range from $0$ to $1$. A value of $0$ corresponds to an incoherent light. A value of $1$ corresponds to a coherent light. For values between $0$ and $1$, the light is said to be partially coherent. In a sense, the first-order correlation function is a quantity describing how well one can predict the phase at space-time point B, given one knows the phase at a space-time point A.

For a coherent light source such as a laser, emitted light has predictable phase relations. Therefore, the first-order correlation function has a constant magnitude. For a thermal light source, the magnitude of the first-order correlation function decreases when the time separation of photons is far to approach the coherence time.

The concept of the first-order correlation of light has been introduced above. However, it is not sufficient to describe all light behavior because the description of the first-order correlation, $E_1^*(r_1, t) E_2(r_2, t+\tau)$, relies on the phase relation. What is a useful measure if phase information cannot be simply integrated to a certain form?

**Classical point of view:**

The first-order correlation function describes the correlation of two fields. Similarly, one can define the correlated intensities of two fields by the intensity correlation function:

$$g^{(2)}(r_1, r_2, \tau) = \frac{\langle E^*(r_1,t)E^*(r_2,t+\tau)E(r_2,t+\tau)E(r_1,t)\rangle}{\langle E^*(r_1,t)E(r_1,t)\rangle\langle E^*(r_2,t+\tau)E(r_2,t+\tau)\rangle}$$

$$= \frac{\langle I(r_1,t)I(r_2,t+\tau)\rangle}{\langle I(r_1,t)\rangle\langle I(r_2,t+\tau)\rangle}. \quad (2.1.9)$$

Analogous to the spatial first-order correlation function, the temporal second-order correlation function can be written as:

$$g^{(2)}(\tau) = \frac{\langle I(t)I(t+\tau)\rangle}{\langle I(t)\rangle\langle I(t+\tau)\rangle}. \quad (2.1.10)$$

From the experimental viewpoint, the intensity is proportional to the number of photon counts $n(t)$ registered by a detector. Thus, $g^{(2)}(\tau)$ can be written as:

$$g^{(2)}(\tau) = \frac{\langle n(t)n(t+\tau)\rangle}{\langle n(t)\rangle\langle n(t+\tau)\rangle}. \quad (2.1.11)$$

The physical meaning of equation (2.1.11) answers the following question: if one detects $n$ photon(s) at time $t$, what is the probability of detecting another $n$ photon(s) after a time interval $\tau$?

One can assume that a classical light source has a constant average intensity with $\langle I(t)\rangle = \langle I(t+\tau)\rangle$, then, equation (2.1.10) is reduced to

$$g^{(2)}(\tau) = \frac{\langle I(t)I(t+\tau)\rangle}{\langle I(t)\rangle\langle I(t+\tau)\rangle} = \frac{\langle I(t)I(t+\tau)\rangle}{\langle I(t)\rangle^2}. \quad (2.1.12)$$

With a zero-time delay, one can get:

$$g^{(2)}(0) = \frac{\langle I^2(t)\rangle}{\langle I(t)\rangle^2}. \quad (2.1.13)$$

For a classical light source, the expression can be expressed by the intensity as the sum of its constant average $I_0$ and an instantaneous fluctuation term $\Delta I(t)$:

$$I(t) = I_0 + \Delta I(t). \quad (2.1.14)$$

If the detector detects a photon event, the fluctuation term tells us the probability to detects additional events at time $t$. For a positive $\Delta I(t)$, an increasing chance to see another photon is expected, while on the contrary, a negative $\Delta I(t)$ indicates a decreased probability. One can derive from equation (2.1.14) and equation (2.1.15):

$$g^{(2)}(0) = \frac{\langle I^2(t)\rangle}{\langle I(t)\rangle^2} = \frac{\langle [I_0 + \Delta I(t)]^2\rangle}{\langle I(t)\rangle^2} \geq \frac{[\langle I_0\rangle^2 + \langle \Delta I(t)\rangle^2]}{\langle I(t)\rangle^2}. \qquad (2.1.15)$$

Again, for a classical light source, the light intensity is constant $\langle I(t)\rangle^2 = \langle I_0\rangle^2$, and thus equation (2.1.15) reduces to:

$$g_{classical}{}^{(2)}(0) \geq \frac{[\langle I_0\rangle^2 + \langle \Delta I(t)\rangle^2]}{\langle I(t)\rangle^2} = 1 + \frac{\langle \Delta I(t)\rangle^2}{\langle I(t)\rangle^2} \geq 1. \qquad (2.1.16)$$

Moreover, for $N$ times measurements,

$$\langle I(t)I(t+\tau)\rangle^2 = \frac{[I(t_1)I(t_1+\tau)+\cdots+I(t_N)I(t_N+\tau)]^2}{N^2}, \text{ and} \qquad (2.1.17)$$

$$\langle I(t)^2\rangle\langle I(t+\tau)^2\rangle = [I(t_1)^2 + \cdots + I(t_N)^2] \cdot$$

$$[I(t_1+\tau)^2 + \cdots + I(t_N+\tau)^2] \cdot \frac{1}{N^2}.$$

Using equation (2.1.12) and Cauchy's inequality [27], one can get:

$$\langle {I_1}^2\rangle\langle {I_2}^2\rangle \geq \langle I_1 I_2\rangle^2. \qquad (2.1.18)$$

One can derive a relation between $g^{(2)}(0)$ and $g^{(2)}(\tau)$ if replacing the corresponding items to equation (2.1.12):

$$g_{classical}{}^{(2)}(0) \geq g_{classical}{}^{(2)}(\tau). \qquad (2.1.19)$$

This means that for a classical light source, the probability of detecting a second photon immediately after the first one is larger than or equal to the probability of a detection at a later time. In other words, photons prefer to arrive together. This is photon bunching.

For coherent light, such as a laser beam, the average intensity fluctuation is zero, i.e. $\langle \Delta I(t)\rangle = 0$. Hence

$$\langle I(t)I(t+\tau)\rangle = \langle\big(\langle I\rangle + \Delta I(t)\big)\big(\langle I\rangle + \Delta I(t+\tau)\big)\rangle$$
$$= \langle\langle I\rangle^2 + \Delta I(t)\langle I\rangle + \langle I\rangle\Delta I(t+\tau) + \Delta I(t)\Delta I(t+\tau)\rangle$$
$$= \langle I\rangle^2\langle I\rangle^2\langle I\rangle^2\langle\langle I\rangle^2 + \Delta I(t)\langle I\rangle + \langle I\rangle\Delta I(t+\tau) + \Delta I(t)\Delta I(t+\tau)\rangle$$
$$= \langle I\rangle^2. \qquad (2.1.20)$$

Therefore, from equation (2.1.12) one can get:

$$g_{coherent}{}^{(2)}(\tau) = \frac{\langle I(t)\rangle^2}{\langle I(t)\rangle^2} = 1. \qquad (2.1.21)$$

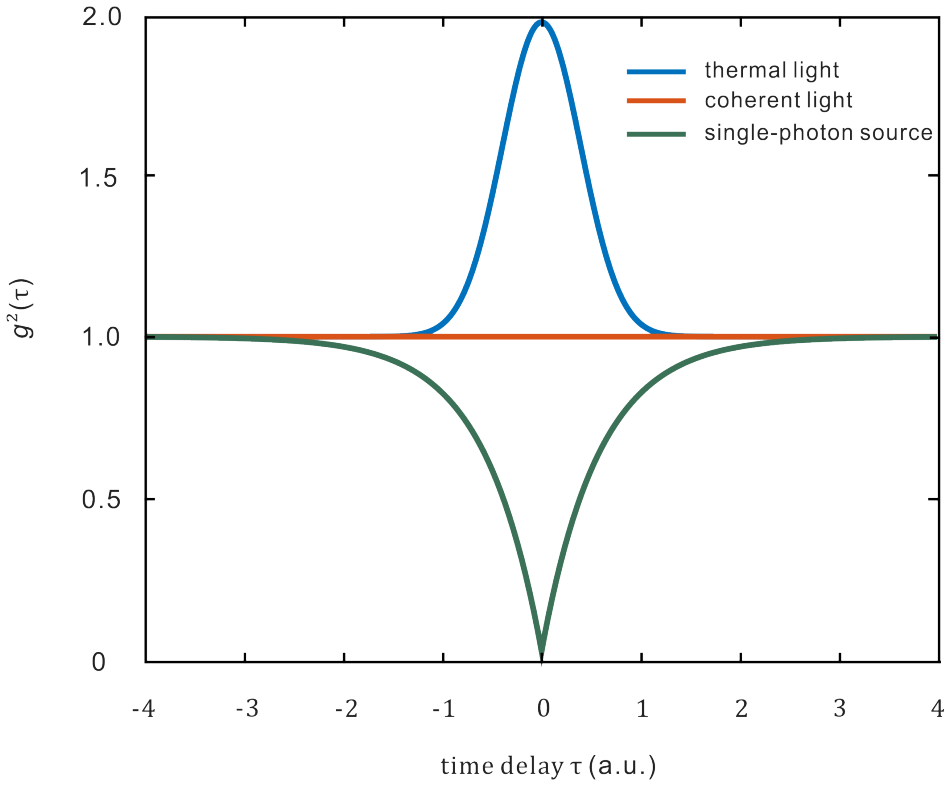


**Figure 2.2 Second-order correlation function $g^2(\tau)$ for three kinds of light sources**: thermal light sources like incandescent light bulbs (blue), coherent light sources like lasers (red) and perfect single photon sources (green).

**Quantum theory:**

From equation (2.1.16), it is known that for a classical light source, $g_{classical}{}^{(2)}(0) \geq 1$. The special case of $g^{(2)}(0) < 1$, photon anti-bunching effect could also takes place and be explained. In 1977, H.J. Kimble and his colleagues were the first to measure anti-bunching effect. They studied the resonance fluorescence from Na atoms excited by a dye-laser beam [28]. This anti-bunching phenomenon cannot be explained by the

previously described classical point of view. However, using quantum theory, this phenomenon can be explained. In quantum theory, photons are treated as energy quanta. The expression $|n\rangle$ indicates a state of an electromagnetic field containing $n$ photons. The intensity of the field is given by the expectation value of the photon number operator $\hat{n}$ which is equivalent to the mean number of photons in the mode.

$$\langle I\rangle \propto \langle \hat{n}\rangle = \langle \hat{a}^{+}\hat{a}\rangle, \tag{2.1.22}$$

where $\hat{a}^{+}$ is creation operator and $\hat{a}$ is the annihilation operator with

$$\hat{a}^{+}|n\rangle = \sqrt{n+1}|n+1\rangle,\ \hat{a}\big|n\rangle = \sqrt{n}\big|n-1\rangle \tag{2.1.23}$$

They obey the commutation rule for bosons:

$$[\hat{a}^{+}, \hat{a}] = 1.$$

Thus, the quantum mechanical version of the second-order correlation function becomes

$$g^{(2)}(\tau) = \frac{\langle \hat{a}^{+}(t)\hat{a}^{+}(t+\tau)\hat{a}(t)\hat{a}(t+\tau)\rangle}{\langle \hat{a}^{+}(t)\hat{a}(t)\rangle^{2}},$$

$$g^{(2)}(0) = \frac{\langle \hat{a}^{+}(t)\hat{a}^{+}(t)\hat{a}(t)\hat{a}(t)\rangle}{\langle \hat{a}^{+}(t)\hat{a}(t)\rangle^{2}}, \tag{2.1.24}$$

and

$$\langle \hat{a}^{+}(t)\hat{a}^{+}(t)\hat{a}(t)\hat{a}(t)\rangle = \langle n|\hat{a}^{+}(t)\hat{a}^{+}(t)\hat{a}(t)\hat{a}(t)|n\rangle. \tag{2.1.25}$$

For $n = 1$, with the definition in equation (2.1.23), one can get

$$\hat{a}(t)\hat{a}(t)|1\rangle = \hat{a}(t)|0\rangle, \tag{2.1.26}$$

where $|0\rangle$ corresponds to the vacuum state. Thus:

$$\hat{a}(t)|0\rangle = 0 \tag{2.1.27}$$

Therefore, one can obtain

$$g^{(2)}(0) = 0 \quad \text{for } |1\rangle \text{ and } |0\rangle. \tag{2.1.28}$$

For $n > 1$, equation (2.1.25) can be further simplified to

$$\langle \hat{a}^+(t)\hat{a}^+(t)\hat{a}(t)\hat{a}(t)\rangle = \langle n|\hat{a}^+(t)\hat{a}^+(t)\hat{a}(t)\hat{a}(t)|n\rangle$$
$$= n^2 - n. \quad (2.1.29)$$

Thus,

$$g^{(2)}(0) = \frac{n^2 - n}{n} = 1 - \frac{1}{n} < 1, \quad (2.1.30)$$

for $n > 1$, and

$$g^{(2)}(0) = 0 \quad (2.1.31)$$

for $n = 0$ or 1.

In this case, the probability of detecting a second photon immediately after the first one is smaller than the probability of detecting it at a later time. This effect is called photon anti-bunching. It cannot be explained classically. Figure 2.2 depicts $g^{(2)}(\tau)$ for the three kinds of photon sources. Table 2.1 summarizes their properties.

| **Light source** | **Property** | **Comment** |
|---|---|---|
| **All classical light** | $g^{(2)}(\tau) \geq 1$ | |
| | $g^{(2)}(0) \geq g^{(2)}(\tau)$ | Photon-bunching |
| **Coherent light** | $g^{(2)}(\tau)$=1 | Random arrival |
| **Single-photon source** | $g^{(2)}(\tau) < 1$ | Anti-bunching |
| | $g^{(2)}(0) = 1 - 1/n$ | $n$ is the number state |

**Table 2.1 Properties of different light sources.**

### 2.1.3. Single-photon emitters

In the previous chapters, the second-order correlation function of photon sources has been discussed. From the quantum mechanical point of view, a non-classical light source with the emission of single photons is theoretically possible. As discussed in Section 2.1.1, the photon number of the coherent state of a laser beam is given by a Poisson distribution with a certain average photon number, while the photons number of a thermal light source follows the Bose-Einstein distribution. Photons emitted by these classical light sources are confined within a spatial region defined by the wavepacket. However, it is hard to manipulate (read) distinct quantum information of a photon in a wavepacket. Whereas single photons emitted from the single-photon source, as quantum bits provide quantum polarization or phase state [29] that can be used for information storing and transmitting.

The application of single-photon sources is widely exploited for decades. The most promising field is the quantum information processing. Comparing with conventional electric information processes, the transmission speed of photons is much higher and the signal is resistant to environment interference resulting in a low loss. Obviously, information carried by only one photon also has much less risk of leakage. For a long-distance communication with quantum cryptography in the form of quantum key distribution (QKD) protocols, a single-photon source is especially useful for a quantum repeater [30]. Additionally, in quantum lithography, an $n$-fold improvement of the resolution of an interferometric experiment can be gained by integrating $n$ single-photon states [31]. Besides quantum information, single-photon sources have been widely used in other fields such as measurement of ultra-weak bio-chemiluminescence [32], highly sensitive detection of DNA [33], remote sensing of single atoms [34], ultra-accurate lidar experiment [35], diffuse optical tomography [36] and quantum beam-splitter by photon-entanglement [37]. In addition, the single-photon source with its unique properties promotes the development of quantum computers to perform tasks that can hardly be handled by classical computation methods.

Accordingly, the practical implementation of these potential applications of single-photon sources requests an ideal single-photon source possessing the following characters:

1. In the quantum information processing, an ideal single-photon source, as the name implies, should produce distinct photons at a defined time or within a finite time interval.

2. One should be able to trigger the single-photon emission in a controlled manner, which refers to an on-demand single-photon emission. The triggering can be, for instance, implemented by pulsed excitation.

3. For an unpolarized photon stream, filtering of photons with orthogonal polarization decreases the photon collection by a factor of 2. Thus, a single-photon source should preferably generate photons with defined polarization.

4. The quantum efficiency of a single-photon source should be high and ideally being as close to unity as possible.

5. For the purpose of being integrated with photonic components, a single-photon source should be robust during the integration experiment.

6. To fabricate a reliable quantum system, the single-photon source should exhibit high photostability under continuous excitation with high power.

7. The single-photon source should work properly at room temperature.

The requirements for an ideal single-photon source are rigorous, but alternative faulty single-photon sources exist and are widely used nowadays.

Highly attenuate laser pulses can produce distinct photons but it only corresponds to a weak coherent state instead of a single-photon state. From Section (2.1.1), it is known that a laser source obeys the Poisson-distribution $p(n)$. Equation (2.1.3) is repeated as:

$$p(n) = \frac{\bar{n}^n e^{-\bar{n}}}{n!},$$

where $\bar{n}$ is the average number of photons in a certain time period. With a heavily attenuated laser beam of $\bar{n} = 1$, the probability of finding one photon i.e. $p(1)$ is $0.368$. One can also derive that $p(0)$ has the same value. This means that generating a single-photon state is as likely as triggering no photons. Moreover, the probability of producing a two-photon state $p(2)$ is $0.184$. This multi-photon state generation cannot be neglected in the quantum information application. Especially for the quantum key distribution, the information carried by the additional photons can be eavesdropped [38].

An alternative approach is to use a nonlinear process, namely the parametric down-conversion, where a bulk nonlinear crystal is pumped by a laser beam. With a certain probability, one photon of the laser beam is converted into a photon pair with one signal photon and an idle photon. This process follows the energy and momentum conservation. The two photons have either the same or orthogonal polarization states. The idle photons can be used to predict the presence of the single photon signal.

Furthermore, some single quantum emitters also exhibit single-photon emission. Upon excitation, the single quantum emitter undergoes a radiative transition and thus a single photon is expected. High quantum efficiency can be obtained if the competing non-radiative transition is suppressed. For example, single quantum dots in III-V and II-VI

semiconductors have been found to be good candidates as single-photon emitters by many groups [39-41]. Moreover, single trapped atoms and ions have been observed to emit single photons [42-43]. Single molecules at room temperature such as dyes [44-46] and single-chain polymer molecules [47] also represent single photon sources implementation. Besides, color centers in diamond lattices with vacancy centers possess a radiation transition in an isolated three-level system, where the single-photon emission was observed [48]. The substituted defects showing single-photon emission include nitrogen-vacancy centers, silicon-vacancy centers [49] and germanium-vacancy centers [50]. In this work, the most interest is in the intensively studied and widely used nitrogen-vacancy centers for the single-photon emission at room temperature.

### 2.1.4. Hanbury-Brown and Twiss (HBT) setup

The concepts of electric field amplitude correlation and intensity correlation have been explained in Section 2.1.2. The amplitude correlation presented by the first-order correlation function can be observed by Young`s double slit experiment. However, for characterizing a single-photon source, the measurement of the second-order correlation function is not straightforward, even though photons can be sensitively detected by avalanche photodiodes (APDs). This is because any detector has finite dead times in the timescale of nanoseconds and after-pulsing effects upon the detecting avalanche [51]. Instead, employing of an additional APD can compensate the time window when one is recovering. Experimentally, the Hanbury-Brown and Twiss (HBT) setup consisting of two APDs is a standard solution to evaluate the second-order correlation function [52], which will be explained below.

**Avalanche photodiode (APD):**

An APD is a semiconductor light sensor with high sensitivity and response speed. With an external reverse voltage, the electron-hole pair generated by absorbing one photon is highly accelerated and thus bound electrons are released. This device is suitable for single photon detection because of the functionality of electron multiplication which efficiently enhances the electron flow of the photon detection events by a significant factor. In the Geiger mode of APD, the biased voltage is slightly above the breakdown threshold voltage, where the absorption at the single-photon level can trigger a strong charge avalanche for detection. An APD that can count the single-photon flux is also supposed to have dark count rates well below $1\,\mathrm{kHz}$ with several tens of percent quantum efficiency, sometimes even well above $50\%$. After one photon detection, a well-designed APD possesses a reasonable avalanche recovery time for the detection of the subsequent photons. This is normally realized by installing an electronic quenching circuit to reduce the voltage below the threshold after one detection event for a short time. If the avalanche recovery time is around $100\,\mathrm{ns}$, it puts a limitation on the maximum detected count rate to approximately $10\,\mathrm{MHz}$. A

higher capability can be reached in a trade-off for a lower sensitivity using a linear mode photodiode which is operated with relatively lower reverse voltage [53].

**HBT measurement:**

Although the APD can be used to register single photon events, due to the intrinsic dead time and afterpulsing effects of APDs, it is hard to measure the second-order correlation function of single photons directly. This task can be performed with the Hanbury-Brown and Twiss (HBT) setup using two detectors. The HBT setup was initially used by Robert Hanbury Brown and Richard Q. Twiss to measure the angular sizes of Sirius [43].

Figure 2.3 demonstrates the sketch of an HBT. The light beam is split by a 50/50 beam splitter and then directed into two separate photon detectors. A photon hitting one of the detectors triggers the working process while the other detector waits for a subsequent photon. In this case, the existence of the second detector eliminates problems caused by the dead time of the first detector and thus the second-order correlation function and the value of $g^2(0)$ can be measured but at the expense of preciseness. It is noteworthy that the practical $g^{(2)}(0)$ value in an HBT experiment can hardly reach the theoretical value due to the existence of background fluorescence and dark counts. The correction method for experimental $g^{(2)}(0)$ is introduced in Section 2.2.1.

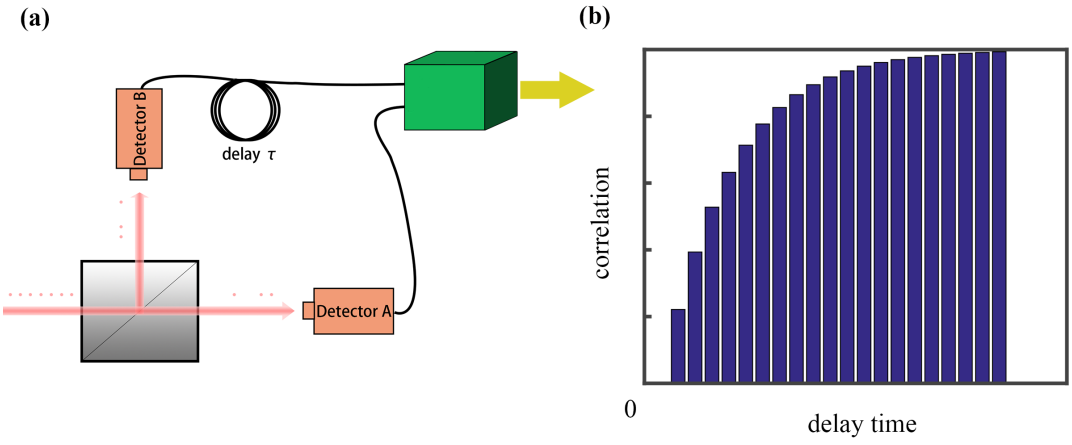


**Figure 2.3.: HBT measurement. (a)** shows the sketch of a Hanbury-Brown and Twiss setup. **(b)** shows the anti-bunching signals which is delayed for the compensating dead times.

In this section, starting from the basis of the photon and photon statistics, the second-order correlation function and the property of single photons has been introduced. Afterward, the HBT setup to experimentally measure the second-order correlation

function is demonstrated. In the following chapters, the concepts and the measurement method will frequently be used.

## 2.2. Nitrogen-vacancy centers in nanodiamonds

As mentioned in the section 2.1.3 there are several choices of single-photon emitters fulfilling the demands listed in section 2.1. Among them, the nitrogen-vacancy (NV) center in nanodiamonds (NDs) is a good candidate as a single-photon emitter and is nowadays widely investigated because of its unique optical properties [55]. The NV center as a single-photon source in NDs is introduced in this section.

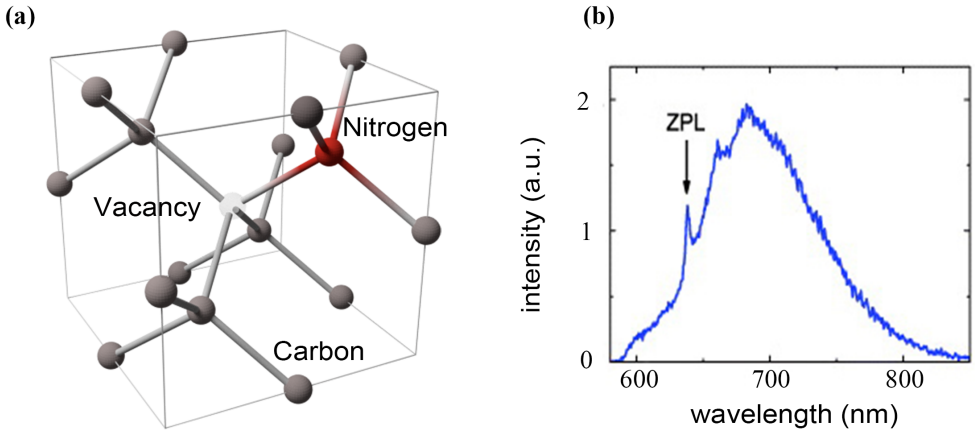


**Figure 2.4. NV center in diamonds (a)** demonstrates the lattice layout of NV centers in diamonds. **(b)** is the typical fluorescence spectrum of NV centers at room temperature adapted from [84].

Diamond, due to its 5.5 eV large band gap with a high Debye temperature [56], is a host for a variety of color defects exhibiting diverse optical properties. In the diamond lattice, the NV center is formed when a carbon atom in the diamond lattice is replaced by a substitutional single nitrogen atom (N) along with a vacancy (V) at an adjacent lattice point. The lattice layout of an NV center is drawn in Figure 2.4 (a). Depending on the charge state, there exist two types of NV centers: negatively charged $NV^-$ centers and neutrally charged $NV^0$ centers [57]. The negatively charged state $NV^-$ center is formed when receiving an additional electron from its adjacent nitrogen atom. This dissertation mainly focuses on the $NV^-$ center because it shows more useful properties (explained below) and thus without specified designation, NV denotes the negatively charged state $NV^-$.

Due to the combination of several remarkable properties, NV centers have drawn a wide attention since they were first reported in 1965 [58]. The NV centers have been experimentally shown to emit single photons [59-61]. At room temperature, the fluorescence emission covers wavelengths from red to near infrared with a stable and high brightness when excited by a 532 nm laser. Figure 2.4 (b) demonstrates the fluorescence spectrum of NV centers at room temperature. It has the zero-phonon line

of $637\ \mathrm{nm}$ and has broad width of around $200\ \mathrm{nm}$ due to the strong electron-phonon interactions at room temperature the vibrational. A remarkable feature of NV centers is that they show no photobleaching effect even upon continuous laser excitation with high energy at room temperature [62]. These fluorescence emission properties make the NV center a good photon source candidate for many applications. In bio-imaging applications, the fluorescence from NV centers has a spectrum far away from the fluorescence wavelength of most cell components and the emission has a good penetration through the surrounding tissue [63]. Besides, a single NV center can be treated as an isolated spin system with a long coherence time of $T \approx 2\ \mathrm{ms}$ [64]. The electron spin can be manipulated on-demand and initialized by optical pumping. Microwave fields and standard electron spin resonance techniques are used to coherently rotate the spin [64-66].

Another interesting field of NV centers is to achieve sub-wavelength resolution. Spatially separated NV centers experience different magnetic fields when put in a magnetic field gradient. In the Optically Detected Magnetic Resonance (ODMR) spectrum, individual NV centers show different Zeeman splittings of the spin sublevels corresponding to the local magnetic field value [67]. The optical approach allows a precisel study and manipulation of the spin of NV centers with a high nanoscale accuracy [68]. Associated with Stimulated Emission Depletion (STED) microscopy, the spin of the single NV center embedded in a solid immersion lens has been addressed with a resolution down to $2.4 \pm 0.3\ \mathrm{nm}$ [69].

In the field of the biology, sensing of single electrons and nuclear spins in biological molecules requires detection sensitivity of micro/nanotesla on a nanometer scale. Such a magnetic field of several nanoteslas corresponds to the one from a single proton at a distance of $10\ \mathrm{nm}$. NV center has been demonstrated for such nanoscale sensing of weak magnetic fields down to several nanoteslas making use of coherent manipulation of individual electronic spin qubits [70]. Besides, the combination of high photostability of NV centers together with the low toxicity and cytocompatibility of NDs make the fluorescent NDs good candidates as biomarkers. The injected NDs with NV centers were used to trace single particles in cells for a long time [71-73]. Moreover, living cells lying on the surface of the chip cause faint fluctuations of the magnetic field, which disturb the spins of the proximate NV centers that can be detected [74]. Thus, the behavior or bioprocess of living cells was measured using a sensor chip with an array of NV centers.

### 2.2.1. Three-level model of NV centers

In the previous section 2.1.2, the second-order correlation function has been explained. Figure 2.2 in the last section shows a $g^{(2)}(\tau)$ simulation of a standard single-photon source. The anti-bunching dip with $g^{(2)}(0) = 0$ clearly indicates the nature of a single-photon source. The curve can be fitted using an expression derived from a two-level system [75-76]:

$$g^{(2)}(\tau) = 1 - e^{-r|\tau|}, \tag{2.2.1}$$

where $\tau$ is the time delay between two signal channels and $r$ is the fluorescence transition count rate. From this model, the value of the second-order correlation function is between 0 and 1. However, the practical model of a NV center is more complicated than the two-level system. A conflict can be seen when the NV center is excited with higher power. An exemplary experimental second-order correlation measurement result is shown in Figure 2.5 (a) where a bunching phenomenon ($g^{(2)}(\tau) > 1$) emerges in the $g^{(2)}(\tau)$ function at around $\pm 30$ ns time delay. This bunching of photons implies that emission photons are impeded by a certain delay time after the coincident event, which can be theoretically explained by introducing an additional energy level with a longer lifetime.

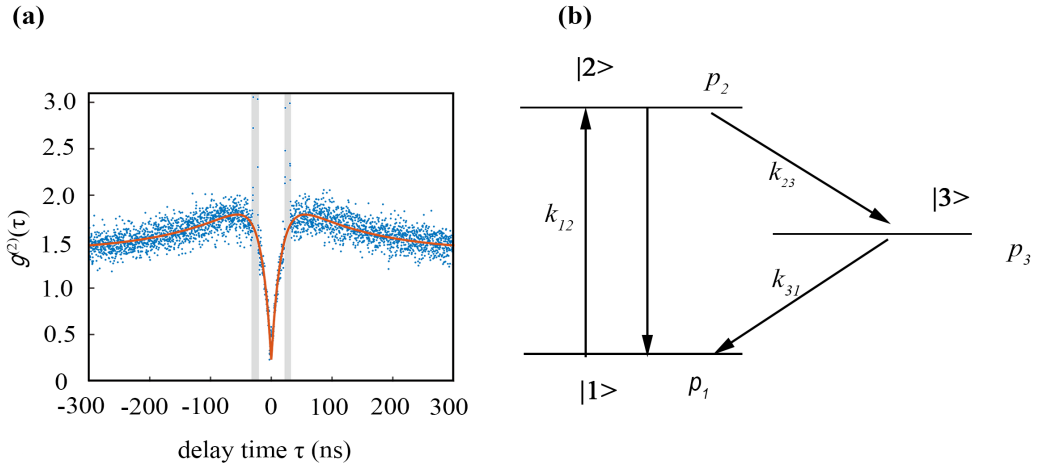


**Figure 2.5**: **Three-level modeling of an NV center**. **(a)** shows an exemplary experimental second-order correlation measurement data indicated by the blue dots; the red curve is a fit to the data using a three-level model. It includes bunching $g^{(2)}(\tau) \geq 1$ features at finite delays. **(b)** is the Jablonski diagram of a simple three-level system. $k_{i,j}$ is the transition rate from state $i$ to state $j$, $p_{i=1,2,3}$ are the simplified ground state, excited state and the metastable state, respectively.

Besides the ground state and the excited state in a two-level model, the electron

transitions in NV center involve an extra metastable energy level. Figure 2.5 (b) indicates the Jablonski diagram of a simple three-level system, where $k_{i,j}$ is the transition rate from state $i$ to state $j$, and the probability of states $|1\rangle$, $|2\rangle$, $|3\rangle$ is denoted by $p_i$, where $i,j = 1,2,3$. The transition dynamic can be described with the rate equations:

$$\frac{dp_1}{dt} = -k_{12}p_1 + k_{21}p_2 + k_{31}p_3,$$

$$\frac{dp_2}{dt} = k_{12}p_1 - k_{21}p_2 - k_{23}p_2, \tag{2.2.2}$$

$$\frac{dp_3}{dt} = k_{23}p_2 - k_{31}p_3,$$

Upon continuous-wave laser excitation, the system reaches an equilibrium condition which reads:

$$\frac{dp_1}{dt} = \frac{dp_2}{dt} = \frac{dp_3}{dt} = 0, \tag{2.2.3}$$

$$p_1 + p_2 + p_3 = 1.$$

With equations (2.2.2) and (2.2.3) one can deduce the equilibrium population of state $|2\rangle$:

$$p_2(\infty) = \frac{k_{12}}{\left(1 + \frac{k_{23}}{k_{31}}\right)k_{12} + k_{21} + k_{23}}, \tag{2.2.4}$$

It can be first assumed that the system is not in the saturated scheme, thus the radiation transition rate $k_{12}$ is proportional to the pump light intensity $P$ with an absorption cross-section $\sigma$:

$$k_{12} = \sigma P, \tag{2.2.5}$$

In the three-level model, photons emitted from the system stem only from the decay from level 2 to level 1 with the corresponding transition rate of $k_{21}$. One can express the emission rate $R$ according to equation (2.2.4) in the form of:

$$R = \frac{\beta P}{P + P_{sat}}, \tag{2.2.6}$$

Where

$$\beta = \frac{k_{21}k_{31}}{k_{23} + k_{31}},$$

$$P_{sat} = \frac{k_{31}(k_{21} + k_{23})}{\sigma(k_{31+}k_{23)}}.$$

The coefficient $\beta$ represents the difference between the two-level system and the three-level system. If $k_{23}$ is zero then $\beta = k_{21}$, which fits the two-level modeling. In the case that the life time of state $|3\rangle$ is long enough as $k_{31} \ll k_{23}$, $R$ drastically decreases, resulting in a reduction of the quantum efficiency of the source.

From the equation (2.2.6) one can predict three different working regimes. First, if the system is excited with an intensity $P \ll P_{sat}$, the emission rate increases linearly with the excitation intensity. Secondly, if the excitation intensity reaches $P \geq P_{sat}$, the emission is in the saturated region. Finally, when the excitation intensity is further increased to $P \gg P_{sat}$, the emission rate depends much less on the excitation intensity anymore and approaches a constant.

Moreover, the second-order correlation function $g^{(2)}(\tau)$ can be defined by the population of the state $|2\rangle$ at time $\tau$, $p_2(\tau)$, normalized to the steady-state rate at infinite time [77] :

$$g^{(2)}(\tau) = \frac{p_2(\tau)}{p_2(\infty)}. \tag{2.2.7}$$

In this calculation, the initial state is assumed to be with $p_1 = 1$, $p_2 = p_3 = 0$. The correlation function is derived from equation (2.2.2), (2.2.3) and (2.2.4) to:

$$g^{(2)}(\tau) = 1 - \beta e^{-\gamma_1 \tau} + (\beta - 1)\beta e^{-\gamma_2 \tau}, \tag{2.2.8}$$

where:

$$\gamma_1 = k_{12} + k_{21},$$

$$\gamma_2 = k_{31} + \frac{k_{12}k_{23}}{k_{12} + k_{21}},$$

$$\beta = 1 + \frac{k_{12}k_{23}}{k_{31}(k_{12} + k_{21})}.$$

This biexponential expression of $g^{(2)}(\tau)$ derived from the three-level model fits the

experimental data quite well and the bunching behavior of NV center emission is explained by the accumulation population of the state $|2\rangle$. In the following chapters, the experimental $g^{(2)}(\tau)$ measurement data are fitted to this model.

**Background correction for second-order correlation experiment:**

Experimentally, the second-order correlation measurement of a single-photon source at zero-time-delay $g^{(2)}(0)$ cannot reach the theoretical value of zero due to the presence of background. The background is mainly composed of stray light in the lab, internal noise of the APDs and the fluorescence from excited surrounding molecules. The output count rate of the APD without any light incident is called the dark count rate mainly corresponding to the internal thermal effects generated carriers in the APDs. Together with the stray light in the lab, the experimental conditions in this work has a practical count rate below $200$ counts/s on each APD with all lasers and lights off. The average diameter of the NDs used here (as shown in Figure 2.8) is below $50$ nm. When the ND is embedded in the photoresist, the molecules around the ND are also excited by the laser focus. The emission from the surrounding photoresist increases linearly with the excitation laser intensity. And experimentally, the second-order correlation measurement of the background noise gives $g^{(2)}(0) = 1$, revealing an expected uncorrelated nature of the background fluorescence. Whereas the fluorescence intensity from the NV centers follows the three-level modeling and it reaches a saturation value at a high excitation laser intensity. Therefore, the light source inspected by the second-order correlation measurement is a mixed photon source. The background influence on the $g^{(2)}(\tau)$ correlation function can be evaluated with the approach as described below.

To understand the correction procedure, it is necessary to specify the practical measurement scheme of the second-order correlation in this experiment. As described in Section 2.1.4, the second-order correlation is evaluated by measuring the chance of coincident events on two independent detectors. Here, coincidence means that two events are sensed by two detectors within a time window $t$. In other words, any two photon events detected by the system within a time delay less than $\tau$ are considered as coincident events. Given that there are $N_1$ events per unit time detected by detector 1, the total coincident time window for all events is $N_1 t$. If the count rate of detector 2 is $N_2$, within this time window, the detector 2 gives the coincident count rate of $N_1 N_2 t$. This is also the number of coincident events per unit time [60].

In the practical second-order correlation measurement with two APDs, the data obtained directly is the raw coincident events $c(\tau)$ at the time delay $\tau$. This quantity can be normalized by the expected coincident events as described above to get the rate of the coincident events:

$$C(\tau) = \frac{c(\tau)}{N_1 N_2 \omega T}, \tag{2.2.9}$$

where $\omega$ is the time bin of the $g^{(2)}(\tau)$ measurement and $T$ is the integration time.

With the impact of the uncorrelated background, the second-order correlation measurement is expressed using the normalized coincident rate:

$$g^{(2)}(\tau) = [C(\tau) - (1 - \rho^2)]/\rho^2, \tag{2.2.10}$$

with $\rho = S/(S + B)$, where $S$ is the photon count rate from the NV center and $B$ is the count rate of the background light. With this correction equation, the corrected $g^{(2)}(0)$ in the experiment of Figure 4.5, approaches 0, pointing out the character of single-photon emission.

## 2.2.2. Electronic structure and optical properties of NV centers.

In the previous sections, the advantages of NV centers as single-photon sources have been briefly reviewed. These properties originate from the intrinsic properties and unique electronic structure of NV centers which are explained in this section in detail.

The lattice of the NV center is shown in Figure 2.4 (a). There are three unpaired electrons from the three carbons nearest to the vacancy and one pair of electrons from the nitrogen (nitrogen has five electrons and three of them form covalent bonds with the three carbons nearest to the nitrogen). The NV center associated with such five electrons forms the neutrally charge $NV^0$ center. And the negatively charge $NV^-$ center involves an additional sixth electron. The electronic configuration of $NV^-$ center exhibits six different possible optical transitions. However, it is more convenient to treat the NV center as a configuration with two holes instead of six electrons.

Figure 2.6 shows the electronic structure of the NV center at room temperature [79]. The NV center has a stable spin-triplet ground state with a zero-field splitting of $D = 2.87$ GHz caused by the spin-spin interactions between the singlet ($m_s = 0$) and the triplet states ($m_s = \pm 1$). The quantization axis is along the N-V axis. In the presence of an external magnetic field $B_{\parallel}$, the triplet states degeneracy is lifted by the Zeeman shift of $\Delta = m_s \gamma B_{\parallel}$, where $\gamma$ is the gyromagnetic ratio with a value of $2.87$ MHz/G. The excited state is also a spin-triplet state with a zero-field splitting of $1.42$ GHz [80-81]. The ground state and the excited state are coupled either through a radiative decay channel with a zero-phonon line of $637$ nm and $200$ nm thermal broadening ($600$ nm $-$ $800$ nm) around it, or through a non-radiative decay channel. The non-radiative decay involves an additional metastable spin-singlet state. This metastable state has a longer life time than the excited state of around $300$ ns. The radiation transition from the excited state to the ground state primarily occurs with spin conservation. Nevertheless, there exists a unique intersystem crossing transition that is not spin-conserving: Here, the $m_s = \pm 1$ excited states are de-populated to the metastable singlet state $m_s = 0$ and subsequently down to the $m_s = 0$ ground state as a non-radiative decay. Therefore, the $m_s = \pm 1$ states exhibit the relatively low

fluorescence intensity. This transition mixes up the initial spin polarization state of the NV center. After being sufficiently pumped, the metastable state has a larger probability to be occupied due to the longer life time and the spin non-conservation transition.

Given that the $m_s = 0$ state is degenerated with the $m_s = \pm 1$ in the ground state, the probability of non-radiative decay from $m_s = \pm 1$ excited states to the metastable singlet state increases. Consequently, the spin-conserved radiation transition is suppressed, leading to an observable decrease of the fluorescence intensity. The NV center can be polarized to the singlet state with the presence of a continuous laser excitation. This key characteristic allows the electronic spin state to be initialized through optical pumping and to be detected via spin-state-dependent fluorescence. In combination with conventional electron spin resonance (ESR) techniques for coherently manipulating the spin, the NV center is highlighted as a platform for applying magnetometry in various areas, including biology, geology and novel materials [80].

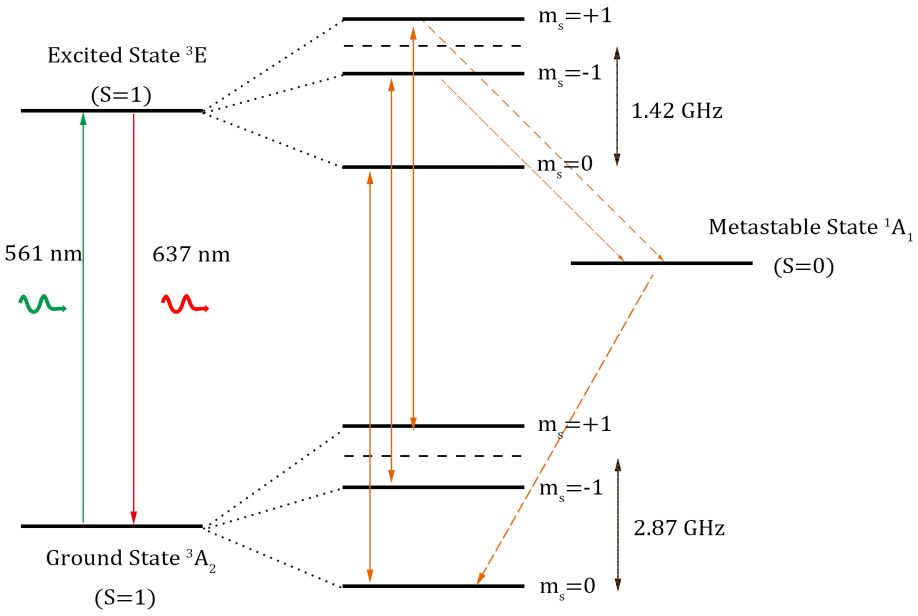


**Figure 2.6**: **Electronic structure of an NV center at room temperature.** The triplet ground state manifold and the triplet excited state manifold are separated by $\Delta E = 1.95$ eV, corresponding to a zero-phonon line of 637 nm. Each of the three electronic spin projections ($m_s = \pm 1, 0$) in the ground state manifold is coupled to the corresponding spin projections in the excited state manifold upon excitation. With a certain probability, spin-orbit interactions allow the $m_s = \pm 1$ excited states couple to the metastable singlet state, which is then coupled to the $m_s = 0$ ground state via a non-radiative transition. This figure is drawn according to reference [79].

## 2.2.3. Nanodiamonds

NV centers exist in both, bulk diamonds and nanodiamonds. Diamond crystals with diameters below 1 µm (usually around 100 nm) are called nanodiamonds (NDs).

NDs are widely used in industrial applications, e.g. for grinding and polishing to obtain smooth surfaces by exploiting of the sheer hardness of NDs. The smallest NDs found were only 1.6 nm in diameter, which corresponds to only 400 carbon atoms surrounding an NV center [72]. The color centers such as the NV centers are found in NDs even exhibiting single-photon emission. Compared with bulk diamonds, NDs are much easier to incorporate into photonic systems, especially for hybrid quantum optical systems [82]. In contrast to fabricating photonic structures directly with bulk diamonds, one can access the color center by either embedding NDs in other lithography materials (this work) or directly picking pre-characterized NDs by an atomic force microscope (AFM) tip [83]. The use of NDs enormously extends the choice of materials for photonic structures. However, there are also some problems emerging from the size of NDs. The NV center is generally very close to the surface of the surrounding nanocrystal, and thus the quantum efficiency can be influenced by the surface strain, impurities and diffraction, which inflicts more than bulk diamonds. It has been demonstrated that the emission efficiency of NV centers in NDs varies from 10% to 90%. [84].

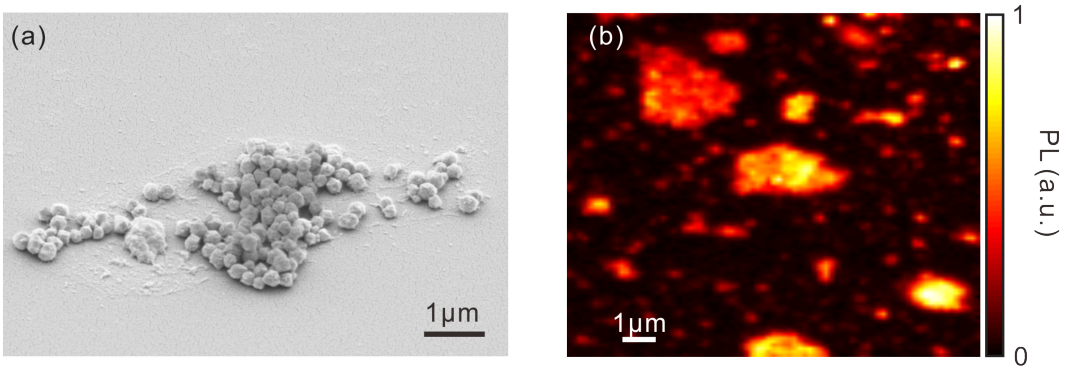


**Figure 2.8: Aggregated NDs on a silica glass substrate.** The NDs are, without any prior treatment, spin-coated on the substrate. **(a)** shows an electron micrograph of aggregated NDs and **(b)** shows a laser scanning confocal fluorescence microscopy image of an aggregated area.

Isolated NDs with color centers occur naturally in meteorites but can also be synthetically produced. There are two main approaches: high-pressure high-temperature (HPHT) synthetization [85] and detonation [86], both requires a chemical purification process. Other methods such as laser ablation in liquid [87] and bead assisted sonic disintegration of a polycrystalline chemical vapor deposition film [88]

have been demonstrated to produce NDs with the smaller size. It is notable that individual ND particles aggregate with each other forming ND groups. Figure 2.8 shows an electron microscope image (a) and a laser scanning confocal microscope image (b) of aggregated NDs on a glass substrate. This effect is an obstacle for the application of NDs but can be removed by surface modification [89].

In this section, NV centers in NDs are introduced as single-photon sources. Exploring the optical and electronic nature of NV centers boosts the exploiting of them including the experiments in the following chapter.

## 2.3. Laser scanning confocal fluorescence microscopy

The previous section has introduced NV centers in NDs as single-photon emitters. To harvest fluorescence light of NV centers, advanced practical experimental methods are required. The first step is to find out and characterize NV centers for the following fabrication of quantum-photonic structures.

Confocal fluorescence microscopy is a common method for mapping photon emitters, which is the basis for further characterizing them. Generally, in comparison with the conventional wide-field optical microscope, the confocal fluorescence microscopy provides true three-dimensional optical resolution by suppressing the signal from out-of-focus planes.

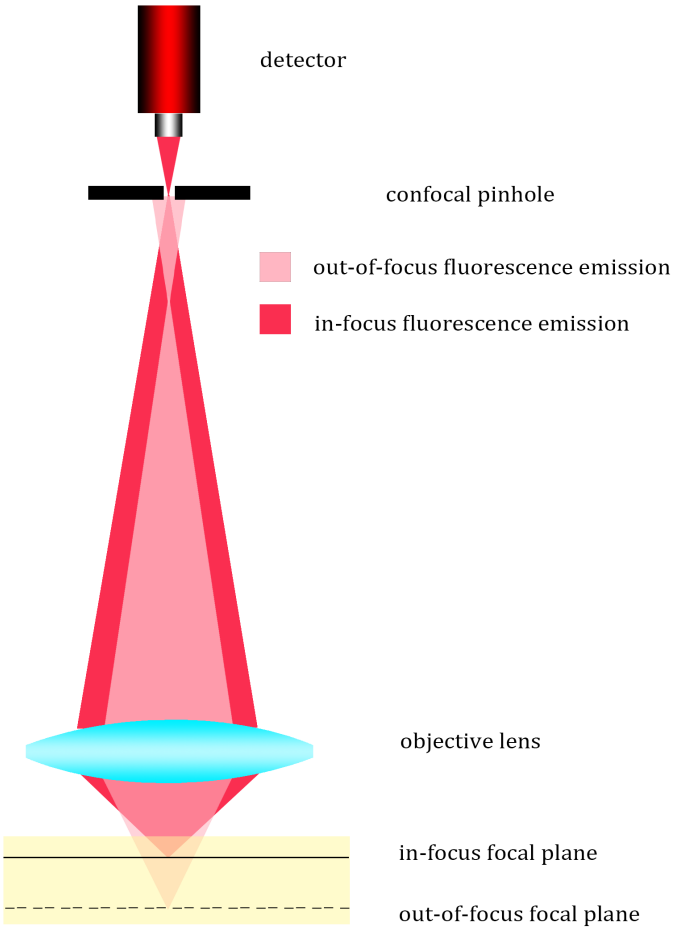


**Figure 2.9: Sketch of a basic confocal fluorescence microscope setup.** Emission light originating from out-of-focus focal planes is blocked by the pinhole in front of the detector. The spatial confinement depends on the pinhole diameter.

When examining samples under a conventional wide-field optical microscope, the optical sectioning capability is governed by the objective lens' numerical aperture (NA). In fluorescence microscopy, optical sectioning is improved, since only fluorophores which have been excited and emit will add to the fluorescence signal. However, in the case that the fluorophores are embedded in a three-dimensional fluorescent environment, surrounding molecules fluorescence contribute interfere the observation of the object, and the precisely locating of the fluorophores in three-dimension is hard. This limitation is especially notable if the sample volume is thicker than 2 µm. In this case, an acceptable resolution for the emitter localization is largely hindered. One solution is to optically segment the specimen by an aperture with a micrometer-sized pinhole at the conjugated image plane in the detection path as shown in Figure 2.9. The confinement works not only in the lateral plane but also along the vertical direction which defines the finite focus plane. With a good alignment, the excitation laser focuses on the sample and the light originating from the confocal volume is imaged by the objective lens and focused through the pinhole without restraint, but the simultaneously imaged light from plane out-of-focus is repelled by the pinhole. Thereby, the true three-dimensional optical resolution is achieved.

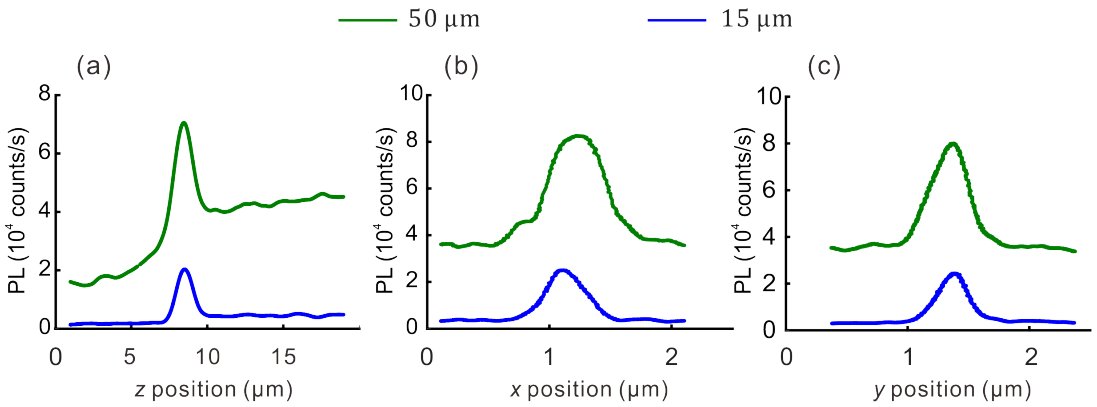


**Figure 2.10**: **Comparison of line scan photoluminescence (PL) signal detected with different confocal pinhole size.** Fluorescence signal while line scanning over a single NV center along the vertical optical $z$ axis **(a)**, planar directions $x$ **(b)**, and $y$ **(c)** with a pinhole diameter of 50 µm (green curves) and 15 µm (blue curves). In the line scanning along $z$ direction, the confocal volume traveled from the air through the interface between air and glass and then focused into the glass. With the larger pinhole, a gradually increasing of fluorescence intensity shows when approaching the interface and with a smaller size pinhole, the volume confinement improves.

Another difference is that in the conventional wide-field optical microscope, the sample is illuminated by a broadband light source and the image is formed either directly by

eyes or by a photon-sensitive device. In the laser scanning confocal microscope, the sample is optically segmented by pumping each optical point using a laser. Each pixel of the object can be pumped during the motion of the stage or the rotation of the reflection mirror in a raster fashion. The image is achieved by reforming the collected emission signals from all segments in all three dimensions.

Figure 2.10 illustrates the photoluminescence (PL) of an NV center detected under the line scan of the confocal fluorescence microscopy with different pinhole sizes. The NDs aqueous suspension is spin-coated on a pre-cleaned glass substrate. The NV center is pumped by a $561\ \mathrm{nm}$ cw laser focused through an oil-immersed objective lens with $\mathrm{NA} = 1.4$ and $100\times$ magnification. Fluorescence photons are filtered by a $650\ \mathrm{nm}$ long-pass spectra filter before being detected by a fiber-coupled APD. The sample is fixed on a piezoelectric stage to perform the line scans along all three directions. With a pinhole of $15\ \mu\mathrm{m}$ diameter, a large amount of the background light is blocked (details about the experiment setup can be found in Section 4.1). The peak of the fluorescence intensity corresponds to the confocal volume containing the NV center. After the line scans in all three directions, the pinhole is removed but the fiber coupler with a diameter of $50\ \mu\mathrm{m}$ still acts as a larger pinhole. One can clearly see the increase in the background light intensity. With a smaller pinhole of $15\ \mu\mathrm{m}$ diameter, the background intensity is reduced by an averaged factor of 10 and the signal-to-noise ratio is improved by an averaged factor of 5. Such improvement is crucial in the field of quantum optics. With the application of the single photons, as described in section 2.2.1, the reduction of background signals significantly improves the experiment by purifying the single-photon emission.

As a conclusion, the laser scanning confocal fluorescence microscopy, compared to conventional optical microscopy, offers enhanced spatial resolution, better contrast, and is suitable for detection of the fluorescence from the single nanoparticle emitter.

## 2.4. Direct laser writing (DLW)

The previous section has introduced NV centers in NDs as single-photon emitter. However, the application of NV centers in quantum optics is restricted by the lack of a reliable method to precisely fabricate and align the on-chip optical components such as lenses, filters, and beam-splitters with respect to the NV centers on the nanoscale. To realize this, NV centers have to be pre-characterized and connected by aligned quantum components. In a two-step process, such alignment is not straight-forward because normally the fabrication process of optical components changes experiment coordinate. Moreover, there are only a few methods that can be relied on to structure true 3D nano-architectures. One of them is the direct laser writing (DLW) technique. In this chapter, the DLW technique for fabricating nearly arbitrary-shaped three-dimensional quantum components is presented.

In 1997, DLW process using multi-photon absorption was demonstrated by Micheal T.Gale and Stefano Pelli [90-91] several years after the previous work on single-photon absorption. The capability of creating arbitrary 3D nano-structures earned applications in various fields such as nano-optics [92], microfluidics [93] and metamaterials [94]. The DLW is a microscale 3D printing technology using multi-photon absorption. It offers an opportunity for fabrication of readily assembled 3D structures with almost nearly arbitrary shapes. The printing process follows the trajectory of the relative motion of a tightly focused ultrafast laser in a photoresist volume. For a negative-tone photoresist, it locally polymerizes the photoresist impinged by the laser beam via multi-photon absorption. The unpolymerized parts are washed out in the following development step. Unlike other lithography techniques, such as the electron-beam lithography, DLW enables tailored 3D structures without a multi-step fabrication and recoating.

### 2.4.1. Two-photon absorption

The 3D fabrication is achieved using two-photon absorption (2PA). Unlike one-photon absorption (1PA) which is mostly seen in our daily life, molecules simultaneously absorb photon-pairs instead of single photons and thus the probability of 2PA depends on the square of the local light intensity. In other words, the strength of the interaction decreases quadratically rather than linearly when the local electric field intensity decreases, which is a non-linear process.

The absorption of two photons in 2PA happens in one step or at the same time rather than by a sequence of processes. For 1PA, the material interacts with photons and the energy of one photon is enough to offer the electric transition of the molecule or atom from the initial state to an excited state. The probability of 1PA process is proportional to the density of the absorber as well as the local photon density. The 1PA of a plane

wave exhibits the intensity changes as:

$$\frac{\mathrm{d}I}{\mathrm{d}z} = -\sigma_{1PA} \cdot N(z) \cdot I(z) \tag{2.4.1}$$

where $I$ is the light intensity and $\sigma_{OPA}$ is the absorption cross-section which is related to electric transition dipole moment of the molecule. $N(z)$ is the absorber molecule density at the initial state and $z$ is the penetration length of the light into the material. If a laser beam is focused into the volume of a highly absorbing material, the light intensity will experience highly attenuation. In the case of a low absorber density, where the laser energy variation along the propagation of the light can be neglected and the number of the excited absorbers stays constant along the propagation axis, the 1PA process occurs along the whole propagation axis. In other words, there is no confinement, thus no controlling, of the absorption along the propagation direction.

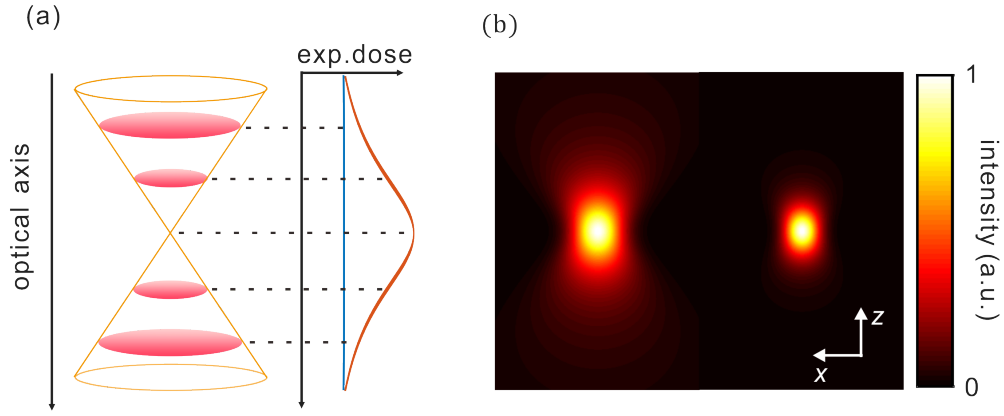


**Figure 2.9**: **(a)** At each planar along the optical axis, the exposure dose of the photoresist corresponds to the integration of the intensity (blue curve) of the 1PA and the intensity square (red curve) of the 2PA. The exposure dose of 1PA is constant along the optical axis; whereas the exposure dose of 2PA has its maximum at the focal point. **(b)** illustrates the simulated exposure intensity for 1PA (left) and 2PA (right). The calculation was made for a Gaussian beam that impinges into a low absorption material.

In contrast to 1PA, the probability of 2PA process depends on the probability to find a photon-pair locally which is proportional of the square of the intensity. Thus, similar to the light attenuation for 1PA, the one for 2PA is:

$$\frac{\mathrm{d}I}{\mathrm{d}z} = -\sigma_{2PA} \cdot N(z) \cdot I^2(z) \tag{2.4.2}$$

where $\sigma_{TPA}$ is the cross-section of the absorber molecule for 2PA. Typical values for most molecules are quite small compared with the ones for 1PA. In many cases, the

cross-section of 2PA is on the order of $10^{-50}$cm$^4$ sec molecules$^{-1}$ photon$^{-1}$. As a result, the promotion of 2PA requires high local photon density, and in an optimized manner only the focal point of the laser beam can fulfill the requirement. Therefore, the confinement along the propagation axis is achieved. Experimentally, this requirement can be fulfilled by employing commercially available femtosecond laser with the wavelength in the near infrared region. Such laser can generate pulses with peak power on the order of a kilowatt and the average power on the order of a milliwatt with 80 MHz repetition rate. Focused by a high NA objective lens, the photon flux is enough to establish a 2PA process.

In an absorbable material, the exposure dose corresponding to the possibility of 2PA or 1PA in each plane along the optical axis of the focused laser beam is calculated as shown in Figure 2.9. Unlike the 1PA process described above, the integration of squared optical intensity in each individual transverse section along the optical axis has the maximum value at the focus and decreases rapidly away from the focus. Thus, within the diffraction limit, the 2PA process is also confined along the optical axis resulting in a spatially 3D selective excitation of molecules. Such non-linear confinement of the excitation by the 2PA is used to realize not only the 3D nanofabrication but also the fluorescence microscope [95-96], optical data storage [97] and photodynamic therapy [98]. Multi-photon or more precisely two-photon microscopy can also be used as point scanning technique that uses a pulsed infrared laser with a tunable wavelength. At the wavelength approximately twice the excitation maximum of a fluorophore, two photons that simultaneously interact with the fluorophore can be excited. These events are restricted to the exact focal point of the laser, so an extremely small volume is excited and no confocal pinhole is required. Furthermore, as the infrared light penetrates deep into tissue multi-photon confocal microscopy is an excellent choice for intravital imaging.

## 2.4.2. Photoresists

A photoresist is a material sensitive to photons. In optical lithography, photoresist molecules absorb photons to form patterns. Generally, there are two types of photoresists. The positive-tone photoresists get soluble by the developer after the exposure with photons, whereas for negative-tone photoresists, exposed parts become solid and the unexposed parts are washed out in the development process. In this work, only negative-tone photoresists are used.

In the 2PA process, photons induce a chain growth mechanism in the photoresist to form materials with high molecular weight [99]. There are two molecule components involving in this process: the photoinitiator and the monomer. The photoinitiator molecules account for an only very small proportion of the photoresist. Most of the resists consist of a monomer with small molecule weight. They do not directly react with each other but can form polymer chains by radical polymerization with the aid of

free radicals generated from the photon absorption process. The photoinitiator molecules absorb photons by 2PA and convert the energy of photons into chemical energy by generating free radicals, which starts the polymerization process. The choice of the photoinitiator determines the excitation laser wavelength and the efficiency of the free radicals generation. In the case of monomers with more than one polymerizable group, molecule networks are formed. The details of the polymerization process are quite complex and a research area itself [100] will not be further investigated in this work.

### 2.4.3. Process of three-dimensional structuring

The theory of DLW is explained in the preceding sections. This part demonstrates the typical workflow of DLW in this work to give an impression of DLW practically.

The principle of 2PA demands a writing laser with a high intensity. Here, a femtosecond laser at a wavelength of 780 nm is used. The laser is modulated by an acoustic-optic modulator (AOM) driven by a home-built RF driver controlled by a computer.

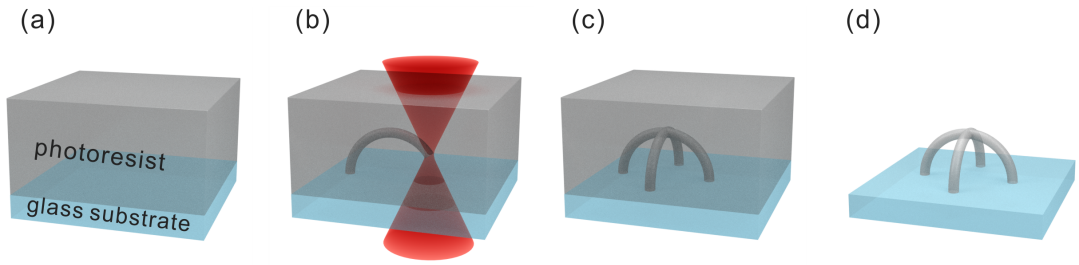


**Figure 2.10: The process of direct laser writing**. **(a)**, A glass substrate is covered with photoresist. In this work, the negative-tone photoresist is used for all experiments. **(b),** A highly focused femtosecond laser polymerizes the photoresist along the trajectory of the focal volume via 2PA. **(c)**, The photoresist turns to be solid and insoluble to the developer in the development process. **(d)**, The 3D micro-structure emerges after the residual photoresist being flushed out.

Figure 2.10 demonstrates the workflow of DLW in principle. The photoresist is either spin-coated or drop-casted on the glass substrate. In a normal DLW mode, the sample is fixed on the piezoelectric stage with the bare glass side facing down to an oil-immersed objective lens with the NA of 1.4. With the laser on, the photoresist is polymerized following the relative trajectory of the laser focus within the resist. 2PA confines the polymerization process within only the tightly focused volume, which constructs the 3D polymer structure with a different refractive index. After the writing process, the sample is taken out of the setup and bathed in the solvent (the solvent depends on the type of photoresist) to wash out the unexposed photoresist. After dried by the nitrogen gas, 3D micro-structures emerge on the substrate.

In this chapter, a powerful tool for fabrication of arbitrary 3D microstructures is presented. The 2PA enables the 3D structuring by restricting the perception of the photoresist to the laser within a tightly confined volume especially along the laser axis. The theory behind the photoresist formation and polymerization is briefly introduced. Finally, a typical workflow of the DLW is demonstrated. Details about the experimental process and the workflow in our case will be described in Chapter 4.

# 3. Integrated setup for wiring up pre-characterized single NV centers in nanodiamonds

For years, people have been exploring for ways to manipulate and apply single-photon emitters on the nanoscale. It is especially interesting to on-demand integrate single-photon sources onto quantum-photonic chips together with well-aligned micro-size waveguides, beam splitters and other optical components. Previous experiments applied atomic force microscope (AFM) tip to pick up and transfer a pre-characterized diamond nanocrystal containing a single NV center to the desired location near the quantum-photonic component [83]. However, the diameter of the diamond nanocrystal with a single NV center is normally of tens of nanometer [101], which diminishes the efficiency of picking and especially transferring the nanocrystal. Additionally, using this method, NDs can only be transferred to the surface of the photonic components or their vicinity, which restricts the coupling efficiency of the emission photons. Other method pre-characterizes and locates the single-photon emitters directly on the chip with a written marker. Subsequently, optical components are structured using electron beam lithography and thereby the NV center is integrated with another setup. In this two-step method, structures with high resolution can be achieved but it is restricted by the possibility of misalignment and the lack of the writing capability in 3D [102].

In the previous chapter, the DLW technique realizing arbitrary 3D structuring is introduced. Here, the DLW is integrated with the setup for NV center characterization. In the setup, firstly, NV centers are individually localized and characterized using the laser scanning confocal fluorescence microscopy. This characterization includes the brightness, second-order correlation function, and the dipole orientation. Secondly, pre-designed quantum photonic components are fabricated directly at relative positions around the pre-localized NV centers. These two parts will be presented in the following.

## 3.1. Experimental setup

As introduced above, this setup can be simply divided into two functionalities: one part for the NV center characterization using laser scanning confocal fluorescence microscopy and the other part for structure construction using DLW. Both functionalities are required to be operated in the micro- or nano-scale. The combination means they share the same working coordinate and it demands ultra-high spatial alignment accuracy on the sample. Besides, the two functionalities should work independently.

As present in the previous chapter, NV centers in NDs exhibit high fluorescence intensity under laser excitation. The absorption spectrum of an NV center has a peak at $571\,\mathrm{nm}$ with a broadening of about $200\,\mathrm{nm}$. In this work, a $561\,\mathrm{nm}$ cw semiconductor laser (OBIS 561 LS from Coherent GmbH) is used for excitation. Compared to the commonly used frequency-doubled $532\,\mathrm{nm}$ Nd:YAG laser [111], $561\,\mathrm{nm}$ is closer to the peak of the absorption spectrum of NV center. The DLW, as introduced in the previous chapter, demands an ultrafast laser source with high intensity. Here a frequency-doubled femtosecond fiber laser is used at the wavelength of $780\,\mathrm{nm}$ (T-Light from MenloSystems). The $780\,\mathrm{nm}$ writing laser is modulated by an acousto-optic modulator (MTS40-A3-750.850 from AA OPTO-ELECTRONIC) driven by a home-build RF-drivers. Accordingly, the foci of two lasers on the sample must hit the same location laterally and axially. It is demonstrated in the next section how the focus alignment is performed using the gold spherical beads as a regulator.

The layout of the setup is depicted in Figure 3.1. Here, a commercial microscope (Leica DM IRB) is used as a basic platform. The back-illumination port of which is used as an entrance port of the writing and excitation laser. On the sample, the axial and lateral resolutions are enhanced for both functionalities by applying an objective lens with the magnification of $100\times$ and NA of 1.4 with oil immersion (Leica HCX PL APO 100×/1.40-0.70 Oil CS). Such preseting improves the resolution of the fluorescence detection to an Abbe diffraction limit with corresponding collection solid angle of $1.67\pi$ [112]. In order to perform the raster scan over the sample and to locate individual centers, the sample is mounted on a high-resolution piezoelectric positioning stage with the motion range of $200\,\mu\mathrm{m} \times 200\,\mu\mathrm{m}$ laterally and $20\,\mu\mathrm{m}$ vertically (P-517 from Physik Instrumente). For a larger movement range, the piezoelectric stage is fixed on a motorized stage with a planar travel range of $120 \times 100\,\mathrm{mm}$ (SCAN IM 120×100 from Märzhäuser Wetzlar GmbH & Co. KG). The scanning route of both stages is programmable via the computer. The fluorescence light is collected by the same objective lens and the most of it travels back via the same path but through the DM1. 10% of the light collected by the objective lens is directed to an integrated microscope integrated CCD camera for visualization of the written structures on the sample and a silicon photodiode for interface finding and beam aligning. At the dichroic mirror (DM2), the fluorescence photons are exclusively reflected to the detection path (orange path in Figure 3.1).

The fluorescence light, after being reflected twice by two mirrors, goes through a set of 4f imaging system consisting of two identical lenses with $50\,\mathrm{mm}$ focal length and one $15\,\mu\mathrm{m}$ confocal pinhole at the foci. The objective lens is originally designed for a tube lens with $200\,\mathrm{mm}$ focal length to achieve the $100\times$ magnification. In this work, a lens with $50\,\mathrm{mm}$ focal length is used as the tube lens. Hence the total magnification in the image plane, where the pinhole is located, is reduced to $25\times$. The excitation laser focuses on the sample and the diameter of the airy disk is estimated as $1.22\times\mathrm{wavelength/NA} = 1.22\times(700\,\mathrm{nm})/1.4 = 605\,\mathrm{nm}$. Hence, the imaginary spot

on the pinhole is magnified 25 times to $605\ \text{nm} \times 25 = 15.125\ \mu\text{m}$. This pinhole size, therefore, is referred to as 1 airy unit [112]. This is a good compromise with good background suppression and better photon detection efficiency.

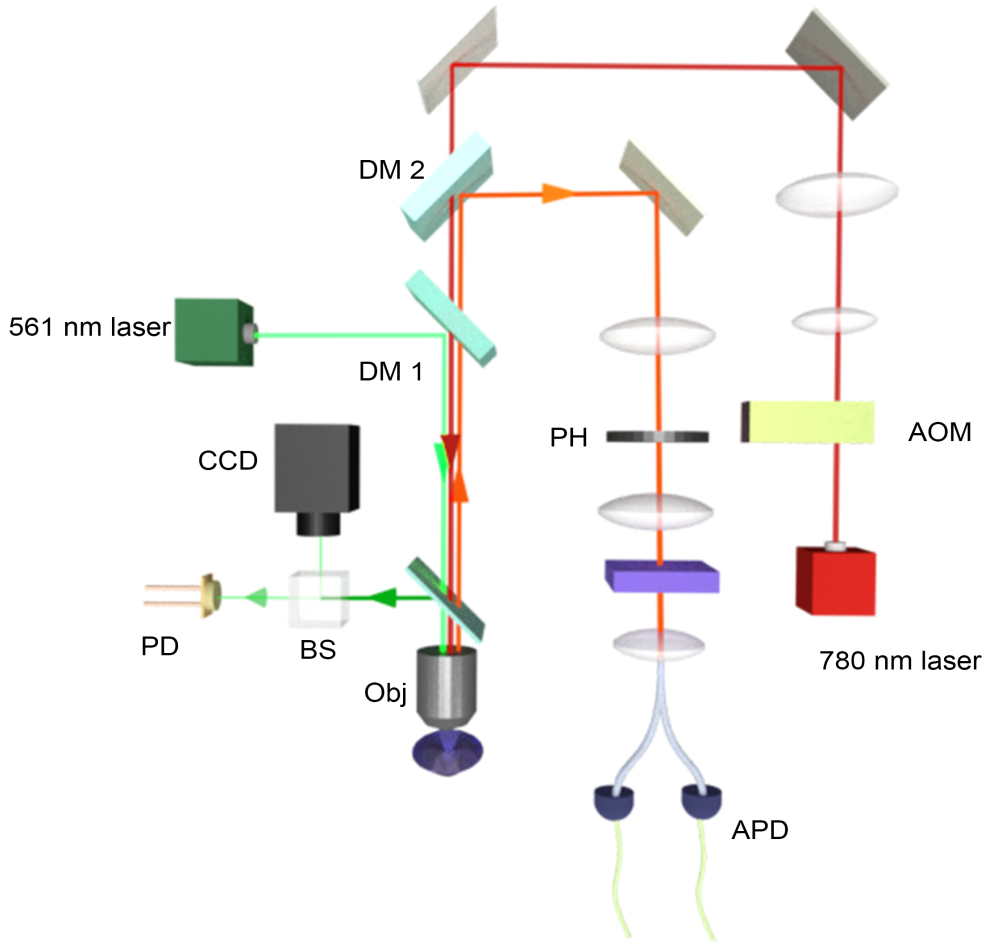


**Figure 3.1: Layout of the integrated setup**. The setup mainly consists of 561 nm cw laser (green path), 780 nm femtosecond laser (red path), acousto-optic modulator (AOM), CCD camera, silicon photodiode (PD), beam-splitter (BS), objective lens (Obj) dichroic mirrors (DM1, DM2), pinhole (PH) and two avalanche photon diode (APD). Also, the detection path is sketched (orange color)

To suppress the pump light, a long-pass filter with a cut-on wavelength of 650 nm (FEL0650, Thorlabs GmbH) is used. The fluorescence light is then focused onto the input of the Y-shape 50/50 fiber (MM coupler grade A, Laser Components) coupler. The two fiber splitter outputs are mounted onto two single photon avalanche photodiodes (τ-SPAD-100 from PicoQuant) forming an HBT setup to measure the second-order correlation function verifying the single NV center. Electric signals generated by APDs are sent to time-tagging electronics (TimeHarp 260 from PicoQuant) connected to a computer. There are two software used for the second-order correlation measurement: one is a commercial Time-Correlated Single Photon Counting model from PicoQuant and the other is home-built Fluorescence Correlation Spectroscopy

software by PD Dr. Andreas Naber.

The red path in Figure 3.1 indicates the DLW optical path with the femtosecond laser. To get a higher writing resolution result, the laser focused spot radius is supposed to be much closer to the Abbe diffraction limit [112]: $d = \text{wavelength}/2\text{NA}$. A higher NA can be experimental realized by collimating the first order of the diffracted laser from the AOM by a beam-expander telescope lens set which enlarges the laser diameter to $2\ \text{mm}$ to fully fill the objective lens entrance pupil. The software used for DLW is originally designed by Dr. Joachim Fischer and modified by integrating the functionalities for characterization of single-photon sources.

## 3.2. Optical path alignment

When using two lasers, it is important to know the axial and lateral displacements between the foci of two lasers. And the displacement correction is essential as it responses to the main experimental error afterwards. Here presents a method to calibrate two laser beams invited by Dr. Joachim Fisher.

In the ideal case, the two laser beams should be recognized simultaneously to avoid the drift of the sample. The drift of the sample is pronounced when the translation stage moves while switching the samples. The drift can last up to several hours until the steady state. In this case, the drift changes the experiment spatial coordinate with time and leads to an error if the calibration of two laser foci is in two separate experiments. A simultaneous calibration process in one step can eliminate the relative displacement error. However, it is not possible to distinguish two lasers by directly measuring the focus image on the camera or the laser intensities. One can circumvent this problem by coding the two lasers differently. In our work, the two lasers signals are modulated with the same frequency but orthogonal initial phases. Thus, the detected light from two sources are discriminated after demodulation.

The two laser beams are focused on the sample by the high NA objective lens. To calibrate the spatial position of the two focuses, single gold beads with spherical shapes are used to highly scatter the focused laser lights. The gold beads have diameters of around $80\ \text{nm}$ which are point-like probes compared to the focus volume of the laser. When preparing the calibration sample with gold beads, two requirements have to be fulfilled. Firstly, gold beads are required to distribute separately on the surface of the substrate without movement over time. Secondly, the environment around gold beads should mimic the one in the experiment later. Namely, the surrounding refractive index should be close to uniform and match the refractive index of the material in later experiments. Here, the gold beads aqueous suspension is first spin-coated onto a glass substrate. The distributed gold beads are fixed by Van der Waals force on the surface.

Subsequently, the sample is covered with the chosen photoresist (referring to Chapter 4) monomer pentaerythritol triacrylate (PETA) with a refractive index of $n = 1.484$. This cover layer modifies the refractive index of the environment and reduces the reflection of the interface between glass and air. The detection scheme is depicted in Figure 3.2 (a).

The calibration sample is fixed on the stage for linear scans of the gold beads in three dimensions. The focused laser light is highly backscattered when it hits the gold bead. The backscattered light is collected through the objective lens and detected by a silicon photodiode (Thorlabs FDS 100). To improve the accuracy of detection, two laser beams are firstly modulated by two synchronous-square-waves electric signals generated from two arbitrary-waveform generators (Hewlett Packard 33120A). The square-wave signals have $4\,\mathrm{kHz}$ frequency and they are synchronously triggered by one reference signal generated from a lock-in amplifier (Stanford Research Systems SR830 DSP) with the same frequency. Therefore, backscattered lights detected by the photodiode during the linear scan are modulated. And the lock-in amplifier demodulates and extracts electric signals carrying $4\,\mathrm{kHz}$ frequency from the photodiode signals according to the reference signal. In this way, ambient light signals without modulation are filtered and thereby to improve the signal-to-noise ratio. The electric signals of two laser beams from the lock-in amplifier are fed into two channels of a data acquisition device (National Instruments Corporation) which sends signals to the computer via a PCI card. It is discussed above that the two laser beams are better recognized simultaneously. For this purpose, a phase shift of $90^{\circ}$ is added to the $780\,\mathrm{nm}$ laser beam by the arbitrary-waveform generator such that even with one photodiode to detect backscattered light from both lasers, the lock-in amplifier can still discriminate the one in phase and the other one with orthogonal phase modulation with respect to the reference signal.

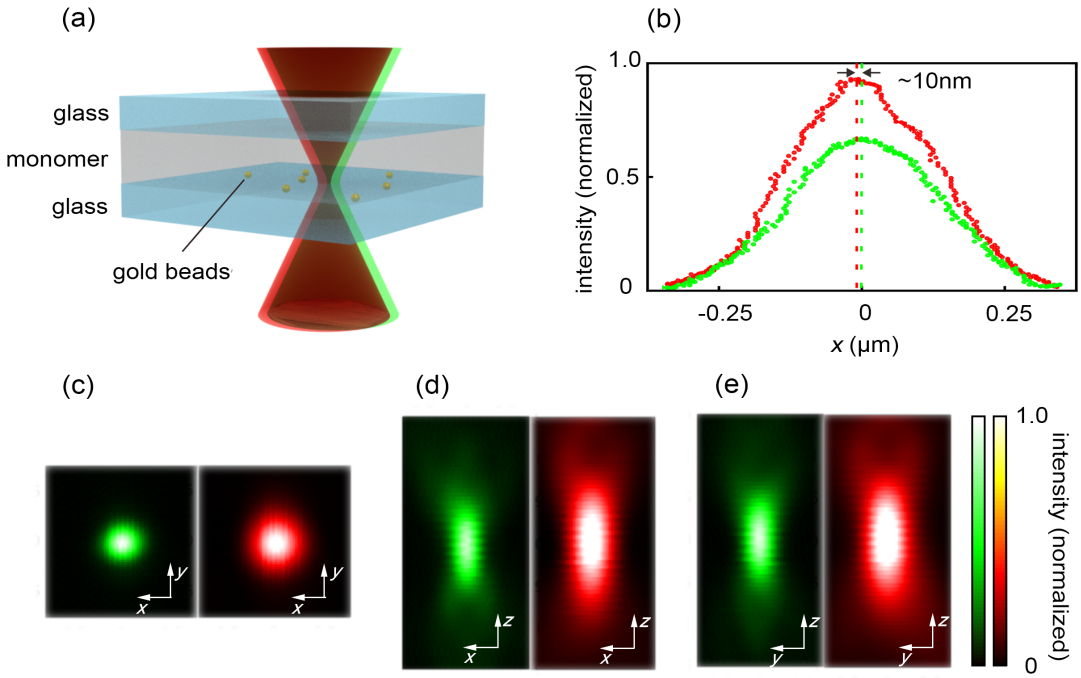


**Figure 3.2: Laser foci alignment**. **(a),** Sketch of the layout of the experiment. The gold spherical beads are spin-coated on the glass covered by a layer of monomer. One additional glass foils the sample being a standard alignment specimen. The femtosecond laser and the cw laser foci are modulated out of phase by 90° in order to simultaneously scan the gold beads layer and the back-scattered light are detected by a silicon photodiode. **(b)** plots the line scan experiment data around a single gold bead along the lateral *x* direction. The fit for two sets of data indicates a 10 nm relative offset between two foci which is within the accuracy range. Furthermore, the focus intensity profiles for planar scans of the gold beads are shown for an *x*-*y* **(c)**, *x*-*z* **(d)** and *y*-*z* **(e)** plane for both laser foci respectively.

Figure 3.2 (b) shows the exemplary line-scan data sets of the calibration process in one direction. The peaks of the two signals indicate the center positions of the gold bead found by two lasers. The experimental repeatability is about 20 nm. The home-build software is designed by Dr. Joachim Fisher. With this method, the spatial shift of two laser foci is measured in 3D by three scanning procedures. The lateral displacement is corrected by tilting one mirror at the optical path, followed by the collimation of the beam by adjusting the second mirror. The axial error is corrected by moving the lens of the beam-expander telescope along the propagation axis of the femtosecond laser. It requires several repetitions of both beam alignment processes to achieve two collimated beams with a relative displacement of below 20 nm. The beam profile is visible by displaying the three-dimensional data set as shown in Figure 3.2 (c)-(e) for both beams.

## 3.3. Sample preparation process

For the implementation of two integrated processes in this work, some additional requirements on the sample especially on the photoresist, which are particularly discussed in Section 4.1, need to be fulfilled. Here presents the procedure for the sample preparation.

The photoresist mostly used in this work contains pentaerythritol triacrylate (PETA) as the monomer (Sigma-Aldrich) and Irgacure 819 (BASF) as the photoinitiator. This photoresist recipe is denoted as LP in the following thesis. The work process requests immobilization of NDs in the photoresist. The liquid mixture LP cannot prevent NDs from drifting around. The solidification of LP can be accomplished by Polymethyl methacrylate (PMMA). However, it takes tens of hours to dissolve PMMA powder directly in LP. This problem is solved by employing acetone as an intermediate solvent. Acetone is miscible with water and compatible with the photoresist. It dissolves the PMMA powder within 2 hours with the aid of magnetic stirring. The amount of the acetone is not crucial because it evaporates afterwards in the spin-coating process. The PMMA solution is then mixed into LP with 20% weight fraction. This mixture is denoted as SP in the following thesis. The viscosity of SP can be modified by heating and stirring process for a certain time. Normally, SP gets highly viscous after 1 hour of treatment. The viscosity influences the thickness of the photoresist layer used for the experiment. If a thin layer of solid photoresist is required, more acetone is added into SP, which accelerate the spread speed of the photoresist layer in the spin-coating process. One fundamental fact realizes this work is that SP does not get polymerized by the 561 nm cw laser within the power range used for the laser scanning confocal fluorescence microscope.

In our experiment, the commercial NDs aqueous suspension from Microdiamant AG is used. However, when directly mixed with photoresist, it causes unexpected local explosions in the DLW process because of the water and the aggregation of NDs. Furthermore, impurities, especially the ones attached to the surface of the diamond nanocrystals, exhibit high bleachable fluorescence emission intensity under excitation. This impedes searching and localizing of single NV centers. The purification of NDs can be achieved by a well-established process involving multistage chemical treatment [113-114]. Here, several steps of physical treatments are implemented to extract NDs from the aqueous suspension into isopropanol or acetone with less impurities. The NDs suspension is first mixed with isopropanol or acetone with 1:1 volume ratio. Isopropanol is also miscible with water and LP photoresist, but compared to acetone it is less erosive to SP. Thus, NDs in isopropanol suspension are suitable for spin-coating on an existing SP layer. The mixed NDs suspension is at first subjected to an ultrasonication treatment for 2 hours to reduce the aggregation of NDs with a size above 200 nm [115]. Then the suspension is centrifugated at 1500 rpm for 30 mins to separate NDs with still remaining visible particles and other contaminants

which form the sedimentation at the bottom after the centrifugal. After this treatment, only the ultra-fine ND particles with a diameter below 100 nm remain in the suspension. The upper part of the suspension is then diluted with pure isopropanol or acetone to dilute the water. After five-fold repetition of this purification process, a colloidal suspension containing evenly dispersed ND particles is obtained as shown in the 3D laser scanning confocal fluorescence image of Figure 3.3. Details about the experiment are described in Section 3.4.

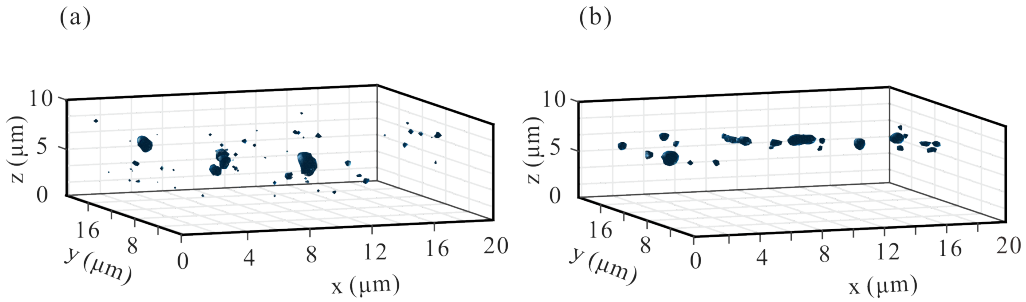


**Figure 3.3**: **3D visualization of the laser scanning confocal fluorescence images of two types of samples.** Emitters are shown with the dark blue iso-intensity surface. **(a)**, In the mixed sample, NDs are distributed in the volume of the solid photoresist with arbitrarily fixed 3D positions. **(b)** shows the experiment of a sandwich sample, which contains two layers of photoresist clamping one layer of NDs. Emitters are well confined in a horizontal layer at a certain height with around 1 μm accuracy.

With the well-prepared photoresist, SP and NDs suspension, two types of samples with different preparation procedures are prepared for distinct purposes: the mixture mode and the sandwich mode.

For the mixture mode as shown in Figure 3.3 (a), the pre-treated NDs-acetone suspension is mixed with SP. The mixture can be spun on the glass substrate or simply cast onto it. After evaporation of acetone, the mixture turns to solid with fixed positions of the embedded NDs.

In the sandwich mode sample as shown in Figure 3.3 (b), just as the name implies, NDs are well dispersed in a layer within the SP with nearly uniform height. The inserting of an ND layer involves two steps. First, one layer of SP is spin-coated on the glass substrate. The thickness is controlled by the process parameters as well as the viscosity of SP. For example, the procedure of spin-coating the SP contains 30% volume of acetone with 4000 rpm for 30s forms an SP layer with a thickness of 5 nm. Second, the pre-treated NDs suspension in isopropanol is spun on the top of the sample and is subjected to spin-coating of another layer of SP.

It should be mentioned that the ND particles suffer from severe agglomeration with

ambient amorphous carbon and nanoparticles. But the ultrasonic treatment is not sufficient to eliminate all the agglomerates. The degree of agglomeration can be significantly reduced by laser treatment [116]. Additionally, the density of isolated NDs in the photoresist can be increased by enhancing the solubility of the NDs in organic solvents using surfactants [117]. However, in our experiments, a colloidal suspension with a high density of isolated single NDs is not crucially required. The primarily treated suspension with the method described above fulfills the requirement of localizing isolated single NV centers with clean surrounding in a relatively large volume.

## 3.4. Localization of NV centers

With the help of the integrated setup demonstrated in Section 3.1, one can find out the presence of single NV centers on the sample and subsequently characterize them. In this section, the procedure of NV center localization which can be automatically controlled by the computer program is introduced.

With the setup, planar zigzag-raster laser scanning is performed within the range of $20\ \mu m \times 20\ \mu m$ with a small raster pitch. At each pitch step, the instantaneous fluorescence intensity is detected by the APD, and simultaneously the position information is collected from the feedback of the piezoelectric stage controller. Due to the intrinsic electronic error and the mechanical delay of the stage, the position data collected are not exactly the same as the commands sent to the controller, and thus when forming the fluorescence map directly by the raw data, the edge of the map shows sawtooth error between adjacent line scanning. Therefore, the data of $2\ \mu m$ near each edge are abandoned and the raw position data are binned with averaged surrounding fluorescence intensity, which results in the reformed fluorescence image of $16\ \mu m \times 16\ \mu m$. Figure 3.4 demonstrates an exemplary 2D laser scanning confocal fluorescence image in a mixture sample prepared as described in the preceding section. The potential photon emitters are automatically recognized by a computer program. It searches for the brighter area in the 2D scanning data set and fits each intensity distribution with a 2D Gaussian distribution function. One well-fitted emitter is indicated by the red circles in Figure 3.4 (a).

The 2D fluorescence image intuitively indicates the emitter distribution at this layer. A 3D visualization of the fluorescence intensity within a certain volume is realized by reconstructing successive 2D planar fluorescence images of multiple layers along the vertical axis. Figure 3.3 in the last section shows the exemplary 3D visualization of a sandwich mode sample and a mixture mode sample, respectively.

However, from these fluorescence images, one cannot read the bleaching information and the precise location information of each emitter. In the next step, the sample is moved to the position where the laser focuses at each circled emitter and subjected to line scanning in three dimensions. The stage movement speed, in this case, is much slower to achieve higher accuracy. Fluorescence intensity is detected by one APD. Figure 3.4 (b)-(d) show the exemplary data set. The three plots are three line scans in $x, y, z$ direction, respectively. After fitting the data set by the Gaussian distribution, one can extract the center position of each emitter. Emitters which are bleachable exhibits down going trend of the fluorescence intensity in the successive scanning sets and are discarded. This eases the following process for determination of single NV centers because of the high photostability of them.

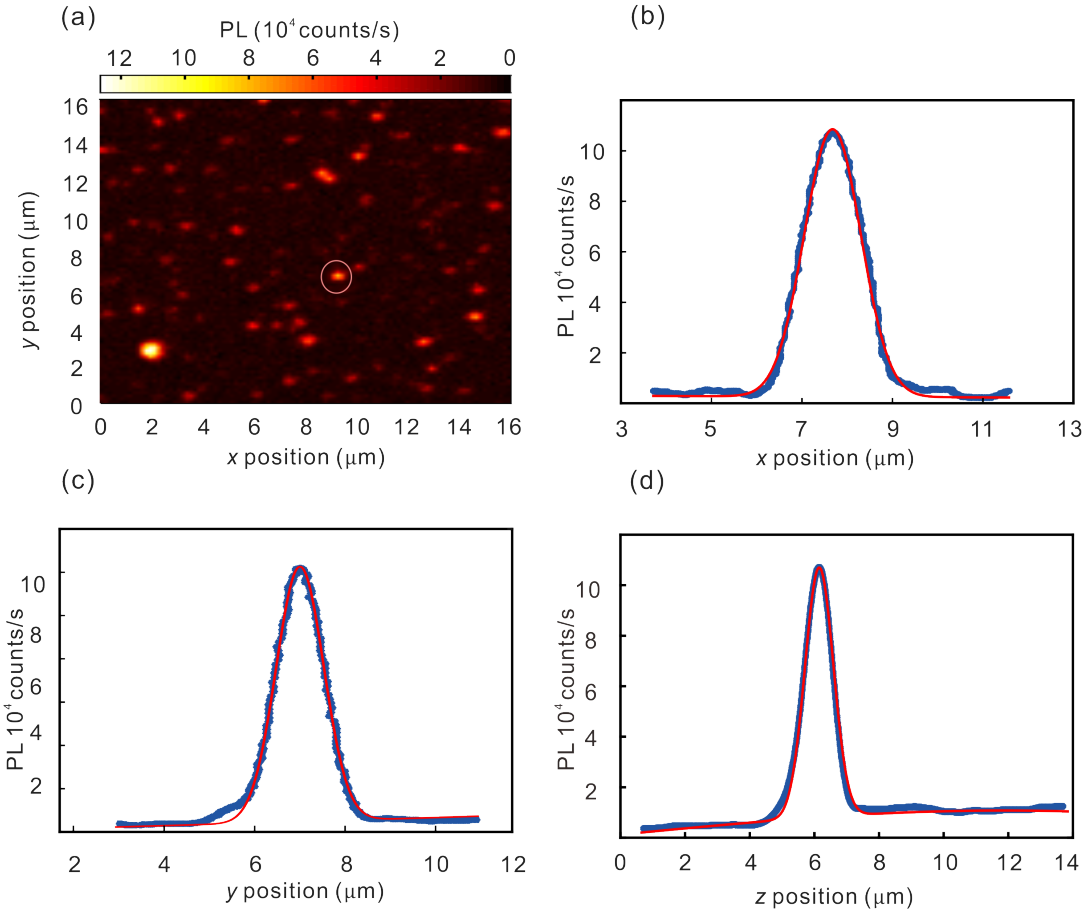


**Figure 3.4: Confocal laser scan of NV center sample in the photoresist. (a)** is an exemplary fluorescence intensity map in the lateral plane. The sample was scanned with a 561 nm cw laser at the power of 100 μW. Bright spots in the map indicate the fluorescence emitter with the circled one pre-fitted by the Gaussian distribution. The line scan data of which in *x, y, z* directions are plotted with blue dots in **(b)**, **(c)** and **(d)**, respectively. The red lines in *x, y* directions **(b)**, **(c)** are fit curves according to a Gaussian profile based on a constant fluorescence background. The fit for the vertical direction **(d)** is performed based on a Gaussian profile pluses a step signal corresponding to the fluorescence difference between the glass and the photoresist.

In this way, information including the average intensity and the position of each NV center candidate are automatically recorded on the computer. Afterwards, an electric signal is sent to the Time Tagging Electronics card (TimeHarp 260, PicoQuant) which automatically triggers the second-order correlation measurement. At each emitter position, the excitation laser is turned on and the fluorescence light is collected and guided into two silicon APDs via a 50%:50% Y-shape splitting fiber coupler. However, there exists a fluorescence cross-talking between two silicon APDs. Photon detection events cause an emission of the silicon atoms in each APD and the

fluorescence photons are guided by the Y-shape fiber to the other one, which is shown as the coincident events in the gray areas in Figure 4.5 (a). For each emitter candidate, the measurement time scale is $300s$ for less time-consuming and the raw data are saved to the computer disk for further manually examining. A standard $g^{(2)}(\tau)$ data is shown in Figure 3.5 (a) with a dip down to $0.21 < 0.5$ indicating the single-photon emission. The satruation of the emission is shown in Figure 3.5 (b) (refering to Section 2.2.1), where the NV center of interest is excited with increasing laser intensity. And the fluorescence intensity are collected by the APD. For each saturation experiment, the background light obtained from a reference sample or an adjecent position are subtracted from the NV center fluoresncece.

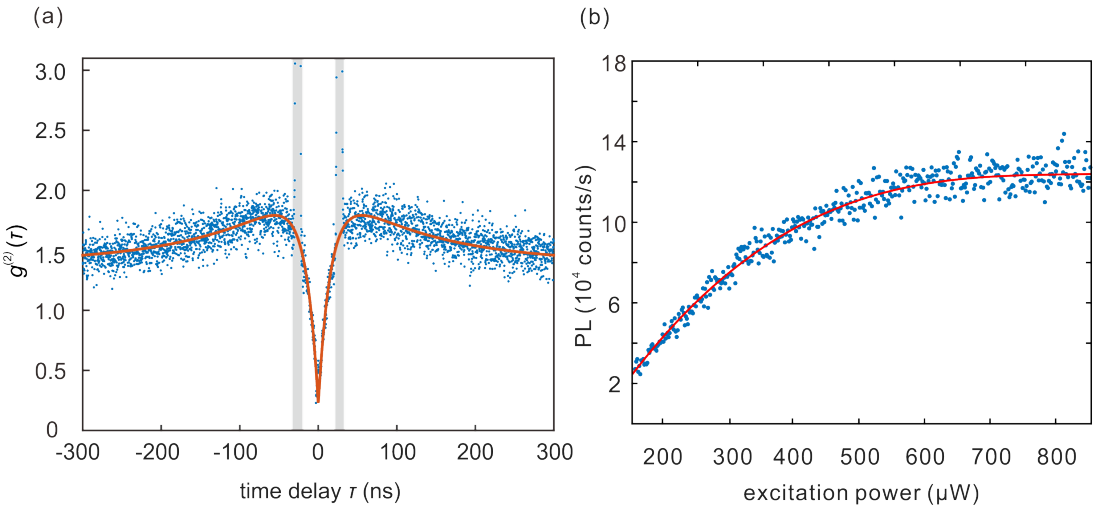


**Figure 3.5**: **Illustration of NV center characterization. (a),** For each NV center candidate, the second-order correlation measurement is performed with HBT setup**.** The data are fitted according to the three-level model (referring to Section 2.2.1) as shown by the orange curve. The two gray areas indicate the photon events generated from the cross talk between two APDs. **(b)** plots the photoluminescence (PL) intensity versus excitation laser power. The red curve is a fitting according to the three-level model of NV center (referring to Section 2.2.1).

## 3.5. Determining the orientation of NV-center dipoles

For the application of NV centers, it is useful to determine the orientation of the optical transition of NV centers to maximize the coupling efficiency. The fluorescence of NV center is related to two degenerate dipoles which are orthogonal to each other and they form a plane perpendicular to the NV symmetry axis [59] as shown in Figure 3.6. Previous work of [118] demonstrated the experiment to determinate the orientation of a molecular single dipole by using linearly polarized excitation light. A similar approach is used here with the integrated setup to evaluate the dipole orientations of an NV center by measuring the polarization-dependent fluorescence intensity modulation depth (PDMD). In the following, the theory based on the model of the NV center is deduced and then implementation of the experiment using the integrated setup is described.

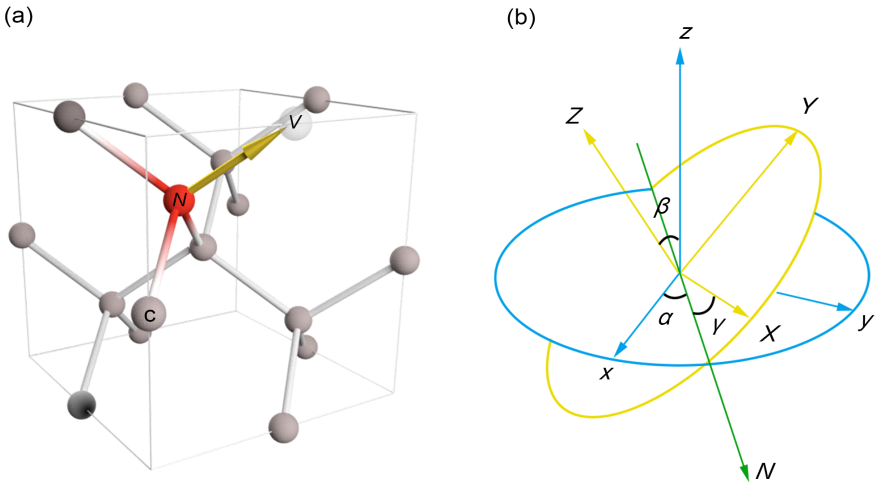


**Figure 3.6**: **Orientation demonstration of dipoles in the NV center**. **(a)** shows the lattice structure of the NV center in diamond. The nitrogen atom, vacancy and the carbon atoms are denoted by the red, semi-transparent and gray spheres respectively. **(b)** illustrates the spatial orientation of the two orthogonal dipoles of the NV center by the Euler angles with respect to the lab frame $(x, y, z)$ and the rotated NV center coordinate is denoted by $(X, Y, Z)$. $Z$ indicates the NV axis and the $X$ and $Y$ indicate the two degenerate dipoles. The two degenerate dipoles form a plane intersecting with the lab frame $x - y$ plane. The Euler angle $\alpha$ is the angle between the intersection line $N$ with $x$ axis. $\beta$ is the angle between the NV axis with the $z$ axis of the lab frame. $\gamma$ is the angle between the intersection line $N$ with one of the NV dipoles.

Figure 3.6 (b) shows the orientation of the two dipoles, where α, β and γ are the Euler angles of the NV coordinate with respect to the lab coordinate system. In the diamond nanocrystal, the NV axis is orthogonal to the plane formed by the two degenerate dipoles. The three axes form a new coordinate system $XYZ$ where two dipoles are along $X$ and $Y$ respectively.

Here the unit vectors $\hat{u}_1$ and $\hat{u}_2$ are used to represent the two dipoles. Based on the coordinate transformation, $\hat{u}_1$ and $\hat{u}_2$ can be transformed from the original $XYZ$ coordinate to the lab coordinate frame as [152]:

$$\hat{u}_1 = \begin{pmatrix} \cos\alpha\cos\gamma - \sin\alpha\cos\beta\sin\gamma \\ \sin\alpha\cos\gamma + \sin\gamma\cos\alpha\cos\beta \\ \sin\beta\sin\gamma \end{pmatrix},$$

$$\hat{u}_2 = \begin{pmatrix} -\cos\alpha\sin\gamma - \sin\alpha\cos\beta\cos\gamma \\ -\sin\alpha\sin\gamma + \cos\alpha\cos\beta\cos\gamma \\ \sin\beta\cos\gamma \end{pmatrix}, \tag{3.5.1}$$

$$\vec{e}_{linear} = \begin{pmatrix} \cos\vartheta \\ \sin\vartheta \\ 0 \end{pmatrix},$$

$$\vec{e}_{circular} = \begin{pmatrix} \sqrt{2} \\ \sqrt{2}i \\ 0 \end{pmatrix},$$

where $\vec{e}_{linear}$ is the unit vector of the linearly polarized electric field and $\vec{e}_{circular}$ is the unit vector for the circularly polarized excitation electric field of the excitation light. The linearly polarized light is in the $x-y$ plane of the lab frame enclosing the angle $\vartheta$ as the polarization direction with respect to the $x$ axis. In the coordinate transformation process, one already has $\alpha$ to determine the relative angle between the dipoles and the $x$ axis. For simplification, it is assumed that the excitation light is always along the $x$ axis which corresponds $\vartheta = 0$.

For linear polarized light, the fluorescence intensity is proportional to the coupling between the two dipoles and the excitation light as:

$$I \propto (\hat{u}_1 \cdot \vec{e})^2 + (\hat{u}_2 \cdot \vec{e})^2 = 1 - \sin^2\alpha \cdot \sin^2\beta, \tag{3.5.2}$$

where $\alpha$ changes when rotating the excitation polarization in $xy$ plane.

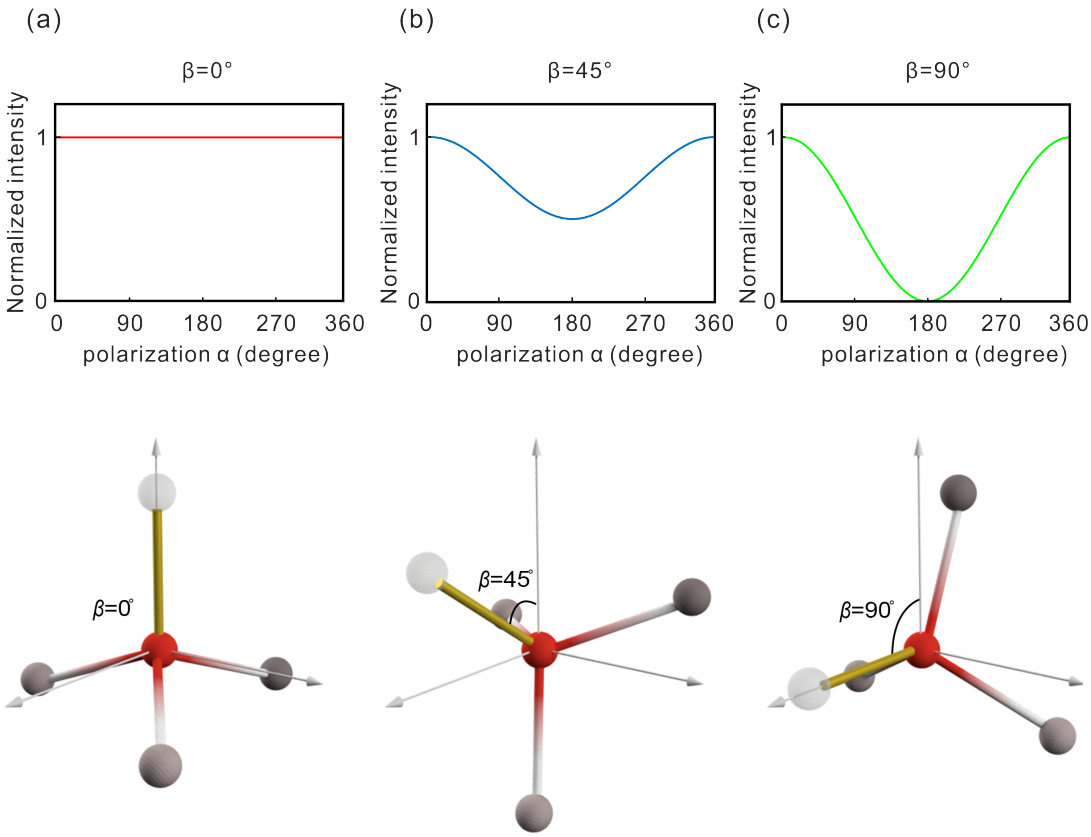


Figure 3.7: **Simulation of fluorescence intensity with rotated excitation polarization for different NV-dipoles orientations.** The NV dipole orientations are rotated by $0°, 45°$ and $90°$ in (a), (b) and (c), respectively. The fluorescence intensity variation upon rotated excitation polarization in the horizontal plane is shown in the upper row. The corresponding NV center orientation angles with respect to the lab frame are sketched in the lower row.

A circularly polarized excitation light i.e. $\vec{e} = (\sqrt{2},\ \sqrt{2}i,\ 0)$ leads to the analogous to equation (3.5.2):

$$I \propto (\hat{u}_1 \cdot \vec{e})^2 + (\hat{u}_2 \cdot \vec{e})^2 = 1 + \cos^2 \beta, \tag{3.5.3}$$

However, the values of $\alpha$ and $\beta$ in the equation (3.5.2) cannot be easily determined because the absolute magnitude of the coupling intensity is generally unknown. This can be solved by defining a polarization dependent fluorescence intensity modulation depth (PDMD) as:

$$P = \frac{I_{max} - I_{min}}{I_{max} + I_{min}} = \frac{1 - \cos^2 \beta}{1 + \cos^2 \beta}, \tag{3.5.4}$$

Thus, the Euler angle $\beta$ of a fixed NV center determines the varying range of the fluorescence intensity. The PDMD can be recognized and read out from the fluorescence intensity variation during changing the polarization of the excitation in the $x - y$ plane. In the case of NV-axis perpendicular to the polarization plane ($\beta = 0$), the fluorescence intensity exhibits no variation when rotating the polarized excitation laser, whereas in the case where the NV-axis is parallel to the polarization plane ($\beta = \pi/2$), the polarization modulation depth is unity. The simulation of the modeling is presented in Figure 3.7.

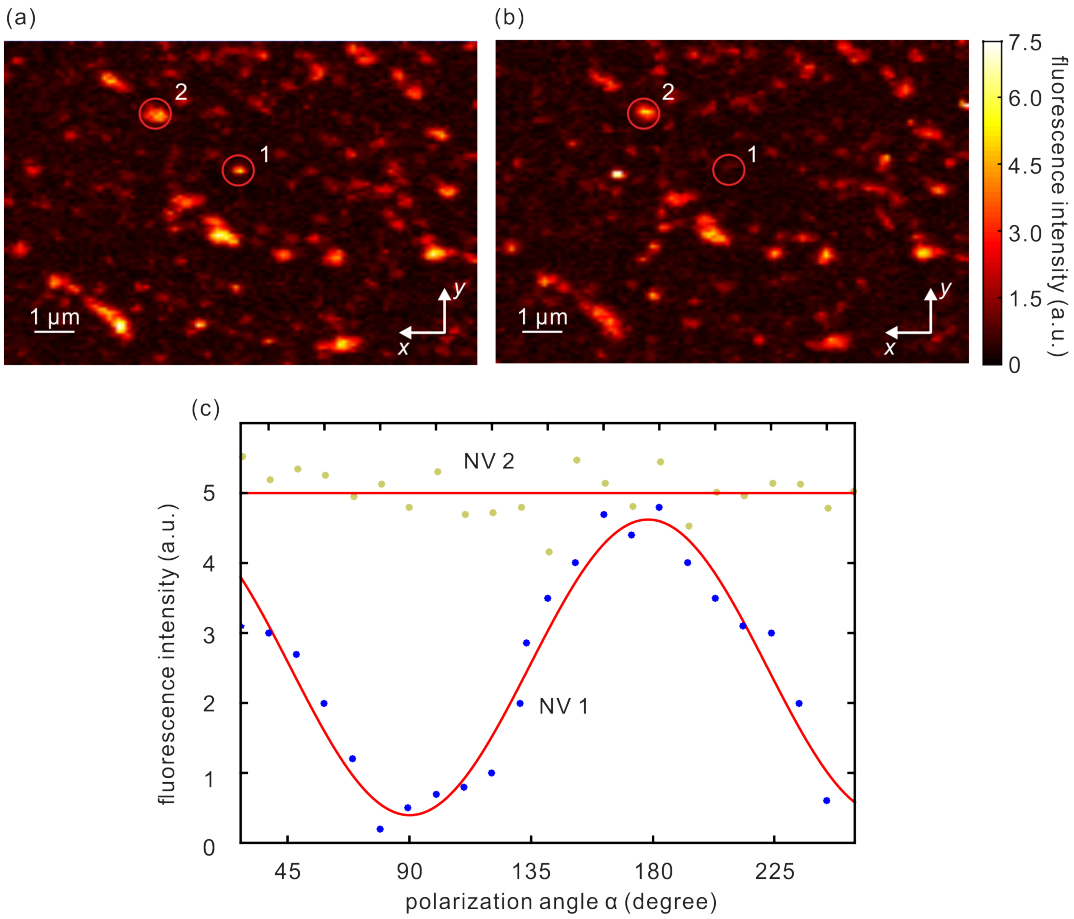


**Figure 3.8: NV center orientation determination by the optical polarization dependence. (a)** shows a laser scanning confocal fluorescence image. The bright spots are emitters and the circled two are single NV center candidates labeled by 1 and 2. **(b)** shows the scanning confocal fluorescence image of the same area with the polarization of the excitation laser rotated by 90°. The NV 1 and NV 2 are indicated by circles. Fluorescence intensity of NV 1 is clearly dimmed whereas the fluorescence intensity stays almost the same with the orthogonally polarized

excitation laser. The measurement data of fluorescence intensity of NV1 and NV 2 versus polarization angle is plotted in **(c)**. The red curves are produced by fitting the theoretical model to the data. The excitation laser power is below the saturation power.

Experimentally, the linearly polarized laser is modified by a half-wave plate fixed on a rotatable mount at the optical path. The power used in the experiment is 100 μW which is required to stay below the saturation power (the definition and methods are explained in Section 2.2.1) of an individual NV center. The sample is prepared as described in Section 3.3. NDs are pre-treated and evenly dispersed in the photoresist SP (see Section 3.3) and the mixture is drop-casted on the glass substrate. The sample is characterized on the integrated setup as described in Section 3.1. The fluorescence map is shown in Figure 3.8 (a). Each potential emitter is subjected to the second-order correlation measurement with the aid of the HBT setup, followed by a background correction (see Section 2.2.1) to confirm the single-photon emission. The characterized emitters with $g^{(2)}(0) < 0.5$ indicating the single-photon emission are selected. Subsequently, the half-wave plate is successively rotated to change the polarization of the excitation light with steps of $15^{\circ}$ and the fluorescence count rate is recorded by APD.

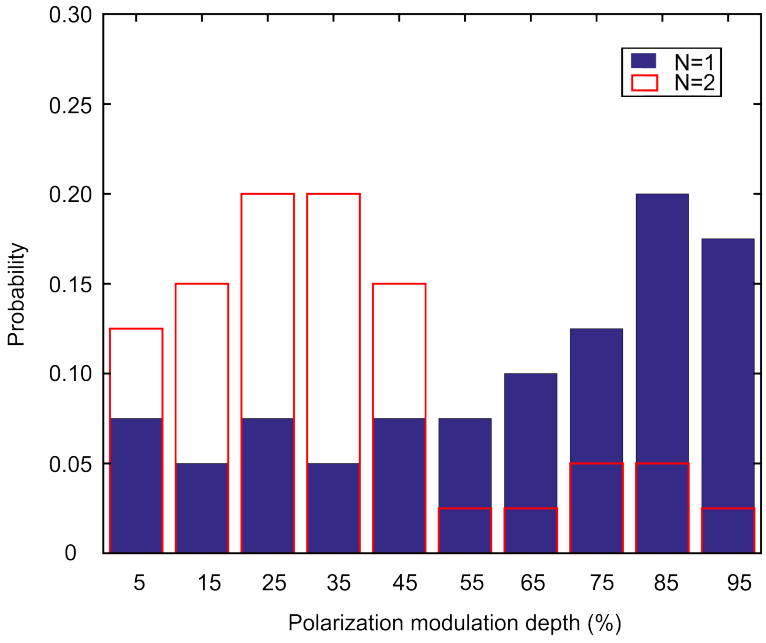


**Figure 3.9**: **The statistic of polarization dependent modulation depth of single NV centers and double NV centers.** The blue bars indicate the single NV centers with $g^{(2)}(0) < 0.5$ in the second-order correlation measurement. And the red frames indicate the double NV centers with $0.67 > g^{(2)}(0) > 0.5$, where 0.67 is the calculated $g^{(2)}(0)$ value of double NV centers referring to equation (2.1.30). All $g^{(2)}(0)$ values are corrected from the background fluorescence (referring to Section 2.2.1)

Two NV centers with polarization dependent fluorescence modulation behaviors are depicted in the fluorescence images of Figure 3.8 (a) labeled as 1 and 2. Figure 3.8 (b) shows the image of the same area but with the excitation polarization rotated by $90^{\circ}$. Comparing the two images, one can find that NV 1 shows undetectable fluorescence intensity after rotation while the other emitter NV 2 remain as before. The statistic measurements of fluorescence intensity with continuously changed laser polarization on NV 1 and NV 2 are plotted in Figure 3.8(c). One can see that the NV 1 expresses highest fluorescence intensity but the least modulation depth. According to the model described above, two NV dipoles are equally coupled with the excitation laser which is approach to the model of $\beta = 0$. The NV 2 exhibits more modulation depth but less intensity because the dipole moment projected onto the polarization plane is small. The PDMDs are derived from the fitting model. NV 1 shows PDMD value of $80\%$ and NV 2 shows a PDMD value of $0$, which corresponding to $\beta = 70.52°$ and $\beta = 0°$ respectively.

In order to perform statistical analysis, 40 single NV centers and 40 double NV centers are characterized. Their characters as a single NV center or double NV centers is proved by the background-corrected $g^{(2)}(0)$ value. The PDMD is measured on each one. The statistics of PDMD is shown in Figure 3.9. It can be predicted that the double NV center has two sets of degenerate dipoles, therefore the probability to find deep modulation for a double NV centers is much less than for a single NV center.

In this chapter, integrated setup combining two functionalities of DLW and NV center characterization is shown. The characterization process introduced above provides pre-characterized NV centers with desired properties for the following on-demand fabrication of quantum-photonic components with high yield and accuracy. The relative positions of the structure and NV centers and can be independently and arbitrarily designed or chosen in 3D within the setup accuracy. Moreover, this characterization method is not restricted to NV centers in NDs but can be used for other single-photon sources such as silicon-vacancy center.

# 4.Photoresist challenges

Works in the thesis base on the idea and the experimental setup integrating the functionality of laser scanning confocal fluorescence microscopy and DLW. In this fashion, NV containing NDs can be localized in a first step and be integrated in the following lithographic step. However, such a setup gives rise to its own challenges. The sample used here consists of NDs in a negative tone photoresist. As described in Section 2.4.2, the photoresist is comprised of photoinitiator and a monomer. Usually, the former is photosensitive and exhibits fluorescence in the most cases. During confocal fluorescence microscopy, the single-photon emission must emerge clearly from the fluorescence background of surrounding excited photoresist molecules. On the other side, the laser scan microscopy should not polymerize the photoresist in advance. Another concern is that the experiment coordinated for NV centers must be fixed in both scanning and writing processes, which requires the unpolymerized photoresist to be solid or viscous enough to restricting the NDs from floating or sinking.

In this chapter, photoresists are characterized and selected from several candidates concerning the aspects described above.

## 4.1. Fluorescence of photoresists

In a negative photoresist system, photoinitiator can absorb light of a particular wavelength to generate active free radicals or strong acids [103], which can convert the monomers into an insoluble form typically by undergoing an increase in molecular weight or by the formation of a new insoluble cross-linked network. The photoinitiator plays a very important role in the negative-tone photoresist, and many efforts have been directed at the development of photoinitiator systems to achieve a proper dynamic range, higher resolution and less local explosions [119-120].

However, one of the problems affecting the performance of the photoresist in the quantum-photonic application is the fluorescence. Fluorescence is an optical phenomenon that occurs when a molecule absorbs light at a particular wavelength and subsequently emits light at a longer wavelength. Upon exposure to an excitation radiation, molecules absorb the photon energy to a higher energy state, followed by a depopulation of this state back to the lower energy state. This depopulation process is determined by the electronic configuration of the molecule [104] and can take place via the radiation transition, internal conversion and intersystem crossing. The depopulation occurs with an intrinsic decay lifetime which is the inverse of the sum of the rate constants ($k$) of all transition processes:

$$\tau^{-1} = \sum k = k_{radiation} + k_{isc} + k_{ic} + \cdots + k_{others} \,. \qquad (4.1.1)$$

The fluorescence behavior from different photoresist varies. For example, SU-8 is a widely-used photoresist in many applications. The main feature of SU-8 photoresist is to offer the high aspect-ratio, surface modification, and transparent observability for the complex 3D microfabrication. But SU-8 photoresist contains benzene rings exhibiting considerable fluorescence [105]. This effect is beneficial in bio-imaging applications but highly unwanted in the quantum-photonic field. If single-photon sources are embedded in or covered with SU-8 having high fluorescence, it is difficult to differentiate the target object from the photoresist resulting in the low contrast ratio (signal-to-noise ratio) and thus the quantitative analysis such as characterization of single-photon emission becomes difficult. Likely, final fabricated polymer components around single-photon emitters are also required to preserve the single-photon emission characteristic.

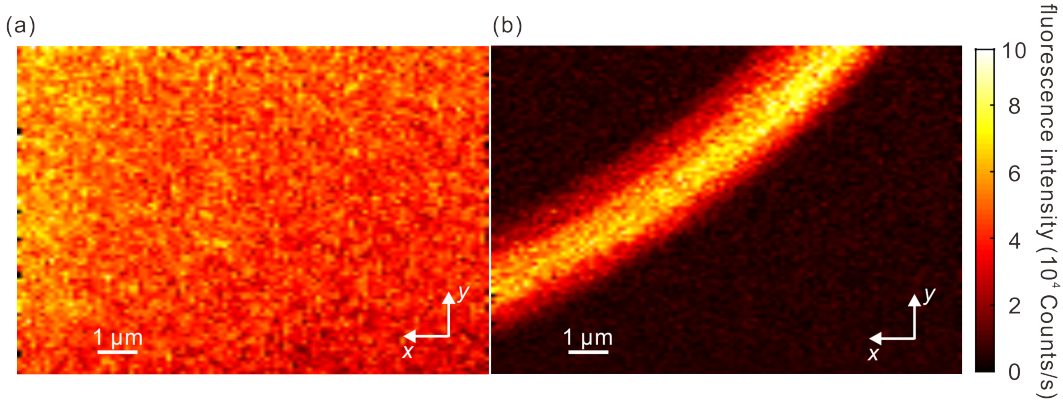


**Figure 4.1: Observation of fluorescence from SU-8 photoresist before and after being polymerized. (a)** is the laser scanning confocal fluorescence image of SU-8 photoresist as an example of photoresist with high fluorescence, and **(b)** is the laser scanning confocal fluorescence image of a laser written micro-structure using SU-8 indicated by the bright curve. In both cases, the unpolymerized photoresist and the polymer structure show high fluorescence hindering the localization of quantum emitters such as NV center which exhibits detected single-photon counts around $10^5$ counts/s.

Figure 4.1 (a) shows the laser scanning confocal fluorescence image of SU-8 (Microchem Corp) photoresist spin-coated on the glass substrate using a 561 nm cw laser with 100 µW power. The SU-8 exhibits inhomogeneous fluorescence intensity reaching up to $10^5$ counts/s which is in the same level of the count rate detected from the NV centers ($1.1\times10^5$ counts/s in the case of Figure 3.4). Such inhomogeneity is caused by several times of pre-scan at the right area. A micro-structure in the form of a polymer curve is fabricated on the sample by the DLW process and Figure 4.1 (b) shows

the laser scanning confocal fluorescence image after the sample is developed (the method is described in Section 2.4.3). The polymer curve on the glass substrate is clearly revealed by its high fluorescence count rate. Such background signal of the microstructures interferes with the accuracy of the observation of single photons in the experiment both before and after the structure is formed.

## 4.2. The photobleaching effect

Some photoresist and polymer molecules (normally with high fluorescence) are not photostable upon excitation exhibiting the photobleaching phenomenon. In contrast to the mechanism of fluorescence, photobleaching is the photochemical alteration of molecules or atoms after which they are unable to fluoresce. This effect is believed to be caused by cleaving of covalent bonds or non-specific reactions between the fluorophore and surrounding molecules such as oxygen [106]. Some irreversible modifications in covalent bonds involve the transition from a singlet-state to the triple-state of the fluorophores which cannot take part in the radiation process since they are spin--forbidden [107-108]. The excitation cycles accumulate over time and result in maximum bleaching to a steady state. The bleaching rate is a function of excitation intensity. For biological experiments, the photobleaching complicates the observation of fluorescent molecules, since they will eventually be destroyed by the light exposure.

## 4.3. Analysis experiments for photoresist fluorescence

Thanks to the previous work of Dr. Joachim Fischer [109], photoresist candidates with excellent writing performance have been characterized. In this section, the fluorescence property of the different photoresist recipes is examined.

As introduced in Section 2.4.2, the photoresist contains monomer and photoinitiator. To achieve a photoresist recipe with low fluorescence, the experiment starts with inspecting the fluorescence from the monomer. Three commonly used monomers are examined here: pentaerythritol triacrylate (PETA from Sigma-Aldrich), pentaerythritol tetraacrylate (PETTA from Sigma-Aldrich), and trimethylolpropane triacrylate (TMPTA from Sigma-Aldrich).

All glass substrates used are cleaned by ethanol, isopropanol and distilled water successively. The three monomers are liquid. In order to make sure that all photoresists are under the same experiment condition, the glass substrate is segmented into three sections by three solid Polydimethylsiloxane (PDMS) hollow circular rings with around 7 mm inner diameter. Each PDMS block contains one casted drop of each kind of photoresist. The whole sample is fixed on a piezoelectric stage for precise 3D movement.

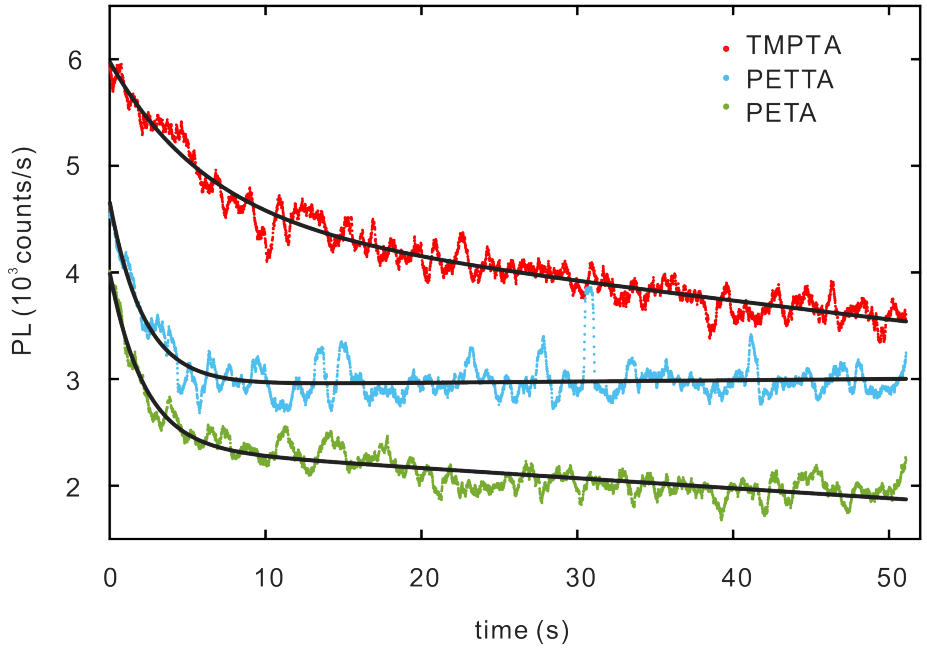


**Figure 4.2: Monomer bleaching experiment.** Under the confocal fluorescence microscopy, all monomers are pumped by the 561 nm cw laser at 250 μW. The dots are experiment data sets of photoluminescence intensity from TMPTA (red), PETTA (blue) and PETA (green). Black curves are the fits according to the biexponential model from reference [108].

The whole sample is fixed on the setup described in Section 3.1. And the monomer is pumped by the 561 nm cw excitation laser at 250 μW power. In this experiment, no pre-bleaching is performed on the photoresist. Around each PDMS segment, the piezoelectric stage moves such that the excitation light focuses into the photoresist volume with 7 μm above the interface between the monomer and the glass substrate. As a result of the confocal microscopy, photons detected by the APD are exclusively from the tight confocal volume. The fluorescence collection process lasts for 55 seconds. Figure 4.2 shows the experiment results for all three candidates, where the photobleaching effect of different photoresists are distinct but behave differently. The experiment data sets are fitted according to the biexponential model as described in reference [108]. From Figure 4.2, one can see that TMPTA shows higher fluorescence along with more prominent photobleaching and PETA show the least photobleaching. Comparing to the count rate from NV center which is on the order of $10^5$ counts/s, the fluorescence from these three monomer candidates is not crucial. It is confident to choose PETA as the monomer for the photoresist recipe in this work with minimally influence on quantum emitters fluorescence.

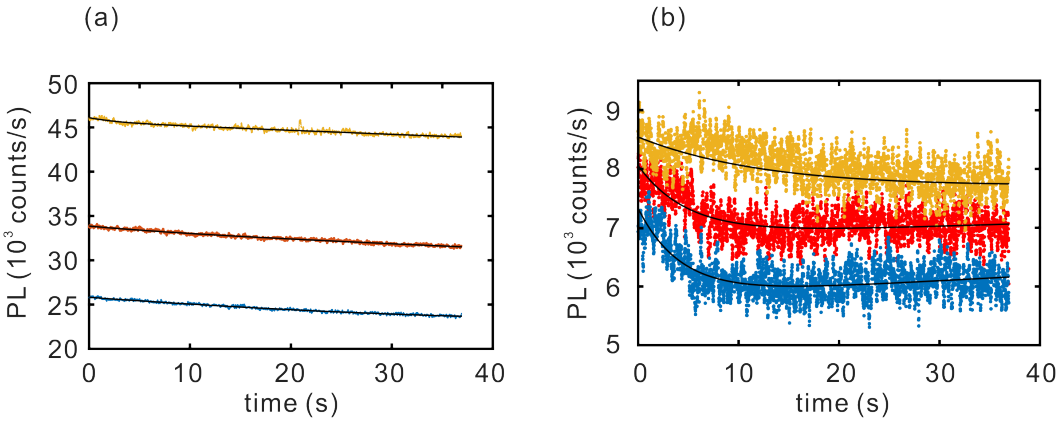


**Figure 4.3: Bleaching experiment for photoresists with PETA as monomer and different photoinitiators:** Irgacure 369 **(a)** and Irgacure 819 **(b)** at 1% (orange), 2% (red) and 3% (blue) concentration. Under confocal fluorescence microscopy, all monomers are excited by the 561 nm cw laser at 250 µW. **(a)** shows the photoluminescence (PL) of PETA mixed with Irgacure 369 of different concentrations versus time. **(b)** shows the PL of PETA mixed with Irgacure 819 of different concentrations versus time. The overall PL from Irgacure 819 mixture is around four times lower than the Irgacure 369 mixture. Gray curves are fits according to the biexponential model from reference [108].

The photoinitiator candidates for the PETA monomer can be Irgacure 819, Irgacure 369 and 7-diethylamino-3-thenoylcoumarin (DETC). DETC, however, has been proved to exhibit relatively high fluorescence in the work of Dr. Joachim Fisher [109] and thus can be abandoned. To inspect the contribution of the photoinitiator on the photoresist fluorescence, another sample is prepared on the glass substrate segmented again into six areas by the PDMS circles. Three of the PDMS hollow circular blocks are filled with the PETA mixed with Irgacure 819 in a weight ratio of 1%, 2% and 3%, respectively. The other three circular blocks are filled with PETA mixed with Irgacure 369 in a weight ratio from 1% to 3%. Afterwards, the same experiment as for the monomer is performed and the fluorescence intensity is compared. Figure 4.3 shows the experiment results. Photoresists with Irgacure 819 exhibit more than four times lower fluorescence intensity than the ones with Irgacure 369 with corresponding concentrations. In the case of Irgacure 369 mixture, photoinitiators contribute the fluorescence photoinitiators more than the monomer PETA, and with increasing concentrate of the photoinitiator, the fluorescence increases by a factor of 1.87. While for the Irgacure 819, three times concentration variation enhances the fluorescence intensity by a relatively lower factor of 1.2. In the case of comparable laser written quality, it is capable of choosing proper photoinitiator concentration to achieve desired writing thresholds without altering the accuracy of the fluorescence experiment. From the experiment above, the photoresist consisting of PETA as monomer and Irgacure 819

as photoinitiator has been found to be good candidate for our single-photon fluorescence experiment.

**Fluorescence from polymer structures:**

From the test above, a photoresist consisting PETA as monomer and Irgacure 819 as photoinitiator with low fluorescence is chosen. However, it is not necessarily equal to exhibiting a low fluorescence after polymerization, as during the DLW process the polymerization process involves chemically reacting monomer molecules together to form new polymer chains or three-dimensional networks [99]. The fluorescence of the polymerized structures needs to be examined. And the experiment is shown below.

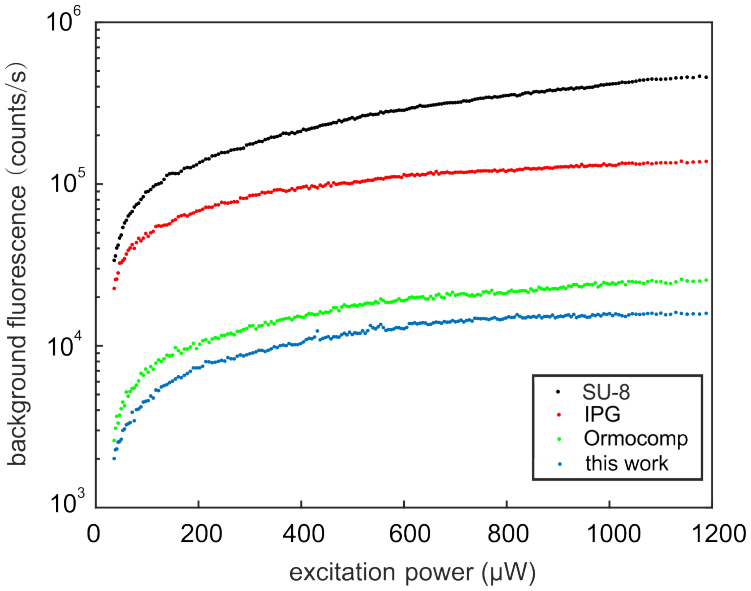


**Figure 4.4: Background fluorescence of four different photoresists.** Data points indicate SU-8 (black), IPG (red), Ormocomp (green) and the home-made solid resist introduced and described in this work (blue), respectively. The sample are bleached to steady state for each of the four photoresists. The recorded background fluorescence on a logarithmic scale is depicted versus excitation power. This figure is adapted from reference [110].

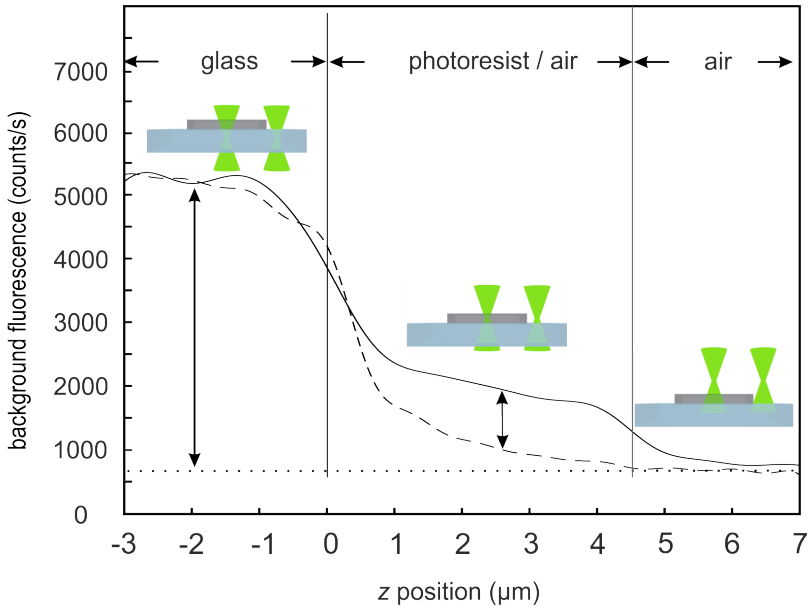


**Figure 4.5: Photoresist with low background fluorescence.** A laser written photoresist cube with 5 µm side length on top of a silica glass substrate is excited by a tightly focused (NA = 1.4) continuous-wave laser at 561 $nm$ wavelength and with 80 µW power. The resulting background fluorescence is recorded by confocal detection versus the $z$-position of the sample with respect to the laser focus. The solid curve shows a $z$-scan through the resist, whereas the dashed curve is a $z$-scan through a glass-air interface for comparison. If the focus lies within the glass substrate ($z < 0$ µm), the detected signal is much larger than the dark count rate (670 counts/s) for the case that the focus lies in air ($z > 4.5$ µm). This figure is adapted from reference [110].

The photoresist recipe consisting of PETA as monomer and 3% (wt) Irgacure 819 as photoinitiator obtained from the last experiment is used here. But in order to solidify the photoresist for fixing the NDs in the photoresist (referring to Section 3.3), additional acetone dissolved PMMA in the photoresist with the volume ratio of 7:3 is added. After quick evaporation of the acetone, the photoresist turns to be solid. In such photoresist, the quantum emitters can be spatially fixed.

Here, the fluorescence intensity versus the excitation power is compared between this home-made photoresist with SU-8 (Microchem Corp), IPG (Nanoscribe GmbH) and Ormocomp (micro resist technology GmbH) as shown in Figure 4.4. Four kinds of photoresist are drop-casted on the segmented glass substrate as described in the last section. Afterwards, square-shaped areas with 10 µm side length and 6 µm height are exposed and polymerized by our lithography setup. Next, the setup is switched to the excitation laser at 561 nm wavelength and locate its focus within the photoresist volume and record the fluorescence. The excitation laser is focused above the glass

surface into the polymer blocks and keep the laser on with a power of 2 mW to bleach the fluorescence to a steady state (the similar bleaching behavior as in Figure 4.2). For different polymers, the bleaching time varies. Nevertheless, in our experiment, 5 mins are sufficient for all polymer structures. After quenching, the fluorescence signals are recorded and the focus position is fixed at the same position in the polymer while gradually increasing the excitation laser power from 0 to 1.2 mW. From Figure 4.4 one can see that even though an additional part of PMMA is added, the home-made photoresist shows fairly low fluorescence then other commercial ones.

To get an intuitive concept of the fluorescence level, the fluorescence from the polymerized photoresist recipe is compared with the glass substrate as shown in the experiment of Figure 4.5. One polymer square is written with the same procedure as described above. In this experiment, the piezoelectric stage moves twice: at the first time the piezoelectric stage moves such that the laser focus moves up from inside the glass gradually through the polymer and then to the air; while at the second time, the piezoelectric stage first moves the polymer block away and the same trajectory from the glass substrate directly to the air is repeated. Such that the $z$-scan experiences no polymer block. The process is depicted by the inset. The laser power used here is 80 μW. The background fluorescence count rate from the photoresist of 1000 count/s (difference between solid and dashed curves) is about six times smaller than that of the glass substrate.

As a conclusion, the fluorescence of some photoresists commonly used for DLW is inspected in this chapter. The achieved recipe (PETA as monomer, Irgacure 819 as photoinitiator and PMMA as the solidified agent) exhibits low fluorescence intensity in both un-polymerized and polymerized forms. This low-fluorescence property provides a remarkable signal-to-background ratio environment for the single-photon source experiment enabling effectively localizing and characterizing single-photon sources embedded in 3D polymer micro-structures.

# 5. Enhancing photon collection efficiency from single NV centers by hybrid antennas

The controlled and effective extraction of photons from single-photon sources is an important task in quantum optics. As described in Section 2.3, confocal fluorescence microscopes are commonly used to detect the fluorescence from NV centers. For a free-standing dipole, the emission to the upper and lower half-space is identical due to the isotropic surrounding. This limits the collection efficiency using confocal fluorescence microscopy to a maximum of 50%. Theoretically, nearly all photons emitted from a single dipole could be collected using a 4Pi microscope [121]. Compared with a standard confocal fluorescence microscope with one objective lens, a 4Pi microscope employs an additional high NA objective lens to boost the total numerical aperture. However, this method requires an impeccable alignment of two focal volumes [121].

In most cases, the dipole is very close or attached to the interface between the glass substrate beneath and some other material (air or photoresist in this work) above. The emission pattern is modified such that the intensity is stronger in the denser medium [122]. It is naturally good for the collection efficiency at first glance if one collects photon beneath the glass substrate and the upper material has lower refractive index such as air. But in this case, maximum of the emission pattern is off-axis with a large angle leading to a crucial experimentally dependency of a high NA collection objective lens [123].

In this work, nano-antennas for the efficient redistribution of the NV center emission pattern in a favorable way is introduced. In a first step, NV centers are on-chip localized using pre-fabricated markers and characterized under a confocal fluorescence setup with an integrated HBT. In a second step, parabolic or hemispherical shape solid mirrors as micro-antennas are fabricated at the previously determined NV center positions. With such antennas, ultra-bright emission from NV center is collected under both confocal and non-confocal detection scheme.

## 5.1. Hybrid parabolic antennas

In an ideal case, most of the emission from NV centers is directed to the desired direction with a rather small NA. In this case, the emission can be effectively coupled to low NA on-chip optical components. Many groups are working on this problem. A recently reported approach employs sub-wavelength diamond nano-posts with a silver film as resonators as well as grating structures to improve the collection and radiation efficiencies. Rishi N Pate *et al.* experimentally demonstrated the reduced detection angle by coupling the NV center emission into optical waveguides and fibers [124]

[125]. Furthermore, bullseye gratings have been utilized to efficiently redistribute the NV fluorescence into low numerical aperture modes [126].

The idea of micro-size parabolic mirrors has been previously used by W. P. Ambrose *et al.* to effectively collect light from single molecules [130]. The parabolic mirrors are previously widely applied in scanning near-field microscopes [127], ion-traps [128] and cathodoluminescence setups [129] to eliminate the geometry restrictions of the experimental setup. In this chapter, a reliable approach to fabricate parabolic micro-mirrors as antennas to enhance photon collection with a smaller NA is demonstrated. Polymer parabolic structures are fabricated with the DLW and pre-fabricated NV centers are integrated at the foci. With depositing of the metallic reflection layer, the parabolic shape antenna is formed. The NV fluorescence intensity collected from such integrated system exhibits ultra-high single-photon saturation count rate and low emission numerical apertures. Moreover, the fabrication approach has a high yield and is reliable.

### 5.1.1. Experimental methods

The fabrication process is shown in Figure 5.1. On a cleaned glass substrate surface, a two-dimensional polymer marker grid is written by DLW to mark the relative positions of NV centers. The marker grid is fabricated with a photoresist consisting of PETA as the monomer and 2% weight ratio of 7-diethylamino-3-thenoylcoumarin (DETC) as the photoinitiator. This resist exhibits a relatively high fluorescence enabling the recognition of the grid in the confocal fluorescence scan afterwards. After the development process (the developing procedure is described in Section 2.4.3), an aqueous suspension of NDs is spin-coated onto the sample. NDs are firmly stuck on the glass surface with fixed positions with respect to the grid markers. The prepared sample is examined under the laser scanning confocal fluorescence microscope. Within the fluorescence map, the NV center candidates are inspected by the second-order correlation measurements using the HBT setup (see Section 2.1.4) to confirm their single-photon emission. Locations of NV centers with relatively high count rates and distinguished $g^{(2)}(0)$ values close to $0$ are recorded. In our work, six single NV centers with $g^{(2)}(0) < 0.5$ are characterized and recorded.

In the next step, another photoresist is spin-coated onto the sample. This photoresist consists of PETA as the monomer and Irgacure 819 as the photoinitiator. The sample is precisely moved on the piezoelectric stage to the recorded relative positions such that the pre-characterized NVs can be individually recognized and localized again. With the recorded locations of the NV centers as focal points, solid parabolic lenses with diameters of $10\ \mu m$ are fabricated by DLW. The polymer structures emerge after the development procedure (see Section 2.4.3).

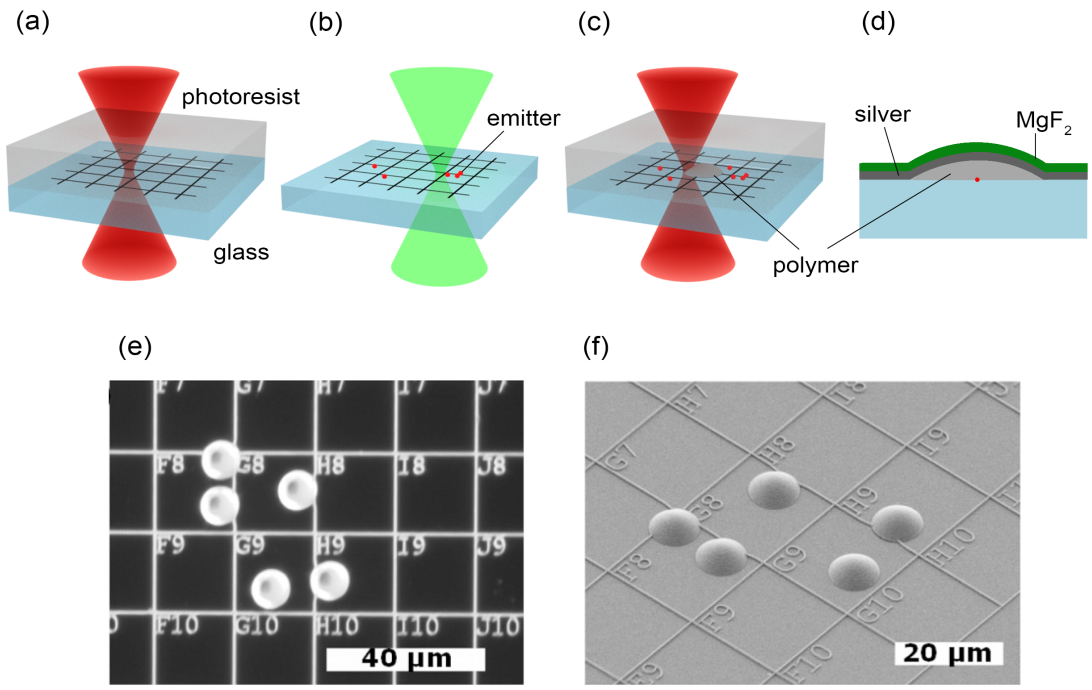


**Figure 5.1: fabrication of parabolic micro-antennas.** Panels **(a)**–**(d)** show a schematic of the fabrication process. **(a)**, In the first step, a polymer marker grid is fabricated with DLW. Subsequently, as shown in **(b)**, NDs are spin-coated on the sample, followed by a localization and pre-characterization process. **(c)**, In a third step, the sample is covered with a layer of photoresist and is subjected to a DLW process for the parabolic polymer structure fabrication at the positions of the pre-characterized NV centers. **(d)**, After the non-polymerized resist is removed in the development process (see Section 2.4.3) a silver reflection layer followed by a $MgF_2$ cover layer for protection are added by the electron-beam evaporation. In this way, a parabolic mirror aligned to one single ND is fabricated. Panel **(e)** shows an optical dark-field image of the laser-written paraboloids and the marker grid before evaporation of the reflective silver film. Panel **(f)** is a scanning electron micrograph of the structures after the fabrication process is completed. Panels **(e)** and **(f)** are adapted from [132].

Parabolic mirrors are formed by covering the solid parabolic lenses with a reflection layer of 100 nm thick silver and subsequently a 30 nm thick magnesium fluoride ($MgF_2$) protection layer by means of electron-beam evaporation. Figure 5.1 (d) depicts the layout of the structure. The final structures with marker grids are inspected under the optical microscope in the dark-field mode and scanning electron microscope as presented in Figure 5.1 (e) and (f) respectively.

### 5.1.2. Experimental results

The purpose of introducing the parabolic mirror is to reshape the angular dependence of the fluorescence emission from the NV centers and thus to enhance the collection efficiency. The fluorescence emission saturation of the embedded NV center is measured upon increasing excitation laser power. Also, intensity measurements in the back focal plane of the objective are presented in the following, showing the resulting angular dependence of the fluorescence emission. Characterization experiments described below is performed by Dr. Andreas Wolfgang Schell.

A $532\,\mathrm{nm}$ cw laser (GL532, SLOC Lasers) is used to pump the NV centers. With the help of the recorded relative positions to the marker grids, NV centers are efficiently found again on the substrate. Emission photons are collected by an objective lens with $\mathrm{NA} = 1.35$ (UPlanSApo 60XO, Olympus). The second-order correlation measurement is carried out in an integrated HBT setup (Section 2.1.4) where a 50/50 beam-splitter is used in the beam path. In each of the two paths, light is then focused into an avalanche photodiode (APD, Perkin Elmer SPCM ARQH-14) for fluorescence detection.

In Figure 5.2 (a), a fluorescence saturation curve from one NV center in a parabolic-mirror antenna is shown. In the experiment, the collected fluorescence intensity is measured upon increasing excitation laser power. In this case, a pinhole is used to suppress the background intensity. The black dots indicate the total measured signal, while the red ones refer to the fluorescence signal with the background signal subtracted. Also, the saturation dependence of three-level systems (Section 2.2.1) is fitted to the measurement data (solid lines). The saturation fluorescence intensity of this NV center is reached at $109\,\mu\mathrm{W}$ excitation laser power. The inset demonstrates the corresponding second-order correlation measurement results with $g^{(2)}(0)$ below 0.5, which indicates the preservation of single photon nature. The use of the confocal pinhole has two effects: on the good side, it suppresses the background light intensity, but it also blocks most of the fluorescence light of the embedded NV center, which is redirected by the parabolic-mirror antenna.

After removing the pinhole, the saturation curve is shown in Figure 5.2 (b). It shows a clear enhancement of the emission collection from the integrated system when compared with Figure 5.2 (a). Similarly, the black data points show the total intensity collected, whereas for the red data points the background signal is subtracted. However, the large separation between the black and the red data set in Figure 5.2 (b) implies that it is unavoidable to collect a large amount of background fluorescence. Due to the interference of the relatively large background light intensity, the saturation count rate can hardly be calculated directly using the data acquired in this fashion. Nonetheless, from the data acquired with the confocal scheme as shown in Figure 5.2 (a), the saturation count rate can be deduced. Compared with a conventional collection method without the parabolic mirrors, the mirror reflects the upper part of the NV center

emission, collimating the light and coupling it into the narrow opening angle of the light-collecting objective lens. The photon collection efficiencies in all six antennas are notably enhanced resulting in an ultra-high recorded photon count rate with values of up to $2\ \mathrm{Mcts/s}$ without correcting for losses in the optics and detector efficiencies, while the average count rate is $1.7\ \mathrm{Mcts/s}$.

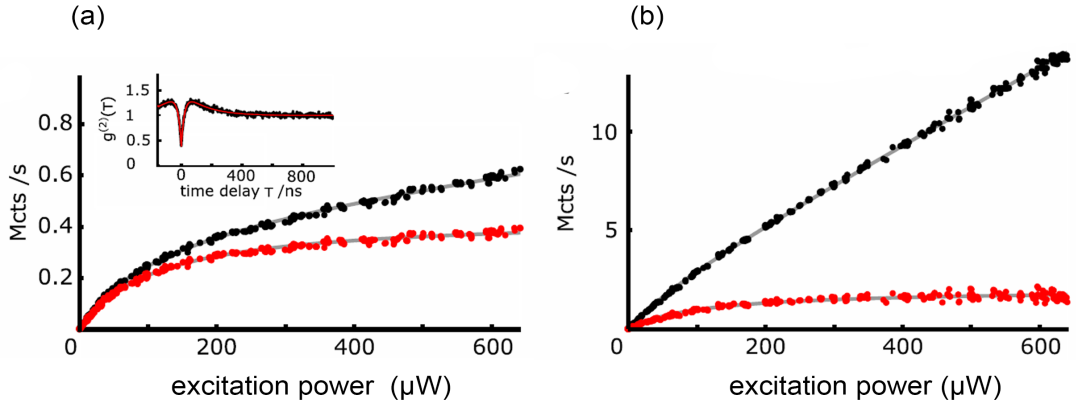


Figure 5.2: **Saturation curves of fluorescence intensity of a single NV center in a parabolic antenna versus increasing excitation power**, **(a)** shows the saturation experiment in a confocal fluorescence microscopy. In this configuration, most of the signal reflected by the mirror is blocked by the confocal pinhole. The black dots are the measured signal and the red dots are the signal subtracted with a linear background fluorescence intensity. The gray curves are fits with the three-level model. The inset shows the second-order correlation measurement data of the photons collected from an NV center under a parabolic antenna in the confocal configuration with the red curve being a fit based on the three-level model. **(b)** shows the detected fluorescence data without the spatial filter. In this case, photons reflected by the mirror are not blocked and thus can be detected. The NV center saturation rate reaches $2.02\ \mathrm{Mcts/s}$. This figure is adapted from [133].

The background fluorescence of the photoresist is always a problem hindering the direct use of the structures as an integrated single-photon source. And at room temperature, the emission spectrum of the NV center overlaps the broad-band background fluorescence and thus is hard to be purified by spectrum filter. This can be solved by either embedded a single photon emitter with much narrow-band fluorescence such as silicon vacancy center in diamond [134] instead of an NV center or combined with an on-chip filter owing the same functionality as the one described in Chapter 7.

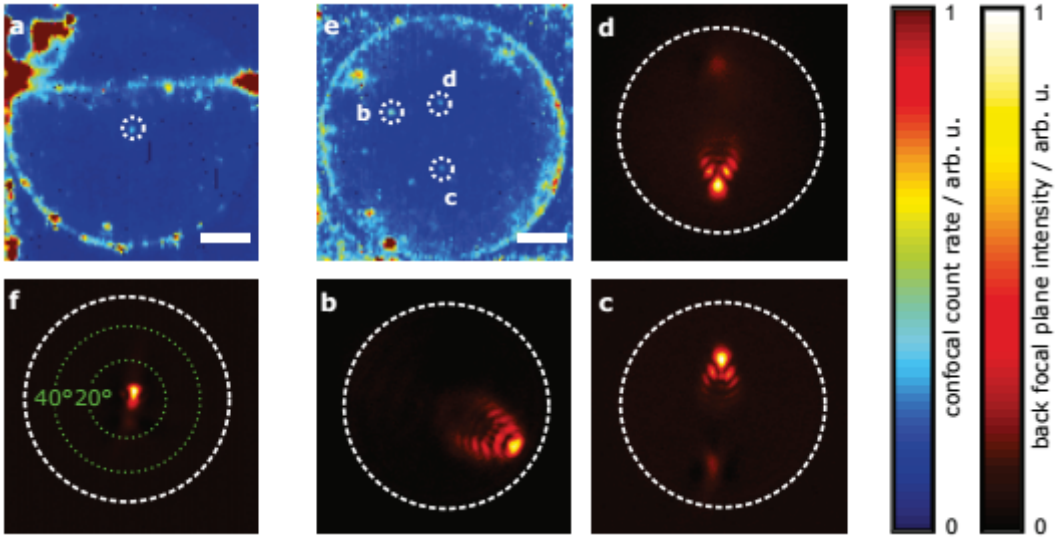


**Figure 5.3.: Confocal and back focal plane images of parabolic mirrors.** In **a**, a confocal scan of a parabolic mirror centered over an ND containing a single NV center is shown. **f** is the corresponding back focal plane image. In the back focal plane, it is visible that the photons reflected by the mirror are directed into a very small solid angle. **e** shows a confocal scan of a parabolic mirror with multiple single NV centers at off-center locations. When these NV centers are excited, the photons reflected are not directed exactly on the optical axis of the collection optics, but under an angle. In this way, beam-steering is achieved. **b c**, **d** show the back focal plane images corresponding to the diamonds marked with b,c,d in panel **b**, respectively. Scalebars in **(a)**, **(b)** are 2 µm. The dashed circles in **(c)-(f)** correspond to the numerical aperture of the collection optics used (NA = 1.35) and the green circles indicate the angle under which the photons are emitted. This figure is from [133].

The back focal plane or rear focal plane of an optical system refers to the transverse plane at the back focus of the system. The object is imaged by the optical system and a 2D Fourier transform is performed by the lens represented by the scalar field on the back focal plane with the expression of:

$$E(x,y) = \iint_{-\infty}^{\infty} E(k_x, k_y)\, \mathrm{e}^{i(k_x x + k_y y)} dk_x dk_y \qquad (5.1.1)$$

where $k_x$ and $k_y$ are the lateral $k$ vectors. Thus, each point of the object is mapped on the $k$-space of the back focal plane which indicates the angular distribution of light intensity. Based on this, the functionality of the fluorescence intensity angular re-directivity by the micro-antenna is proved by measuring the back-focal-plane image of the system and the result is shown in Figure 5.3. A laser scanning confocal fluorescence

experiment is preliminary performed as Figure 5.3 a. Here, the NV center is precisely located at the center of a highly fluorescent circle, which is the boundary of parabolic mirror. Thanks to the high precision of DLW, in all six structures, NV centers are all found at the desired position relative to parabolic antennas. The high fluorescent line crossing the parabolic antenna denotes the marker grid fabricated using the different photoresist. Besides, a similar parabolic antenna with three NV centers at deflected planar positions is fabricated as indicated in Figure 5.3 e. The white dotted circles indicate the pre-characterized NV center. The corresponding back-focal-plane images are individually depicted in Figure 5.3 b-d.

The image background is corrected by subtracting the average intensity around NV centers. In this experiment, the same $532\ \mathrm{nm}$ laser is used to excite the NV center. An EMCCD camera (iXon, Andor) is placed on the back focal plane to record the fluorescence intensity field pattern. By analyzing the extent of the peak in the back focal plane, it is found that the photons coupling into the parabolic antenna are re-directed into a smaller solid angle with a numerical aperture smaller than $0.2$. In the case of an isotropic emission, the re-directivity is $16\ \mathrm{dB}$. Such integrated design with high directing capability can be utilized in cases where the optical setup is restricted such as in the cryogenic environment where the background influence can be remarkably reduced by filtering out the light in all spectrum expect for the zero-phonon line of NV center fluorescence.

## 5.2. Hybrid hemispherical antennas

In the previous section, it is demonstrated that the use of parabolic-shape antennas leads to a count rate reduction in the confocal setup because the pinhole blocks the collimated emission. The pinhole blocks the light not originating from the confocal volume in the sample. One solution is to modify the shape to hemisphere instead of parabola while keeping the emitter at the center. A similar experiment with spherically shaped antennas has been carried out.

### 5.2.1. Experimental methods

An experimental difference with the parabolic antenna is that here the experiment of the characterization and fabrication processes are performed with the integrated setup described in Chapter 3. Firstly, a pre-cleaned glass substrate is spin-coated with NDs aqueous suspension. And the sample is laser raster scanned under a confocal fluorescence microscopy. The single-photon source is sorted out with the HBT setup (see Section 2.1.4). Five single NV centers with high quantum emission efficiency are picked and characterized.

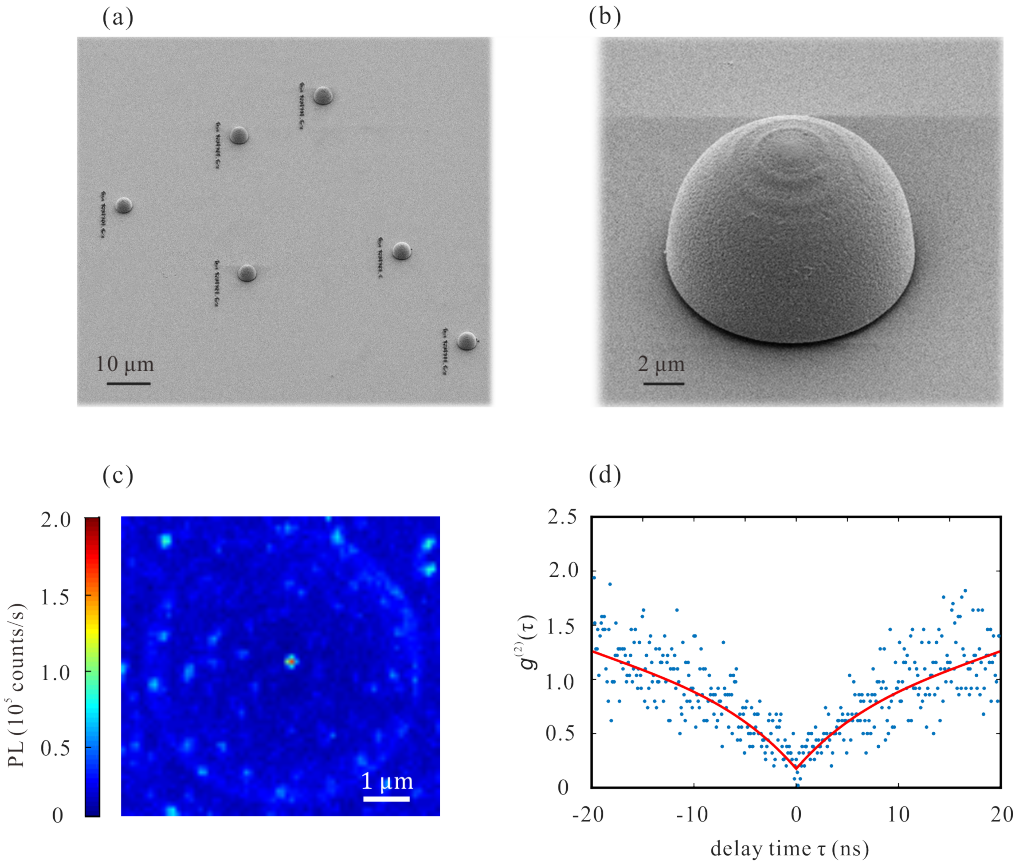


**Figure 5.4**: **Hemispherical mirrors. (a)** shows the scanning electron micrograph of spherical structures layout and **(b)** is a finer scanning of one hemispherical structure with 5µm radius. **(c)** is the scanning confocal fluorescence image of a hemispherical mirror. The bright NV center is clearly detected at the center of the hemispherical. **(d)** is the second-order correlation measurement data of the NV center in the confocal fluorescence microscopy. The red curve fits the data points according to the three-level model and the $g^{(2)}(0)$ shows a value deep to $0.189 < 0.5$ indicating a distinct single-photon emission.

Similar to the previous experiment, a hemispherical structure is written using DLW and afterward covered by a silver layer of 100 nm thickness followed by 30 nm thick $MgF_2$ protective layer. Figure 5.4 (a) and (b) show the scanning electron micrograph of the polymer structure.

For characterisation, the same integrated setup in the mode of laser scanning confocal fluorescence microscopy as in the previous section is used. The excitation laser is focussed on the NV center by the oil-immersed objective lens with 1.4 NA and through the glass substrate. The second-order correlation measurement and the saturation test are performed. Here, to examine the collection enhancement by the antenna, The same NV center is characterized three times in three steps separately: after been spin-coated on the glass substrate, after covered by the photoresist, and after hemispherical antenna fabrication.

### 5.2.2. Experimental results

Figure 5.4 (c) shows the laser scanning confocal fluorescence image of one hemispherical mirror at the layer of the substrate surface with excitation intensity of $300\ \mu W$. The bright spot at the center is the pre-characterized NV center. The single-photon emission is confirmed by the second-order correlation measurement with $g^2(0) = 0.189 < 0.5$ as shown in Figure 5.4 (d) without background correction (referring to Section 2.2.1). Figure 5.5 depicts the PL saturation curves from a single NV center versus the excitation power. The green, red and blue dots are the data measured for three different conditions: the NV center is attached on the bare glass substrate without any covering, covered with photoresist and in a spherical antenna, respectively. Background signals measured at adjacent positions are subtracted from the saturation curves for each case. According to previous work [135], for the case of the bare glass substrate, the emission pattern of dipoles is modified due to the anisotropic dielectric environment and around $60\% - 80\%$ emission photons are guided down into the glass and then collected by the objective lens. Whereas the photoresist layer changes the dielectric environment around the NV center. The emission pattern of an NV center in such environment is nearly isotropic resulting in a redirection of part of the emission to the upper region. Covered with a solid hemispherical mirror, emission to the upper solid angle is supposed to be redirected to the center of the sphere, and thus collected by the objective lens. Theoretically, the enhancement of the photon collection by the hemispherical immersion mirror is a factor of 2 compared with the NV center on the isotropic dielectric environment. Compared with the bare glass case, the enhancement is in the range of $25\%$ to $67\%$ depending on the orientation of the NV center. In this experiment, the saturated fluorescence intensity is calculated by fitting the saturation curve to the three-level model (described in Section 2.2.1). It is found that the hemispherical mirror improves the collection efficiency of the saturated fluorescence intensity of the NV center by a factor of 1.87 (close to 2) compared with the isotropic dielectric environment.

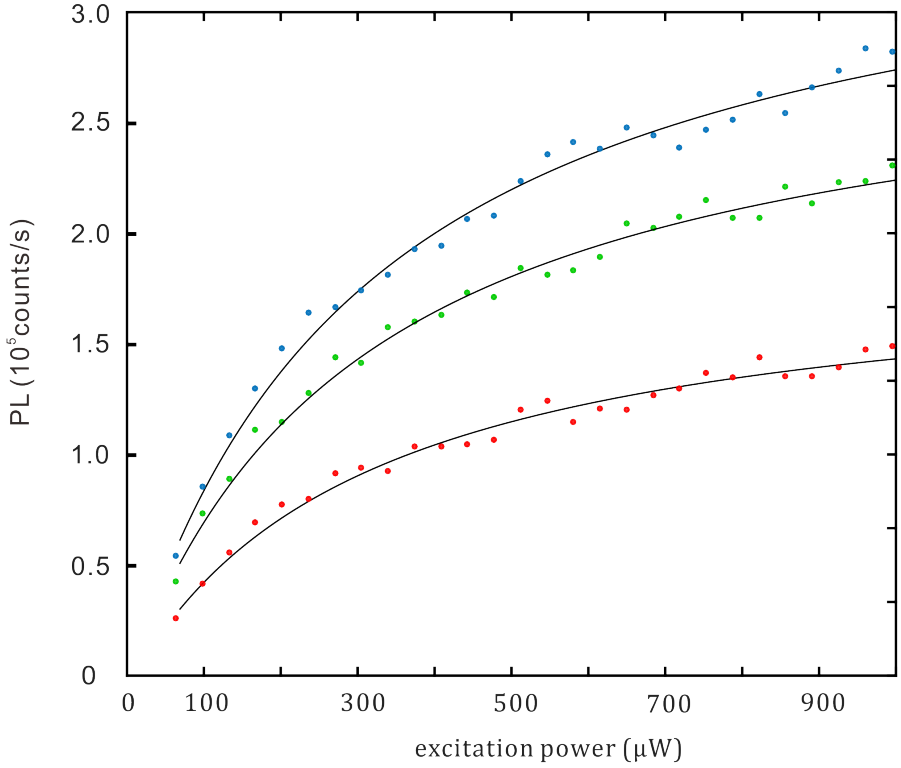


**Figure 5.5: Saturation curves of photoluminescence (PL) intensity versus excitation laser power**. The measured PL for bare glass (green dots), isotropic dielectric (red dots) and spherical mirror (blue dots) are depicted. The black curves are fits according to the three-level model (referring to Section 2.2.1). The environment doesn`t affect the saturation behavior and thus the optical properties of the NV center, but increases the collection efficiency by introducing the hemispherical solid immersion mirror.

In this work, the fabrication process is on the planar localization of NV centers on the substrate. Further improvement of the re-directionality and collimation of the emission is supposed by optimizing the shape of the mirror such that the NV center is designed to locate at a focal point vertically above the surface depending on the design of the mirror. The method is achievable by applying the with solid photoresist SP with volume distributed NV centers as described in Section 3.3. In the following chapters, experiments where arbitrary 3D polymer structures with integrated NV centers at arbitrary desired 3D locations are demonstrated.

This chapter introduces hybrid integrated antennas with two different geometries exhibiting the high capability of re-distribution of the emission pattern from the NV center embedded, and the enhancement of the collection of single photons. Thanks to the flexible and deterministic nature of DLW, the fabrication yield is remarkable with high quality. The flaw of the design is obvious: the background fluorescence intensity restricts the wide application. However, such integrated quantum-unit can be used to

act as an ultra-bright single-photon unit in the cryogenic environment because the background light can be suppressed by a spectral filter. The collection efficiency improvement in the confocal is further improved by changing the shape to a hemispheric that redirects the upper part of the emission pattern to be re-originated from the position of the NV center.

# 6. Integrating pre-fabricated photonic components with single NV centers

In the previous chapter, it has been shown how to integrate NV centers into laser written 3D polymer nanostructures. Due to the nature of the DLW process, the writing scale, speed and resolution are limited. Some nanostructures are fabricated with a finer resolution using other lithography techniques such as electron beam lithography [136-137]. In order to apply single-photon sources in a photonic circuit [138], it is necessary to integrate NV centers into components from another platform on-demand. This chapter presents a method to integrate NV centers with hybrid quantum-photonic structures. As a proof-of-principle demonstration, a single NV center is integrated into a polymer waveguide connecting $Si_3N_4$ photonic circuit devices. Another experiment is to connect tapered fiber ends using a polymer waveguide with an integrated single-photon source.

## 6.1. Photonic circuits with integrated single NV centers

The fabrication of integrated photonic circuits draws wide attraction due to the possibility of realizing a quantum-photonic system with low cost, high efficiency, multiple functionalities, reliable performance and stability [139]. Previous work has demonstrated photonic circuits based on polycrystalline diamond thin films [140]. Reference [141] reports on an approach to fabricate 3D hybrid functional devices with DLW on a pre-fabricated planar optical chip. As an example, an optical waveguide was fabricated for interconnection. The 3D bridge waveguide showed outstanding optical transmission and low insertion loss. Based on the previous work, it is possible to further integrate NV centers into the hybrid system consisting of the polymer waveguide interconnection between pre-fabricated photonic devices.

The substrate used here has the same layout as the one used in reference [141] and produced by Dr. Patrik Rath. The substrate is based on a silicon wafer with a thermally oxidized buffer layer of 2.6 µm thickness. The circuit is made of chemical-vapor-deposited $Si_3N_4$, which is structured by an electron-beam lithography process. The detailed sample preparation process is described in reference [141]. Figure 6.2 (b) shows the optical microscope image of the substrate. The circuit consists of grating couplers that couple incident light to planar waveguides. Y-shaped splitters are used to distribute the light into two paths, one of which is interrupted by a 50 µm gap. In this work, a polymer waveguide will be fabricated to bridge this gap. The planar $Si_3N_4$ waveguides have tapered ends to improve coupling to the interconnecting polymer waveguide.

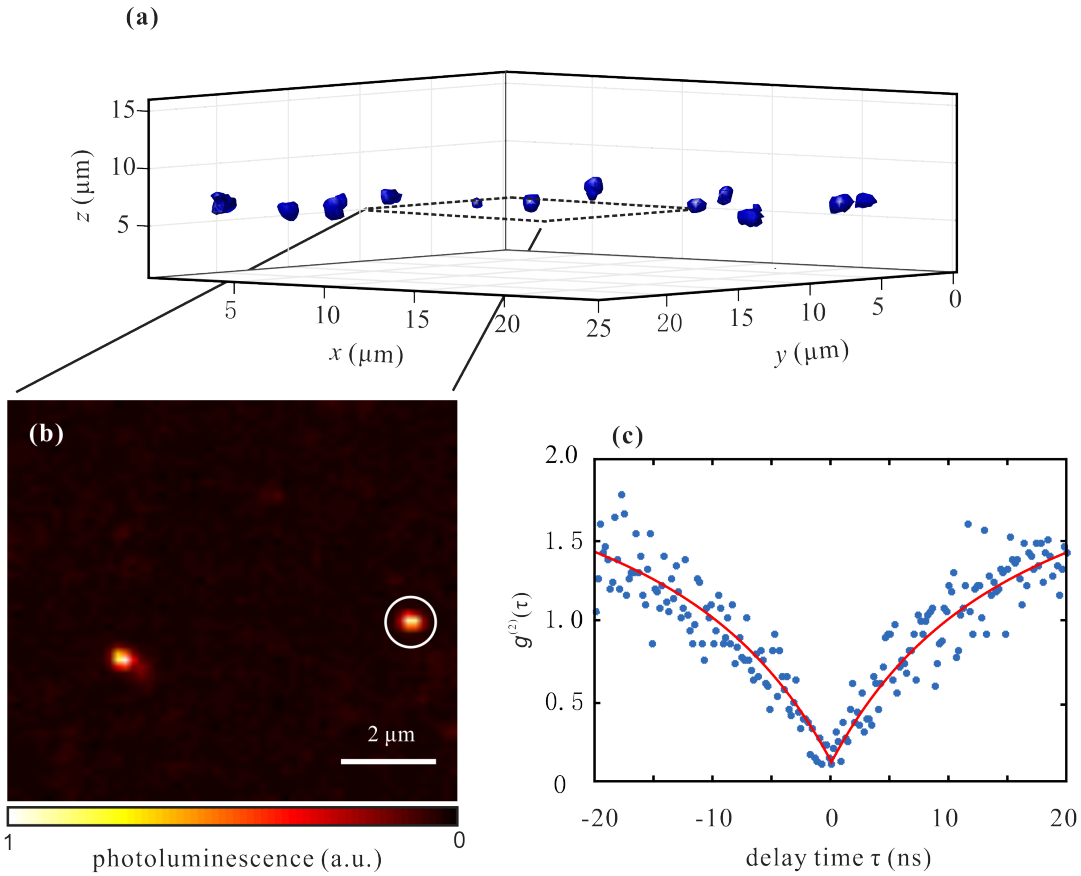


**Figure 6.1: Localization of single NV center.** The $Si_3N_4$ sample is covered with two layers of solid photoresist and one ND layer in between. **(a)** shows the confocal fluorescence volume scan image where iso-intensity surfaces are indicated in blue. Emitters are well confined at the central layer in this case. One planar scanning is shown in **(b)**, where one of the emitters is characterized and circled as a single NV center candidate. The second-order correlation measurement data shown in **(c)** confirms the single-photon property. The red curve fits the data according to the three-level model (details are described in Section 2.2.1). $g^{(2)}(0) = 0.18$ is obtained without any background correction.

## 6.1.1. Experimental methods

The photoresist used in this experiment consists of PETA as the monomer with a 3% weight ratio of Irgacure 819 as the photoinitiator. The photoresist is solidified by mixing PMMA solution in acetone with the volume ratio of 4:1 (details are described in Section 3.3). First, the photoresist is spin-coated on the substrate with 4000 rpm for 1 min as a supporting layer. Subsequently, a suspension drop of NDs in isopropanol is spin-coated at the top with 2500 rpm (details are described in Section 3.3). One additional cover layer of photoresist is spin-coated with 2000 rpm on top. With this fabrication

process, NDs are well distributed and fixed at the height of 6 µm above the substrate surface.

The setup used here is the same as described in Chapter 3. The silicon wafer is only transparent to light at wavelengths above 1100 nm. Therefore, the 780 nm writing laser as well as the 561 nm excitation lasers cannot pass through the substrate. Thus, the sample is fixed on the stage with the structured side facing down to the objective lens. To get a high NA the sample and the objective lens are immersed in a drop of PETA for refractive-index matching. The setup used in this experiment is the same as described in Chapter 3, but with a different objective lens with NA of 1.3 and 100× magnification (Zeiss Objective EC Plan-Neofluar 100x/1.30 Oil M27).

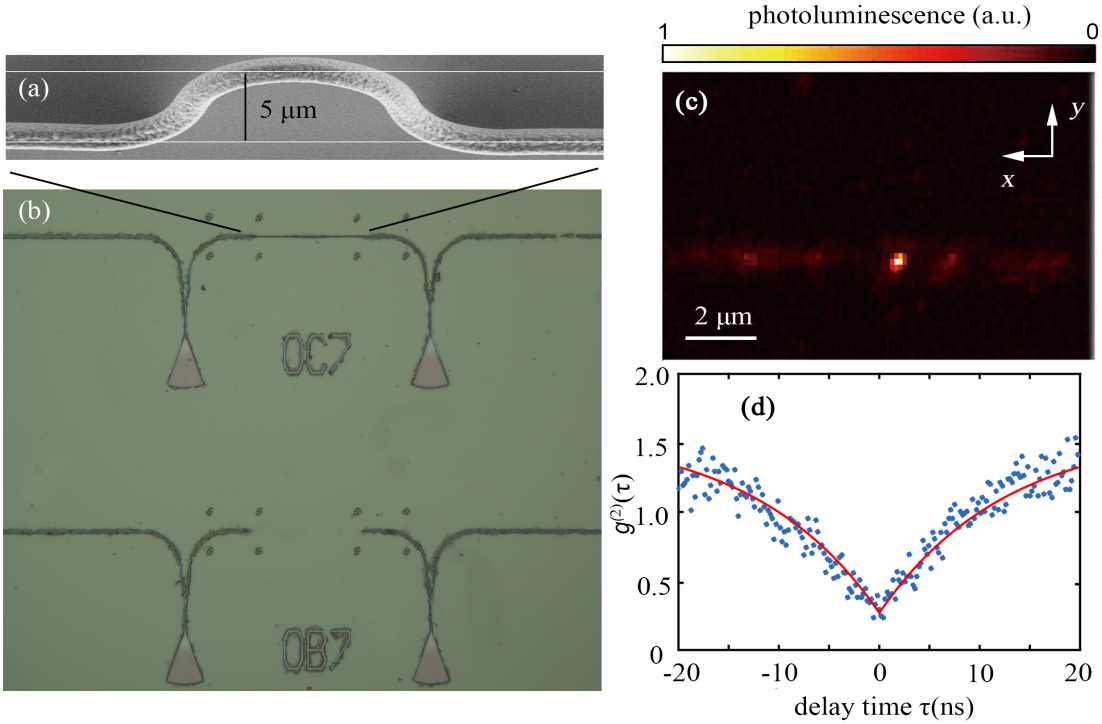


**Figure 6.2**: **Characterization of NV center in the polymer waveguide connecting two $Si_3N_4$ waveguides**. **(a)** shows a scanning electron micrograph of the bending part of the polymer waveguide. An overview of the photonic circuit is shown in an optical micrograph **(b)**. In the upper structure, the $Si_3N_4$ waveguides are connected by a polymer waveguide, while the lower one is the original layout of the $Si_3N_4$ circuit, featuring the 50 µm wide gap. **(c)** is the scanning confocal fluorescence image at the layer where the pre-characterized NV center is embedded. While taking the micrograph, the waveguides are immersed in the monomer PETA to reduce the refractive index difference and thus enhance light outcoupling from the waveguide. The bright spot indicates the pre-characterized NV center. The fluorescent line going through the emitter indicates the polymer waveguide. The single-photon property of the pre-characterized NV center after fabrication is confirmed by the second-order correlation measurement data as

shown in **(d)**. The red curve fits the data according to the three-level model. $g^{(2)}(0) = 0.28$ is obtained without any background correction.

Similar to the experiments in Chapter 5, the sample is raster-scanned in the confocal fluorescence microscope with excitation intensity of $150\ \mu W$ using a pinhole of $15\ \mu m$ diameter. Figure 6.1(a) shows the 3D volume visualization of the sample in the volume of the gap between two waveguide tips. The blue dots indicate detected fluorescent emitters lying $6\ \mu m$ above the surface. Figure 6.1 (b) is a planar laser scanning confocal fluorescence image with a single NV center of interest. The single photon emission is confirmed by the second-order correlation measurement as shown in Figure 6.1(c). Without background correction, $g^{(2)}(0)$ goes down to $0.18$.

The interconnecting process involves three points on the substrate: the locations of two $Si_3N_4$ waveguide ends and the location of the pre-characterized NV center. The integrated setup is based on a commercial microscope (referring to Section 3.1), the back-illumination port of which is used as an entrance port of the writing and excitation laser. For illuminating from the objective side onto the sample, the writing and excitation light are temporally blocked. Instead, a yellow LED illumination unit is fixed on the back-illumination port such that the bottom side of the sample can be illuminated to be seen on the CCD camera. Thereby, the two tapered waveguide tips are roughly localized. Around the tip, the interface between the wafer surface and the photoresist is found by confocal detection of the reflected $561\ nm$ light during a line scan along the vertical direction. Afterward, a planar line scan along the direction perpendicular to the waveguide is performed on the interface. The reflected light remains constant until the laser hits the waveguide, where the reflection light intensity fluctuates. The disturbance depends on the shape of the waveguide and the position of the waveguide. Due to the experiment accuracy and the interference of the noise, the exact position of the tip end with $50\ nm$ width is hard to be specified. Therefore, the line scan is performed at a position $5\text{-}10\ \mu m$ away from the tip. The exact position of the tip is not crucial because the polymer waveguide is designed to start at a position along the waveguide. One more important factor is the tilted angle of the planar waveguide which needs to match the direction of the polymer waveguide fabricated later. Three points along the $Si_3N_4$ waveguide are measured with three-times line scan. The rotation angle is determined by a linear fit to the data. The same value is obtained by evaluating of the fluorescent light in the fluorescence confocal image as shown in Figure 6.2 (c). The measurement is repeated at the other waveguide tip.

The polymer waveguide is designed to overlap part of the $Si_3N_4$ waveguide tip and linearly extend along the pre-calculated direction towards the other waveguide. Along the polymer waveguide, the waveguide gradually bends up to the pre-characterized NV center position and then bends down to the substrate surface. The polymer waveguide emerges after the development process which is the same as explained in Section 3.3. The optical microscope image is shown in Figure 6.2 (b) with Figure 6.2 (a) being a scanning electron microscope image of the bending region.

### 6.1.2. Experimental results

To confirm the existence of NV center in the waveguide, the sample is examined using the same laser scanning confocal fluorescence microscope with excitation intensity of $150\ \mu W$ after the fabrication process. To effectively excite the NV center embedded in the polymer waveguide and extract photons from it, the sample and the objective lens are immersed in the monomer of the photoresist (PETA) to reduce the refractive index difference. The bright spot in the waveguide of Figure 6.2(c) reveals the preservation of the previously located NV center. The second-order correlation measurement on this emitter showed $g^{(2)}(\tau)$ with $g^{(2)}(0) = 0.28 < 0.5$ as shown in Figure 6.2 (d), which is comparable to the one before writing structures shown in Figure 6.1 (c). The weakly fluorescent strip indicates a part of the bending polymer waveguide. Due to the accumulated background fluorescence stemming especially from the $Si_3N_4$ waveguide (which can be expected from the fluorescence map), the excitation light is not coupled into the waveguide and then detect the single-photon property of the out-coupled light.

With the integrated setup, a flexible and straightforward fabrication process is demonstrated to integrate a single NV center into pre-fabricated photonic circuits with a polymer waveguide as the interconnection. Further effort can be made to improve the signal to background ratio fluorescence, possibly by separating the excitation and collection channels of the NV center using the orthogonal orientated waveguides. The presented method can be expanded to single-photon sources other than NV centers and is not limited by the shape of the pre-fabricated photonic structure.

## 6.2. Fiber-integrated single NV centers

In the preceding section, it is demonstrated that the utilization of DLW offers wide possibilities to integrate NV centers into photonic chips. The same method is adopted to interconnect two tapered single-mode optical fiber tips with single NV centers integrated. In the research field of NV centers, coupling of single-photon emission into single-mode fibers draws large attention. The single photons emitted from NV centers can be channeled into a single optical mode and thus the fiber acts as a compact interface with the non-essential optical components eliminated.

Previous works done by the group of Prof. Oliver Benson and Prof. Shigeki Takeuchi have shown a fancy approach to realize an integrated diamond-tapered-fiber system [142-143]. They deposit ND particles on the surface of the tapered fiber, the fluorescence emission from individually excited NV centers is evanescently coupled into the fiber. In this section, an exemplary experiment to robustly integrate single NV centers into tapered fibers using our integrated setup is reported. Here, an interrupted tapered fiber is used. Similar to the previous integration example, a single NV center is pre-localized and characterized in the area of interest, and an optical interconnect is

fabricated by DLW to re-connect the interrupted tapered fiber.

The tapered fiber is produced by Bernd Sontheimer using a single mode fiber with 9 µm core diameter and a cladding diameter of 125 µm. The fiber is gradually pulled by a micropipette puller (P-2000 Sutter Instrument Company CO.) to an hour-glass shape and further to break. Figure. 6.3 (a) shows the optical microscope image of the polymer waveguide connected interrupted fiber. The two fibers are fixed on two linear motor stages with the two tips pointing to each other with a distance of about 15 µm. Under a wide-field optical microscope, the two tips are carefully aligned and then glued onto a common glass substrate using a small drop of photoresist (IP-G from Nanoscribe GmbH). The photoresist drops are polymerized under an UV lamp for 15 minutes. With the two long fibers glued, it is difficult to spin coat the photoresist on the substrate. Therefore, the home-made solid photoresist SP is mixed with the ND-acetone suspension (referring to Section 3.3) and one droplet of the mixture is casted in the area between the fiber tips. During thermal curing (5 minutes at 70°C), the acetone in the mixture evaporates and residual PMMA solidifies the droplet with ND particles fixed in the photoresist.

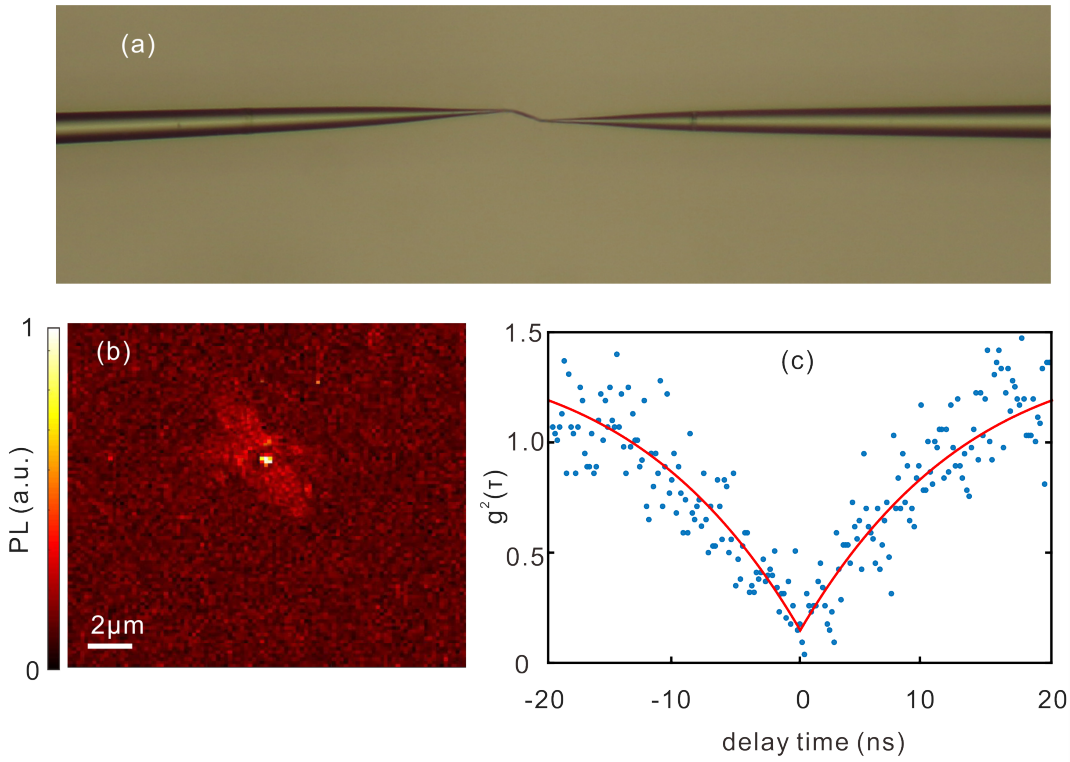


**Figure 6.3**: **Single NV center integrated into tapered fiber. (a)** shows a wide-field optical micrograph of tapered fibers connected by a polymer waveguide using direct laser writing. **(b)** shows a scanning confocal microscope image of a region with an embedded NV center. The polymer waveguide adds relatively high background fluorescence in the area around the emitter. **(c)** is the second-order correlation measurement data of the emitter with $g^2(0) = 0.18 < 0.5$ without

background correction, indicating a good single-photon property.

The sample is fixed on the piezoelectric stage and a droplet of PETA is used to immerse the objective lens and the structure for refractive-index matching. The rough positions of the fiber tips are found by the aid of a CCD camera. Subsequently, the precise location of the fiber tips and their rotation angles are measured with a similar method as described in the last section. But here, the fiber has a $125\,\mu m$ cladding, so the tapered fiber tip is expected to be $65\,\mu m$ above the glass surface. Therefore, when performing the line scanning, the back-scattered light by the fiber is used instead of the back-reflected light on the interface. Also, a second line scanning is necessary to get the vertical position of the fiber tips.

The NV center in the region of interest is found in a laser scanning confocal fluorescence image of the space between two fiber tips. The single-photon emission is determined by the second-order correlation function measured by the HBT setup. Knowing the relative locations of the NV center and the two fiber tips, a polymer waveguide connection is fabricated using DLW from one fiber tip through the NV center to the other fiber tip. The polymer waveguide connection has $2\,\mu m$ long overlapping parts with each fiber tip to ensure good mechanical and optical connections. After the development process, the connection between two tips emerges which is shown in the optical microscope image in the Figure 6.3 (a). Figure 6.3 (b) is the post-scan image with excitation intensity of $150\,\mu W$, where the bright spot is the pre-characterized NV center embedded in the polymer waveguide visible in the fluorescence image as a less fluorescent strip. Figure 6.3 (c) gives the second-order correlation measurement. Due to the lack of ability to more precisely align two fibers, the waveguide bending loss is expected to be large inhibiting further optical characterization through the fiber. Given a technique to well align and fix the relative positions of the fibers, such method is expected to integrate more than one connected-fibers unit with a single NV center on one chip forming an accessible multiple single-photon sources network.

In this chapter, proof-of-principle experiments are demonstrated showing the fabrication of hybrid quantum-photonic chips with 3D polymer optical waveguides connecting pre-fabricated optical components. And at the same time a pre-characterized single NV centers is embedded. The whole process is not limited to the type of emitters and the material of the photonic components used here. An improvement of the performance can be expected when optimizing the shape of the waveguide (diameter and bending radius) and the position of the emitters according to individual existing components to minimize the loses and improve the coupling efficiency.

# 7. 3D Polymer waveguides with integrated single-photon sources

In the previous chapters, a versatile and straightforward integrated setup and several exemplary applications have been demonstrated. This approach allows for the easy and compact integration of single-photon sources with waveguides, fibers and micro-antennas to form a hybrid quantum-optical chip. In this chapter, the integration of pre-characterized single NV centers with functional quantum-photonic components is demonstrated. First, a structure acting simultaneously as an on-chip waveguide, a background filter and a splitter is demonstrated. Afterward, an improved structure to connect several pre-characterized single NV centers in NDs is shown.

## 7.1. Single-photon sources

For practical quantum-photonic chips, the on-demand integration of single-photon sources with individual controllable accesses and high photon collection efficiency is desired [144-145]. However, the background fluorescence intensity influences the single-photon emission in most of the current proposals concerning NV centers, which poses a challenging benchmark on the route to the fabrication of practical, scalable quantum-photonic chips [146]. In this work, single NV centers are integrated into a crossing-waveguide photonic system which allows for selective guiding of the excitation light and the emission from the single-photon source in different waveguide channels. Additionally, the background fluorescence accumulated along the excitation path is separately guided away from the NV center emission channel. Simulations regarding the geometry of the structure are done to optimize the collection efficiency. The detected single-photon count rate from the whole structure is comparable with NV centers in NDs that are excited and measured in a free space configuration.

The idea is proposed by Prof. Dr. Wolfram Pernice. The structure mainly contains two polymer waveguides and is shown in Figure 7.1 (d). The two waveguides have the same half-circle shape but with perpendicularly crossing orientations. A single NV center is embedded in the intersection area. Four waveguide facets are positioned on the substrate surface where light from the far-field is coupled in. All four identical-designed waveguide branches can be used as input or output. When photons emitted by the NV center are collected along the waveguide where the excitation light propagates, the single photons are expected to be immerged in the accumulating background fluorescence originating from the waveguide material. However, in the configuration where the excitation and the collection of the NV center photons is performed through perpendicularly orientated branches of the structure, the accumulated background fluorescence is spatially filtered out. Thus, theoretically the signal-to-background ratio

is less influenced by the length of the propagation path in this approach. The crossing system packages the NV center and creates four accesses as interfaces to either far-field or on-chip optical components. It should be mentioned that the half-circular shape of the waveguides is only for the sake of simplification of the measurements where the light coupling can be performed with the same setup.

### 7.1.1. Experimental method

As described in Chapter 4, the photoresist consists of PETA as a monomer with a 3% weight ratio of Irgacure 819 used as photoinitiator. The photoresist is mixed with the PMMA-acetone solution using a volume ratio of 7:3 for solidification. The NDs suspension is mixed with acetone using a volume ratio of 1:10 and ultra-sonicated for 30 minutes. Similar to the previous work in Section 6.1, two layers of photoresist are spun on the glass substrate with one layer of the NDs spun in between the resist layers. The distribution of NDs in space is controlled such that the sandwich layout restricts the vertical position of NDs to a $1\ \mu m$ thick layer parallel to the substrate avoiding additional unwanted NDs in the waveguides. After rapid evaporation of the acetone, this spun-on mixture becomes solid, such that the locations of all embedded NDs are fixed.

The prepared sample is mounted to the 3D piezoelectric transition stage. The sample is examined using laser scanning confocal fluorescence microscopy with a $561\ nm$ cw laser resulting in a fluorescence map of the NDs layer at a height above the substrate surface of $5\ \mu m$, as shown in Figure 7.1 (a). Each red dot indicates a potential single NV center. A three-dimensional linear scan around the emitter is performed to obtain the precise position of the emitters. The single-photon emission of the NV centers is confirmed by an HBT setup. A typical second-order correlation measurement is depicted in Figure 7.1 (c). A fit to the raw experiment data shows photon anti-bunching with $g^{(2)}(0) = 0.14$ indicating the single-photon emission. All emitters with $g^{(2)}(0)$ values smaller than $0.5$ are documented. In the shown measurement 10 single-photon emitters are found out and localized out of a total of 50 characterized emitters within one hour. Subsequently, the setup is switched to the frequency-doubled femtosecond laser at $780\ nm$ center wavelength for fabrication. With the help of the DLW process, the cross-arch structure is polymerized with the pre-characterized NV center at the waveguide crossing. Afterwards, the samples are rinsed with acetone and water for development. To illustrate the influence of the structure design on the coupling properties and at the same time highlight the advantage of one-step fabrication using DLW, the three structures on the left in Figure 7.1 (e) are fabricated with a larger waveguide diameter.

To explicate the influence of the background fluorescence photons, reference structures are fabricated with the same geometry in an area without any NV centers on the same sample. All structures undergo the same development and examination process.

### 7.1.2. Experimental results

Figure 7.1 (e) is the scanning electron micrograph of a sample with eight cross-arc waveguides, each of them containing a single NV center at the top intersection. This is confirmed by laser scanning confocal fluorescence microscope of this region. The subsequent second-order correlation measurement proves the single-photon emission with $g^{(2)}(0) < 0.5$. Due to the limitations of DLW technique and the inherent aspect ratio of the focus, the structures show an elongated geometry in the vertical direction when the tangent angle of the arc is close to zero with respect to the substrate surface. This effect is more pronounced when the radius of the structure is close to the writing voxel size. The upper most part of the waveguide has a tangent angle of zero and the geometry has a vertical radius of $r_{\perp} = 0.4$ µm and a horizontal radius of $\mathrm{r}_{\parallel} = 0.2$ µm.

The waveguide is designed in a fashion allowing for optimized photon collection efficiency. According to literature on photon collection using optical fibers, or waveguides two parameters need to be addressed for optimization: the bending and the waveguide radius [142] [148-150]. The former one determines the bending loss during the propagation, while the later one determines the light mode coupling to the waveguide. On the one hand, if the waveguide radius is too small, most of the energy flow in higher order modes cannot be coupled and guided in the waveguide. On the other hand, the upper limit of the waveguide radius should prevent the waveguide from becoming multi-modal leading to a decrease in collection efficiency because of the confocal detection scheme. The system is simulated to optimize the waveguide radius. The simulation is performed by Niko Nikolay with JCMwave, which is a full 3D frequency-domain finite-element solver. The wavelength-dependent refractive indices of the substrate (polymer) are taken from the Schott glass (PMMA) data sheet. The index of the surrounding air is taken to be $n = 1$. Two crossed tori with a toroidal angle ranging from 0° to 180° form the structure. This structure is placed on top of a glass substrate and surrounded by air. A $z$-oriented dipole, as shown in Figure 7.2 (a), is placed in the middle of the crossing to simulate the emission of an NV center. In order to numerically detect the guided flux through facets of the arcs, circular regions with a radius of 800 nm are placed on each arc facet (i.e., where arcs and substrate meet). Only downwards directed radiation that crosses these surfaces is considered. To calculate the guiding efficiency, this value is divided by the total flux that leaves the simulated area and enters the isolating perfectly matched layers (PML).

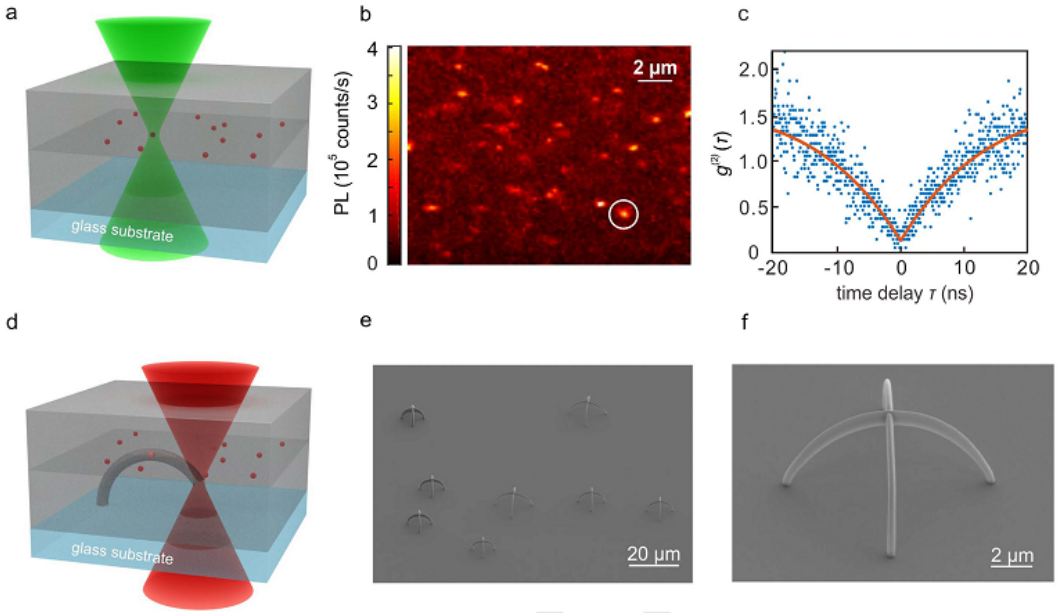


**Figure. 7.1**: **Localization of single-photon emitters and aligned 3D DLW.** **(a)**, Scheme of the photoresist sandwich. First, a 5 µm thick solid photoresist is spin-coated on a glass substrate. Second, NDs containing NV centers suspended in isopropanol are spin-coated on top. Third, another thick layer of solid photoresist is added. As a result, the single-photon emitters are located in a plane parallel to the substrate surface within the volume of the photoresist. At this stage, the sample is optically excited by a 561 nm wavelength continuous-wave laser (green), tightly focused to a diffraction-limited spot, and raster scanned. **(b)**, Resulting confocal photoluminescence (PL) intensity image. **(c)**, Example of a second-order correlation function $g^{(2)}(\tau)$ showing single-photon emission from the encircled point in (b). Excitation power is 100 µW. Similar data is taken from many other emitters. **(d)**, Using femtosecond pulses centered at 810 nm wavelength, 3D microstructures are written, each is aligned with respect to one of the various pre-localized and pre-characterized single-photon emitters. Removal of the unexposed photoresist leads to the final structure. **(e)**, Scanning electron micrograph of several fabricated arc-shaped crossing waveguides. Each crossing contains one pre-characterized single-photon emitter. **(f),** Magnified view of one crossing. The Figure is from reference [110].

The simulation results are displayed in Figure 7.2. Figure 7.2 (a) graphically shows the photon intensity confinement with a fixed emitter at a vacuum wavelength of 680 nm for a fixed arc radius of 5 µm in three cases: waveguide radius smaller than optimal value (left), optimal value (middle) and waveguide radius larger than optimal value (right). Figure 7.2 (b) depicts the collection efficiency versus the waveguide radius and the emission wavelength. The white dashed line indicates the cut an emission wavelength of 680 nm where according to the emission spectrum of the NV centers

the maximum fluorescence intensity is located. Figure 7.2 (c) shows a line plot of this data. The maximum collection efficiency is around 80%. The variation is likely due to interference caused by the reflection at the substrate.

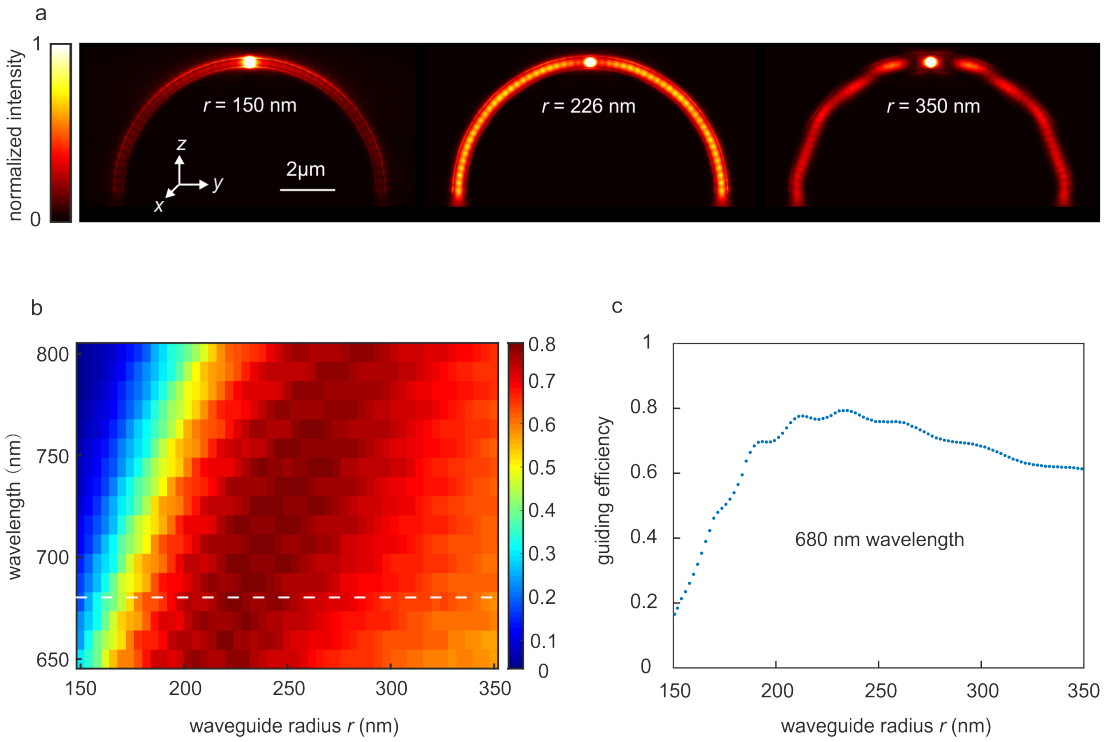


**Figure. 7.2: Single-photon collection efficiency.** Numerical calculations for crossed-arc waveguide structures with arc radius $R = 5\ \mu m$ and waveguide radius $r$. A dipole emitter oriented along the $z$-direction is located in the middle of the crossing. **(a)** shows the Light intensity distribution in a plane parallel to the $yz$-plane cutting through the middle of the waveguide for three different waveguide radii $r$ at a vacuum wavelength of 680 nm. **(b)** shows the guiding efficiency versus waveguide radius and wavelength on a false-color scale. **(c)** is the detailed scan of guiding efficiency versus waveguide radius at a fixed vacuum wavelength of 680 nm. The Figure is from reference [110].

An estimate for the guiding efficiency can be derived from Figure 7.3 (a). The sample is examined upside down under the optical microscope in wide-field reflection mode. The white illumination light couples into the waveguide ports and the guided light couples out from all ports. Figure 7.3 (b) shows the wide-field fluorescence image of a reference structure without a single-photon emitter. Upon pumping into the right port, reduced background PL emerging from the orthogonal waveguide is observed. Figure 7.3 (c) and (e) demonstrate the second-order correlation measurement results of photons extracted from two different waveguide-ports. The second-order correlation function with $g^{(2)}(0) < 0.5$ shows the single-photon emission without background correction

(the correction process is presented in Section 2.2.1). The result with $g^{(2)}(0) = 0.26$ is obtained when collecting photons from the port of a waveguide orthogonal to the waveguide used for excitation. This result is comparable with the $g^{(2)}(0)$ value obtained from free-standing NV centers in the confocal microscope. The filter functionality of the system is remarkable when comparing the result with $g^{(2)}(0) = 0.61$ (without background correction) of photons collected from the port along the same waveguide as used for the excitation. Here the background fluorescence is expected to accumulate along the waveguide until the output port.

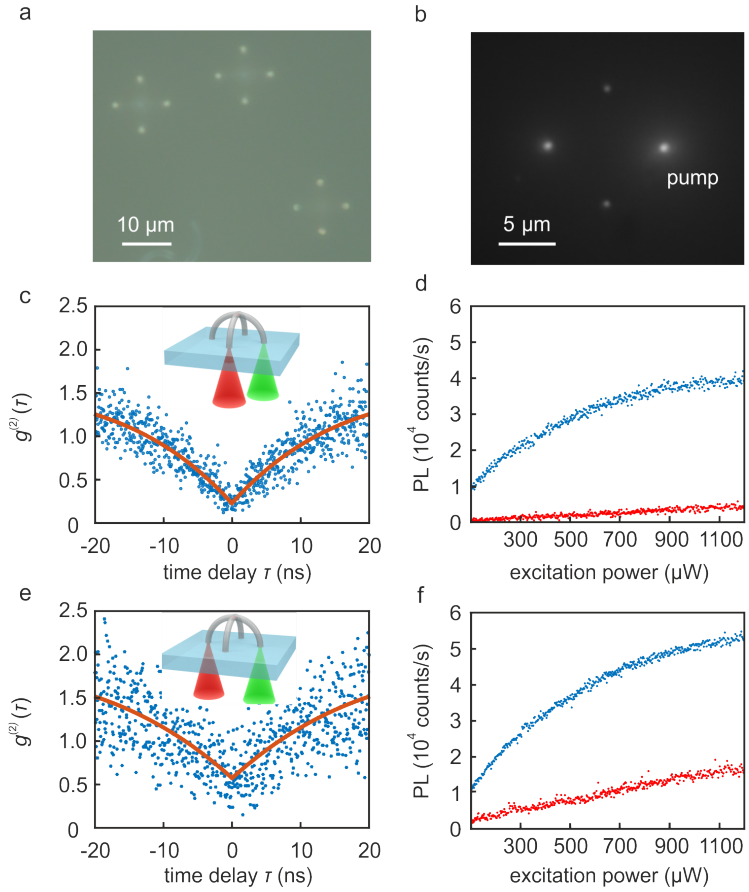


**Figure. 7.3**: **Characterization of single-photon collection from crossed-arc waveguides. (a),** Wide-field reflection-mode optical microscope image under white-light illumination showing light coupled in and out of the four waveguide ports for three different crossed-arc structures. **(b),** Wide-field fluorescence image of a reference structure without a single-photon emitter. **(c),** Structure with a single-photon emitter in the crossing. The blue dots are raw data of $g^{(2)}(\tau)$ measurements, the red curve is a fit to the data. Excitation is at a wavelength of 561 nm and 900 µW incident power. The inset illustrates that detection (red) is from the port corresponding to the waveguide oriented orthogonal to the excitation waveguide (green). **(d),** The PL saturation curves compare the count rates of the structure with (blue) and a reference structure without (red) a single-photon

emitter in the crossing. **(e)** and **(f)** As panels **(c)** and **(d)**, but for detection from the port belonging to the waveguide used for excitation see inset in **(e)**. The Figure is from reference [110].

Figure 7.3 (d) and (f) depict the saturation curves of photoluminescence (PL) intensity versus the excitation laser power. The blue data dots indicate the total photons collected from the integrated structure and the red data dots indicate photons collected from the reference structures which are supposed to be the background fluorescence. It can be seen from the plot that the background fluorescence is filtered out. It is noteworthy that the measurement environment is not optimized for this structure i.e. the excitation laser is coupled into waveguide port with an objective lens, which leads to a large coupling loss and a leakage of the laser during the propagation, which both excite the polymer contributing to the background. An intrinsic origin of the background is from the intersection polymer. It is notable that the fluorescence intensity obtained by subtracting the background from the total photon count in both cases is comparable. This indicates that the orientation of the two dipoles of this NV centers offers almost the same coupling efficiency to two orthogonal directions. Further experiments can be performed to pre-characterize the NV center dipole orientation with the methods described in Section 3.4. Thus, the input ports can be selected to achieve an improved laser coupling efficiency.

## 7.2. Multiple single-photon sources

In the previous section, an integrated structure has been introduced exhibits the abilities to direct excitation light to pump single NV centers, efficiently collect the single-photon emission and filter background light at the same time. When used as a practical sensor for measuring the magnetic field or the mechanical stress, NV centers are required to form an array or a network. The practical, scalable quantum-photonic chip fabrication requires more than one single-photon sources to be integrated. However, on-demand integrating multiple pre-characterized single-photon sources as well as simultaneously and selectively exciting single-photon sources and collecting photons are still challenging tasks. Based on the integrated setup, it is possible to wire up multiple single NV centers to build an integrated quantum-photonic network. Here, waveguides are used for the guiding excitation light and single-photon emission of the NV centers. Similar to the structure in the last section, the design here effectively filters the background fluorescence originating from the polymer structure and thus the single-photon emission is less interfered. The network structure offers multiple choices of inputs and outputs. By choosing proper ones, two work modes can be used: one can either simultaneously excite all NV centers with individual collection channels of single photons from each NV center, or selectively pump any NV center with a uniform photon collection channel. Moreover, such integrated network shows excellent single photon count rate.

### 7.2.1. Experimental methods

Figure 7.4 (a) sketches the structure design. It can be seen as an extended version of the structure introduced in the previous section. It consists of one long backbone waveguide to connect all pre-characterized NV centers. At the position of each NV center, an arc-shaped waveguide is fabricated with the orientation locally orthogonal to the backbone waveguide. All waveguide ports are standing on and facing down towards the substrate surface for the experimental convenient. It is possible to choose any port as either excitation light input or emission light output. Analog to the previous work, each waveguide crossing contains a single NV center and the accumulated background fluorescence stemming from the waveguide material is filtered if excitation and collection of single photons are performed through waveguides that are orthogonal to each other.

The fabrication procedure is similar to the one described in the previous section. It is performed using the same integrated setup. Two layers of solid photoresist with an intermediate layer of NDs are spin-coated on the substrate. In this way, NDs are confined in a layer at the height of $5\ \mu m$ above the substrate (see Section 3.3). For each structure, three NV centers within an area of $30\ \mu m \times 30\ \mu m$ are localized

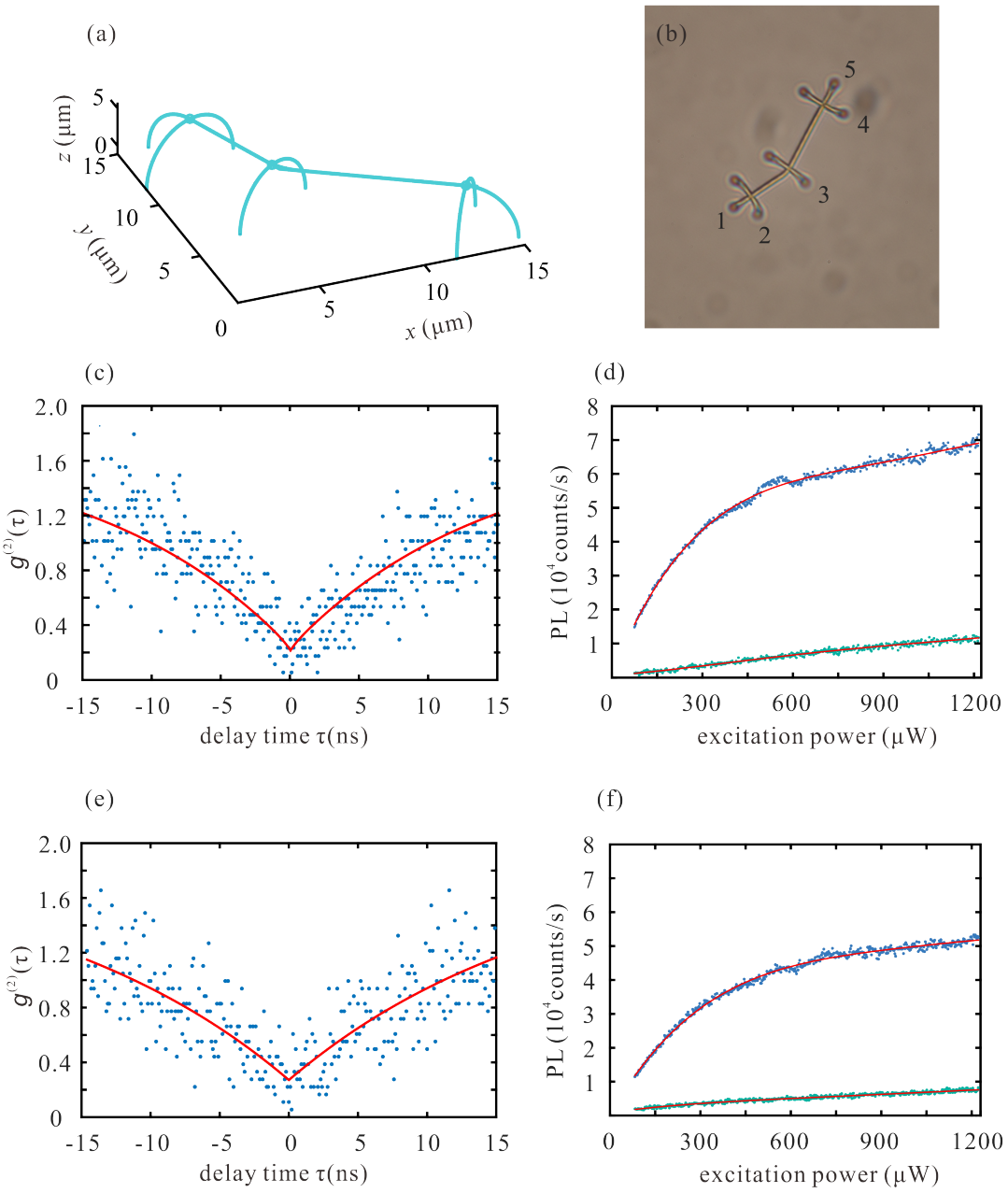


**Figure 7.4**: **Multiple single NV center wired up (a)**, Layout of the system. The backbone waveguide wires up three pre-characterized single NV centers. At each position of the NV center, a waveguide oriented orthogonal to the backbone waveguide is fabricated. **(b)**, A wide-field optical micrograph of the network system, where five ports are labelled. **(c)**, Second-order correlation measurement of the collected photons collected from port 1 with excitation laser feed into port 2. The data is fitted (red curve) according to the three-level model (see Section 2.2.1). **(d)**, PL saturation measurement for photons collected in the case of **(c)**. The blue data points indicate photons collected from the structure with NV centers integrated into the waveguide crossing. The green data points are from the

reference structure using the same measurement scheme. The data is fitted according to the three-level model (red curves). Second-order correlation measurement **(e)** and saturation curve **(f)** of the photons when the excitation laser is coupled into port 1 and the photons are collected from port 3.

and characterized. The shape of the backbone waveguide is based on the locations of the three NV centers. The fabrication of the waveguide starts from the glass surface and bends towards the first NV center with the shape of a quarter circle. The radius equals to the height of the NV center position. Instead of a half-circle shape as in the cross-arc waveguides, the waveguide in this case linearly extends to the second NV center, followed by a gradually bending part to the third NV center and concluded by another quarter-circle shaped waveguide towards the substrate surface.

With each NV center serving as the vertex, three branching waveguides with half-circle shape are fabricated in the plane orthogonal to the local direction of the backbone waveguide. A reference structure without NV centers is fabricated for the sake of background fluorescence studies.

## 7.2.2. Experimental results

The system is proposed to work as an integrated single-photon sources network with multiple choices of light pumping and collection. The structure is characterized based on the collection ability of the single-photon emission under two different operation modes: selective pumping and simultaneous pumping. In the selective pumping mode, the excitation light is coupled in through one of the branch waveguides, and the emission photons are collected from the nearest port of the backbone waveguide. In the simultaneous pumping mode, the excitation is coupled into the long backbone waveguide and the emission photons are collected through ports of the side branch waveguides. Photon collection and excitation are performed using the same objective lens with $\mathrm{NA} = 1.4$ and $100\times$ magnification. Two APDs are used to detect photons and perform the second-order correlation measurement. The cw excitation laser power used in all modes is $1\ \mathrm{mW}$. The details of the far-field photon detection setup can be found in section 3.3.

The ports are numbered in the optical micrograph in Figure 7.4 (b). In the selective pumping mode port 2 of one branch waveguide is used as the excitation input. Photons are collected from the adjacent port 1 of the backbone waveguide. Figure 7.4 (c) shows the second-order correlation measurement data in this case. The fit to the raw data gives $g^{(2)}(0) = 0.24 < 0.5$. Figure 7.4 (d) shows the corresponding PL saturation curve. Similar experiments on the other two NV centers have been performed by coupling excitation light into ports 3 and 4 and photons are collected from port 5 (similar figures are not shown here). In the case of exciting through port 4, $g^{(2)}(0) = 0.25$ is obtained while in the case of exciting through port 3, $g^{(2)}(0) = 0.38$ is obtained. The photons

collected from the three mentioned ports show characters of single-photon emission. The reason for the larger $g^{(2)}(0)$ when exciting through port 3 and collecting from port 5 is mainly due to the long propagation distance of the fluorescence light leading to higher propagation losses.

In the simultaneously pumping mode, the pump laser is coupled into port 1 and the photons are collected from ports 2, 3 and 4 individually. Photons from all three ports show $g^{(2)}(0) < 0.5$. Figure 7.4 (e) shows the second-order correlation measurement of photons collected from port 3 giving $g^{(2)}(0) = 0.31 < 0.5$. The corresponding saturation measurement is shown in Figure 7.4 (f).

In this chapter demonstrates the on-chip quantum-photonic unit and network containing pre-characterized single NV centers. The waveguides guide the excitation light and the emission from NV centers. The orthogonal orientated layout effectively filters the accumulated background fluorescence. In the network design, the input and output ports of the system can be chosen and the excitation of the single-photon sources can be done simutaneously. At the same time, the photons collected from each port show characters of single-photon emission with $g^{(2)}(0) < 0.5$. The fabrication procedure and the photon collection efficiency is not limited by the number of integrated NV centers. This system can be used as a standard single-photon unit or network allowing for integration into quantum-photonic circuits with multiple single-photon sources. And such network system has potential to form a practical nano-magnetic field sensor.

# 8. Summary and outlook

In this thesis, I introduced a method that enables fabrication of 3D hybrid quantum-photonic structures with single-photon sources integrated. Combined with DLW, this unique method enables nearly arbitrary design of quantum-photonic components.

In Chapter 2, concepts and technical basics of this thesis are explained, especially the single-photon source, NV centers in NDs and DLW. The experimental methods are introduced afterwards. The laser scanning confocal fluorescence microscopy enables mapping of single-photon sources in 3D and the single-photon emission is characterized by the second-order correlation measurement using a Hanbury-Brown and Twiss-type setup. The widely investigated single-photon source, NV center in NDs, is introduced next. A three-level modeling of NV centers explains its optical characteristics. Besides exploring the nature of the single-photon source, the powerful tool for fabrication of quantum-photonic components, DLW, is illustrated. Exploiting the benefits of this lithography technique, nearly arbitrary 3D quantum structures can be fabricated.

In Chapter 3, the integrated setup for the localization-selection-lithography approach is introduced. The setup combines the functionalities of laser scanning confocal fluorescence microscopy and DLW technique. The pre-characterizing of NV centers includes 3D fluorescence mapping, estimating the quantum emission efficiency by comparing the fluorescence saturation behaviors and determining the NV center's dipole orientation. These pre-characterization processes help to select an NV center with excellent properties.

Before implementing the main idea of this work, one fundamental problem considering the background fluorescence of photoresists is solved in Chapter 4. Based on tests of different combinations of monomers and photoinitiators, the fluorescence intensity from several commonly used composites of photoresist is investigated. The results lead to a photoresist recipe showing low background fluorescence. Further efforts to improve the signal-to-background ratio can be made by a special design of packaging the source which spatially filters out the background fluorescence photon-stream in Chapter 7.

In Chapter 5, with the aid of the setup and lithographic methods, hybrid quantum-photonic antennas have been fabricated. I demonstrated their ultra-high collection efficiency from a single NV center. This is achieved by redirecting the emission of the NV center into the designed detection direction. The parabolic design is incompatible with the confocal pinhole and the background fluorescence from the polymer under the non-confocal scheme then hinders the practical application. Another design of the hemispherical shape mirror enhances the collection efficiency of NV center with low

background fluorescence in the confocal scheme. The enhancement, comparing with NV centers in an isotropic dielectric environment, reaches a factor of 1.87.

In Chapter 6, I demonstrate a method to integrate pre-characterized single NV centers into pre-fabricated quantum-photonic components. In the first experiment, pre-fabricated $Si_3N_4$ waveguides are connected by a polymer waveguide with a pre-characterized single NV center integrated. The single-photon emission from the NV center is post-characterized and confirmed. In another experiment, single NV centers are integrated into interrupted tapered fibers with a laser written polymer waveguide as interconnection. This method promises the ability to combine quantum-photonic structures fabricated from different platforms with single-photon source integrated and well-aligned in desired positions.

Finally, in Chapter 7, functional 3D quantum-photonic systems are demonstrated. The design combines the functionality of on-chip single-photon guiding, collection and splitting. It suppresses the accumulated background fluorescence from the component structure. A 3D single-photon sources network with multiple integrated single NV centers is illustrated in a second experiment, where single photons from different NV centers are directionally and selectively extracted.

As described above, the task to realize the ideal quantum-photonic circuit is still impeded by many factors. First of all, an ideal single-photon source as described in Section 2.1.3 is hard to achieve so far. Even though NV centers in NDs exhibit excellent optical properties at room temperature, the practical application is restricted by the broad emission spectrum and quantum efficiency relying on the host diamond nanocrystal. A promising alternative are silicon-vacancy centers in NDs which show much higher quantum efficiency within an extremely narrow spectrum band of around $20\,\mathrm{nm}$ at room temperature. In this case, the signal-to-background ratio can be dramatically improved and single-photon sources can be more effectively integrated into waveguides or fibers and thus the characterization and manipulation of single-photon sources will not rely on a confocal setup anymore.

Besides, NV centers are also being used as nano-sensors to precisely detect local magnetic field variations and mechanical stress. By using the approach of integrating NV centers with DLW, NV centers are wired up forming an array or network with well-designed antennas at desired locations. This can be used for detecting nano-magnetic field variations in an optically detected magnetic resonance-type experiment.

Another promising experiment is to work with on-chip single-photon detectors that have been reported recently [151]. I have demonstrated in this work the method to integrate single-photon sources onto a pre-fabricated quantum optical circuit. With the help of an on-chip single-photon detector, a more advanced and completed functional quantum-photonic chip is on the way.

# Bibliography


[1] **Chuang, M. A. Nielsen and I. L.** *Quantum computation and quantum information.* s.l. : Cambridge university press, 2010.

[2] *Photonic quantum technologies.* **O'brien, Jeremy L., Akira Furusawa, and Jelena Vučković.** 12, 2009, Nature Photonics, Vol. 3, pp. 687-695.

[3] **Schrödinger, Erwin.** Discussion of probability relations between separated systems. *In Mathematical Proceedings of the Cambridge Philosophical Society.* s.l. : Cambridge University Press, 1935, Vols. vol. 31, no. 04, pp. 555-563.

[4] *An update on quantum cryptography.* **Bennett, C.H. and Brassard, G.** 1984. In Workshop on the Theory and Application of Cryptographic Techniques.

[5] *On the power of quantum computation.* **Simon, Daniel R.,** 5, 1997, IAM journal on computing, Vol. 26, pp. 1474-1483.

[6] *Quantum computing with molecules.* **Gershenfeld, Neil, and Isaac L. Chuang.** 6, 1998, Scientific American, Vol. 278, pp. 66-71.

[7] *Toward Heisenberg-limited spectroscopy with multiparticle entangled states.* **Leibfried, D., Barrett, M.D., Schaetz, T., Britton, J., Chiaverini, J., Itano, W.M., Jost, J.D., Langer, C. and Wineland, D.J.,.** 5676, 2004, Science, Vol. 304, pp. 1476-1478.

[8] *Super-resolving phase measurements with a multiphoton entangled state.* **Mitchell, Morgan W., Jeff S. Lundeen, and Aephraem M. Steinberg.** 6988, 2004, Nature, Vol. 429, pp. 161-164.

[9] *Multiphoton path entanglement by nonlocal bunching.* **Eisenberg, H.S., Hodelin, J.F., Khoury, G. and Bouwmeester, D.** 9, 2005, Physical review letters, Vol. 94, p. 090502.

[10] *Beating the standard quantum limit with four-entangled photons.* **Nagata, Tomohisa, Ryo Okamoto, Jeremy L. O'brien, Keiji Sasaki, and Shigeki Takeuchi.** 5825, 2007, Science, Vol. 316, pp. 726-729.

[11] *Statistical distance and the geometry of quantum states.* **Braunstein, Samuel L., and Carlton M. Caves.** 22 , 1994, Physical Review Letters, Vol. 72, p. 3439.

[12] *Erasable electrostatic lithography for quantum components.* **Crook, Rolf, Abi C. Graham, Charles G. Smith, Ian Farrer, Harvey E. Beere, and David A. Ritchie.** 6950, 2003, Nature, Vol. 424, pp. 751-754.

[13] *Silica-on-silicon waveguide quantum circuits.* **Politi, Alberto, Martin J. Cryan, John G. Rarity, Siyuan Yu, and Jeremy L. O'brien.** 5876, 2008, Science, Vol. 320, pp. 646-649.

[14] *Three-dimensional quantum photonic elements based on single nitrogen vacancy-centres in laser-written microstructures.* **Schell, Andreas W., Johannes Kaschke, Joachim Fischer, Rico Henze, Janik Wolters, Martin Wegener, and Oliver Benson.** 2013, Scientific reports , Vol. 3 , p. 1577.

[15] *Laser written waveguide photonic quantum circuits.* **Marshall, Graham D., Alberto Politi, Jonathan CF Matthews, Peter Dekker, Martin Ams, Michael J. Withford, and Jeremy L. O'Brien.** 15, 2009, Optics express, Vol. 17, pp. 12546-12554.

[16] *Efficient coupling of photons to a single molecule and the observation of its resonance fluorescence.* **Wrigge, Gert, Ilja Gerhardt, Jaesuk Hwang, Gert Zumofen, and Vahid Sandoghdar.** 4, 2008, Nature Physics, Vol. 1, pp. 60-66.

[17] *A diamond nanowire single-photon source.* **Babinec, Thomas M., Birgit JM Hausmann, Mughees Khan, Yinan Zhang, Jeronimo R. Maze, Philip R. Hemmer, and Marko Lončar.** 3, 2010, Nature nanotechnology, Vol. 5, pp. 195-199.

[18] **C. Cohen-Tannoudji, J. Dupont-Roc, and G. Grynberg.** *Photons and Atoms: Introduction to Quantum Electrodynamics* . s.l. : Wiley-Interscience, New York, 1997.

[19] **Haar, D. Ter.** *The Old Quantum Theory.* s.l. : Oxford, 1967.

[20] *Über einen die Erzeugung und Verwandlung des Lichtes betreffenden heuristischen Gesichtspunkt.* **Einstein, A.** 6, 1905, Annalen der Physik, Vol. 322, pp. 132-148.

[21] *Einstein's Proposal of the Photon Concept—a Translation of the Annalen der Physik Paper of 1905.* **Arons, A. B., and M. B. Peppard.** 5, 1965, American Journal of Physics, Vol. 33, pp. 367-374.

[22] *Coherence and Fluctuations in Light Beams.* **Spiller, W. Martienssen and E.** 12 , 1964, American Journal of Physics, Vol. 30, pp. 919-926.

[23] *Intensity Fluctuations in Light Beams with Several Degrees of Freedom.* **Martienssen, Werner, and Eberhard Spiller.** 12, 1966, Physical Review Letters, Vol. 16, p. 531.

[24] *Single-photon sources.* **Wolf, R. P., and P. P. Crooker.** 68, 2005, Reports on

Progress in Physics, Vol. 5, p. 1129.

[25] *Time distribution of photons from coherent and Gaussian sources.* **Lounis, Brahim, and Michel Orrit.** 1 , 1966, Physics Letters , Vol. 20, pp. 27-29.

[26] *Quantum theory of interference effects in the mixing of light from phase independent sources.* **Fano, U.** 8, 29 8, 1961, American Journal of Physics, Vol. 29, p. 539.

[27] *Generalization of the Cauchy-Schwarz inequality.* **Callebaut, D.K.** 3, 1965, ournal of mathematical analysis and applications, Vol. 12, pp. 491-494.

[28] *The Rabi frequency in optical spectra.* **Knight, Peter L., and Peter W. Milonni.** 66, 1980, Physics Reports , Vol. 2, pp. 21-107.

[29] **Brylevski, Alexey.** *Quantum Key Distribution: Real-time Compensation of Interferometer Phase Drift, Ph.D. thesis, Norwegian University of.* s.l. : Norwegian University of Science and Technology, Trondheim, Norwa, 2002. p. 15.

[30] *Unconditional security of quantum key distribution over arbitrarily long distances.* **Lo, Hoi-Kwong, and Hoi Fung Chau.** 5410, 1999, science, Vol. 283, pp. 2050-2056.

[31] *Quantum interferometric optical lithography: exploiting entanglement to beat the diffraction limit.* **Boto, Agedi N., Pieter Kok, Daniel S. Abrams, Samuel L. Braunstein, Colin P. Williams, and Jonathan P. Dowling.** 13, 2000, Physical Review Letters, Vol. 85, p. 2733.

[32] *Ultrahigh sensitivity single- photon detector using a Si avalanche photodiode for the measurement of ultraweak biochemiluminescence.* **Isoshima, Takashi, Yasushi Isojima, Katsuhiko Hakomori, Kazuro Kikuchi, Katsuya Nagai, and Hachiro Nakagawa.** 4, 1995, Review of Scientific Instruments, Vol. 66, p. 2922.

[33] *Probes for Detection of Specific DNA Sequences at the Single-Molecule Level.* **Jens-Peter Knemeyer, Nicole Marmé , and Markus Sauer *.** 16, 2000, Analytical Chemistry, Vol. 72, pp. 3717–3724.

[34] *Two-photon lidar technique for remote sensing of atomic oxygen.* **T. J. McIlrath, R. Hudson, A. Aikin, and T. D. Wilkerson.** 3, 1979, Applied Optics, Vol. 18, pp. 316-319.

[35] *Room- temperature 1.3- μm optical time domain reflectometer using a photon counting InGaAs/InP avalanche detector.* **Levine, B. F., C. G. Bethea, and J.**

**C. Campbell.** 4, 1985, Applied Physics Letters, Vol. 46, p. 333.

[36] *Time-Resolved Diffuse Reflectance Using Small Source-Detector Separation and Fast Single-Photon Gating.* **ntonio Pifferi, Alessandro Torricelli, Lorenzo Spinelli, Davide Contini, Rinaldo Cubeddu, Fabrizio Martelli, Giovanni Zaccanti, Alberto Tosi, Alberto Dalla Mora, Franco Zappa, and Sergio Cova.** 13, 2008, Physical Review Letters, Vol. 100, p. 138101.

[37] *Proposed entanglement beam splitter using a quantum-dot spin in a double-sided optical microcavity.* **Hu, C. Y., W. J. Munro, J. L. O'Brien, and J. G. Rarity.** 20, 2009, Physical Review B, Vol. 80, p. 205326.

[38] *Quantum key distribution over 122 km of standard telecom fiber.* **Gobby, C., Z. L. Yuan, and A. J. Shields.** 19, 2004, Applied Physics Letters, Vol. 84, pp. 3762-3764.

[39] *Efficient source of single photons: a single quantum dot in a micropost microcavity.* **Pelton, Matthew, Charles Santori, Jelena Vucković, Bingyang Zhang, Glenn S. Solomon, Jocelyn Plant, and Yoshihisa Yamamoto.** 23 , 2002, Physical review letters, Vol. 89, p. 233602.

[40] *A highly efficient single-photon source based on a quantum dot in a photonic nanowire.* **Claudon, Julien, Joël Bleuse, Nitin Singh Malik, Maela Bazin, Périne Jaffrennou, Niels Gregersen, Christophe Sauvan, Philippe Lalanne, and Jean-Michel Gérard.** 3, 2010, Nature Photonics, Vol. 4, pp. 174-177.

[41] *High-frequency single-photon source with polarization control.* **Strauf, S., Stoltz, N.G., Rakher, M.T., Coldren, L.A., Petroff, P.M. and Bouwmeester, D.,.** 22, 2007, Nature photonics, Vol. 1, pp. 704-708.

[42] *Deterministic generation of single photons from one atom trapped in a cavity.* **McKeever, J., A. Boca, A. D. Boozer, R. Miller, J. R. Buck, A. Kuzmich, and H. J. Kimble.** 5666, 2004, Science , Vol. 303, pp. 1992-1994.

[43] *Continuous generation of single photons with controlled waveform in an ion-trap cavity system.* **Keller, Matthias, Birgit Lange, Kazuhiro Hayasaka, Wolfgang Lange, and Herbert Walthe.** 7012, 2004, Nature , Vol. 431, pp. 1075-1078.

[44] *Single photons on demand from a single molecule at room temperature,.* **Lounis, Brahim, and William E. Moerner.** 6803 , 2000, Nature, Vol. 407, pp. 491-493.

[45] *Nonclassical photon statistics in single-molecule fluorescence at room temperature.* **Fleury, L., Segura, J.M., Zumofen, G., Hecht, B. and Wild, U.P.** 6, 2000, Physical review letters, Vol. 84, p. 1148.

[46] *Room temperature single-photon source: single-dye molecule fluorescence in liquid crystal host.* **Lukishova, Svetlana G., Ansgar W. Schmid, Andrew J. McNamara, Robert W. Boyd, and Carlos R. Stroud.** 6, 2003, EEE Journal of selected topics in quantum electronics, Vol. 9, pp. 1512-1518.

[47] *Oriented semiconducting polymer nanostructures as on-demand room-temperature single-photon sources.* **Lee, T.H., Kumar, P., Mehta, A., Xu, K., Dickson, R.M. and Barnes, M.D.,.** 1, 2004, Applied physics letters, Vol. 85, pp. 100-102.

[48] *Single defect centres in diamond: A review.* **Jelezko, F., and J. Wrachtrup.** 13, 2006, physica status solidi (a), Vol. 203, pp. 3207-3225.

[49] *Diamond-based single-photon emitters.* **haronovich, I., et al.** 7, 2011, Reports on Progress in Physics, Vol. 74 , p. 076501.

[50] *Germanium-vacancy single color centers in diamond.* **Iwasaki, T., Ishibashi, F., Miyamoto, Y., Doi, Y., Kobayashi, S., Miyazaki, T., Tahara, K., Jahnke, K.D., Rogers, L.J., Naydenov, B. and Jelezko, F.** 2015, Scientific reports, p. 5.

[51] *Afterpulsing and its correction in fluorescence correlation spectroscopy experiments.* **Zhao, Ming, Lei Jin, Bo Chen, Yao Ding, Hui Ma, and Dieyan Chen.** 19, 2003, Applied optics, Vol. 42, pp. 4031-4036.

[52] *Interferometry of the Intensity Fluctuations in Light. I. Basic Theory: The Correlation between Photons in Coherent Beams of Radiation.* **Brown, R. Hanbury, and Richard Q. Twiss.** 1230, 1957, Proceeding of The Royal Society A, Vol. 242, pp. 300-324.

[53] *Geiger-mode avalanche photodiodes, history, properties and problems..* **Renker, Dieterss.** 567, 2006 , Nuclear Instruments and Methods in Physics Research Section A: Accelerators, Spectrometers, Detectors and Associated Equipment , Vol. 1 , pp. 324-326.

[54] *The question of correlation between photons in coherent light rays.* **Brown R.H. Hanbury, and R.Q. Twiss.** 178, 1956, Nature, Vol. 4548, pp. 1447-1448

[55] *Scanning Confocal Optical Microscopy and Magnetic Resonance on Single Defect Centers.* **Gruber, A., A. Dräbenstedt, C. Tietz, L. Fleury, J. Wrachtrup, and C. Von Borczyskowski.** 5321 , 2012-2014, Science, Vol. 276, p. 276.

[56] *Optical Studies of the 1.945 eV Vibronic Band in Diamond.* **Davies, Gordon, and M. F. Hamer. "Optical studies of the 1.945 eV vibronic band in**

**diamond.** 1653, 1976, Proceedings of the Royal Society of London A, Vol. 348 , p. 285.

[57] *Theory of the neutral nitrogen-vacancy center in diamond and its application to the realization of a qubit.* **Gali, Adam.** 23, 2009, Physical Review B, Vol. 79, p. 235210.

[58] **L., Du Preez.** *Electron paramagnetic resonance and optical investigations of defect centres in diamond.* s.l. : Thesis (Ph.D.)--University of the Witwatersrand, Science Faculty (Physics), 1965.

[59] *Low-temperature microscopy and spectroscopy on single defect centers in diamond.* **Dräbenstedt, A., L. Fleury, C. Tietz, F. Jelezko, S. Kilin, A. Nizovtzev, and J. Wrachtrup.** 16, 1999, Physical Review B, Vol. 60, p. 11503.

[60] *Photon antibunching in the fluorescence of individual color centers in diamond.* **Rosa Brouri, Alexios Beveratos, Jean-Philippe Poizat, and Philippe Grangier.** 17, 2000, Optics Letters, Vol. 25, pp. 1294-1296.

[61] *Stable Solid-State Source of Single Photons.* **Christian Kurtsiefer, Sonja Mayer, Patrick Zarda, and Harald Weinfurter.** 2, 2000, Physical Review Letters, Vol. 85, p. 290.

[62] *Observation and control of blinking nitrogen-vacancy centres in discrete nanodiamonds.* **Bradac, C., T. Gaebel, N. Naidoo, M. J. Sellars, J. Twamley, L. J. Brown, A. S. Barnard, T. Plakhotnik, A. V. Zvyagin, and J. R. Rabeau.** 5, 2010, Nature Nanotechnology, Vol. 5, pp. 345-349.

[63] *Quantum measurement and orientation tracking of fluorescent nanodiamonds inside living cells.* **McGuinness, L.P., Yan, Y., Stacey, A., Simpson, D.A., Hall, L.T., Maclaurin, D., Prawer, S., Mulvaney, P., Wrachtrup, J., Caruso, F. and Scholten, R.E.** 6, 2011, Nature Nanotechnology, Vol. 6, pp. 358–363.

[64] **Balasubramanian G, Neumann P, Twitchen D, Markham M, Kolesov R, Mizuochi N, Isoya J, Achard J, Beck J, Tissler J, Jacques V, Hemmer PR, Jelezko F, Wrachtrup J.** Ultralong spin coherence time in isotopically engineered diamond. *Nature Materials.* 2009, pp. 8(5):383-7.

[65] *Enhanced solid-state multispin metrology using dynamical decoupling.* **Pham, Linh My, Nir Bar-Gill, Chinmay Belthangady, David Le Sage, Paola Cappellaro, Mikhail D. Lukin, Amir Yacoby, and Ronald L. Walsworth.** 4, 2012, Physical Review B, Vol. 86, p. 045214.

[66] *Solid-state electronic spin coherence time approaching one second.* **Bar-Gill, Nir, Linh M. Pham, Andrejs Jarmola, Dmitry Budker, and Ronald L.**

**Walsworth.** 4, 2013, Nature communications, p. 1743.

[67] *Scanning confocal optical microscopy and magnetic resonance on single defect centers.* **Gruber, A., A. Dräbenstedt, C. Tietz, L. Fleury, J. Wrachtrup, and C. Von Borczyskowski.** 5321, 1997, Science, Vol. 276, pp. 2012-2014.

[68] *Sub-optical resolution of single spins using magnetic resonance imaging at room temperature in diamond.* **Shin, Chang, Changdong Kim, Roman Kolesov, Gopalakrishnan Balasubramanian, Fedor Jelezko, Jörg Wrachtrup, and Philip R. Hemmer.** 9, 2009, Journal of Luminescence, Vol. 130, pp. 1635–1645.

[69] *Solid Immersion Facilitates Fluorescence Microscopy with Nanometer Resolution and Sub-Ångström Emitter Localization.* **D. Wildanger, B. R. Patton, H.Schill,L. Marseglia,J. P. Hadden, Sebastian Knauer, Andreas Schönle, John G. Rarity, Jeremy L. O'Brien, Stefan W. Hell, Jason M. Smith.** 44, 2012, Advanced Materials, Vol. 24, pp. 309–313.

[70] *High-sensitivity diamond magnetometer with nanoscale resolution.* **Taylor, J. M., P. Cappellaro, L. Childress, L. Jiang, D. Budker, P. R. Hemmer, A. Yacoby, R. Walsworth, and M. D. Lukin.** 10, 2008, Nature Physics, Vol. 4, pp. 810-816.

[71] *Characterization and application of single fluorescent nanodiamonds as cellular biomarkers.* **Fu CC, Lee HY, Chen K, Lim TS, Wu HY, Lin PK, Wei PK, Tsao PH, Chang HC, Fann W.** 3, 2007, Proceedings of the National Academy of Sciences, Vol. 104, pp. 727-732.

[72] *Dynamics of diamond nanoparticles in solution and cells.* **Neugart, Felix, Andrea Zappe, Fedor Jelezko, C. Tietz, Jean Paul Boudou, Anke Krueger, and Jörg Wrachtrup.** 12, 2007, Nano letters, Vol. 7, pp. 3588-91.

[73] *Tracking the engraftment and regenerative capabilities of transplanted lung stem cells using fluorescent nanodiamonds.* **Wu, Tsai-Jung, Yan-Kai Tzeng, Wei-Wei Chang, Chi-An Cheng, Yung Kuo, Chin-Hsiang Chien, Huan-Cheng Chang, and John Yu.** 9, 2013, Nature Nanotechnology, Vol. 8, pp. 682-689.

[74] *Optical magnetic imaging of living cells.* **Le Sage, D., Arai, K., Glenn, D.R., DeVience, S.J., Pham, L.M., Rahn-Lee, L., Lukin, M.D., Yacoby, A., Komeili, A. and Walsworth, R.L.** 7446, 2013, Nature , Vol. 496, pp. 486–489.

[75] **Rosa Brouri, Alexios Beveratos, Jean-Philippe Poizat, and Philippe Grangier.** Photon antibunching in the fluorescence of individual color centers in diamond . *Optics Letters.* 2000, pp. Vol. 25, Issue 17, pp. 1294-1296.

[76] *Near-field optical microscopy with a nanodiamond-based single-photon tip.* **Aurélien Cuche, Aurélien Drezet, Yannick Sonnefraud, Orestis Faklaris, François Treussart, Jean-François Roch, and Serge Huant.** 22, 2009, Optics Express, Vol. 17, pp. 19969-19980.

[77] **Milonni, Peter.** *The Quantum Vacuum: An Introduction to Quantum Electrodynamics.* s.l. : Academic Press, New York, 1993.

[78] *Heralded entanglement between solid-state qubits separated by three metres.* **Bernien, H., Hensen, B., Pfaff, W., Koolstra, G., Blok, M.S., Robledo, L., Taminiau, T.H., Markham, M., Twitchen, D.J., Childress, L. and Hanson, R.,.** 497, 2013, Nature, Vol. 7447, pp. 86-90.

[79] *The nitrogen-vacancy colour centre in diamond.* **Doherty, M. W., Manson, N. B., Delaney, P., Jelezko, F., Wrachtrup, J., & Hollenberg, L. C.** 1, 2013, Physics Reports, Vol. 528, pp. 1-45.

[80] *Bright fluorescent nanodiamonds: no photobleaching and low cytotoxicity.* **Yu, Shu-Jung, Ming-Wei Kang, Huan-Cheng Chang, Kuan-Ming Chen, and Yueh-Chung Yu.** 127, 2005, Journal of the American Chemical Society, Vol. 50, pp. 17604-17605.

[81] *Molecular-sized fluorescent nanodiamonds.* **Vlasov, I.I., Shiryaev, A.A., Rendler, T., Steinert, S., Lee, S.Y., Antonov, D., Vörös, M., Jelezko, F., Fisenko, A.V., Semjonova, L.F. and Biskupek, J.** 1, 2014, Nature nanotechnology, Vol. 9, pp. 54-8.

[82] *Assembly of hybrid photonic architectures from nanophotonic constituents.* **Benson, Oliver.** 480, 2011, Nature, Vol. 7376, pp. 193–199.

[83] *Single Defect Centers in Diamond Nanocrystals as Quantum Probes for Plasmonic Nanostructures.* **Schell, Andreas W., Günter Kewes, Tobias Hanke, Alfred Leitenstorfer, Rudolf Bratschitsch,.** 8, 2011, Optics Express, Vol. 19, pp. 7914-7920.

[84] *Suitability of nanodiamond nitrogen–vacancy centers for spontaneous emission control experiments.* **Koenderink, Abbas Mohtashami and A Femius.** 4, 2013, New Journal of Physics, Vol. 15, p. 043017.

[85] *Beyond the shine: recent progress in applications of nanodiamond.* **Krueger, Anke.** 34 , 2011, Journal of Materials Chemistry, Vol. 21, pp. 12571–12578.

[86] *Enormously High Concentrations of Fluorescent Nitrogen- Vacancy Centers Fabricated by Sintering of Detonation Nanodiamonds.* **Baranov, Pavel G., Alexandra A. Soltamova, Daniel O. Tolmachev, Nikolay G. Romanov,**

**Roman A. Babunts, Fedor M. Shakhov, Sergey V. Kidalov et al.** 11, 2011, Small, Vol. 7, pp. 1533-1537.

[87] **Zousman, Boris, and Olga Levinson.** *Pure Nanodiamonds Produced by Laser-assisted Technique.* 2011. pp. 21, 12571-12578.

[88] *Narrowband fluorescent nanodiamonds produced from chemical vapor deposition films.* **Neu E, Arend C, Gross E, Guldner F, Hepp C, Steinmetz D, Zscherpel E, Ghodbane S, Sternschulte H, Steinmüller-Nethl D, Liang Y.** 24, 2011, Applied Physics Letters, Vol. 98, p. 243107.

[89] *Surface modification and functionalization of nanostructured carbons.* **Stanishevsky, A., S. A. Catledge, and Y. Vohra.** 2, 2009, Journal of Achievements in Materials and Manufacturing Engineering, Vol. 37, pp. 348-353.

[90] *Three-dimensional microfabrication with two-photon-absorbed photopolymerization.* **Maruo, Shoji, Osamu Nakamura, and Satoshi Kawata.** 2, 1997, Optics letters, Vol. 22, pp. 132-134.

[91] *Fabrication of continuous-relief micro-optical elements by direct laser writing in photoresists.* **Gale, Michael T., Markus Rossi, Joern Pedersen, and Helmut Schuetz.** 11, 1994, Optical Engineering, Vol. 33, pp. 3556-3566.

[92] *Near-field laser parallel nanofabrication of arbitrary-shaped patterns.* **Guo, W., Wang, Z.B., Li, L., Whitehead, D.J., Luk'yanchuk, B.S. and Liu, Z., 2007.** 90, 2007, Applied physics letters, Vol. 24 , p. 243101.

[93] *Fabrication of microfluidic mixers and artificial vasculatures using a high-brightness diode-pumped Nd: YAG laser direct write method.* **Lim, Daniel, Yoko Kamotani, Brenda Cho, Jyotirmoy Mazumder, and Shuichi Takayama.** 4, 2003, Lab on a Chip, Vol. 3, pp. 318-323.

[94] *Photonic metamaterials by direct laser writing and silver chemical vapour deposition.* **Rill, Michael S., Christine Plet, Michael Thiel, Isabelle Staude, Georg Von Freymann, Stefan Linden, and Martin Wegener.** 7, 2008, Nature materials , Vol. 7, pp. 543-546.

[95] *Fundamental improvement of resolution with a 4Pi-confocal fluorescence microscope using two-photon excitation.* **Hell, Stefan, and Ernst HK Stelzer.** 5-6, 1992, Optics Communications, Vol. 93, pp. 277-282.

[96] *Two-Photon Laser Scanning Fluorescence Microscopy.* **Denk, Winfried, James H. Strickler, and Watt W. Webb.** 4951, 1990, Science, New Series, Vol. 248, pp. 73-76.

[97] *Three-dimensional optical data storage in refractive media by two-photon point excitation.* **Strickler, James H., and Watt W. Webb.** 22, 1991, Optics letters, Vol. 16, pp. 1780-1782.

[98] *Photodynamic therapy by nonresonant two-photon excitation.* **Koenig, Karsten, Iris Riemann, and Peter Fischer.** 1999. BiOS'99 International Biomedical Optics Symposium. International Society for Optics and Photonics.

[99] **Young, Robert Joseph, and Peter A. Lovell.** Introduction to polymers. s.l. : London: Chapman & Hall, 1991, p. Vol. 2.

[100] *Mechanisms for enhancement of two-photon absorption in donor–acceptor conjugated chromophores.* **Kogej, T., D. Beljonne, F. Meyers, J. W. Perry, S. R. Marder, and J. L. Brédas.** 1, 1998, Chemical Physics Letters, Vol. 298, pp. 1-6.

[101] *The particle size-dependent photoluminescence of nanodiamonds.* **Chung, P. H., Perevedentseva, E., & Cheng, C. L.** 18, 2007, Surface Science, Vol. 601, pp. 3866-3870.

[102] *Quantum nature of a strongly coupled single quantum dot–cavity system.* **Hennessy, Kevin, Antonio Badolato, M. Winger, D. Gerace, Mete Atatüre, S. Gulde, S. Fält, Evelyn L. Hu, and A. Imamoğlu.** 2007, Nature , Vols. 445, no. 7130, pp. 896-899.

[103] *Negative photoresists for optical lithography.* **Shaw, J. M., Gelorme, J. D., LaBianca, N. C., Conley, W. E., & Holmes, S. J.** 1.2, 1997, xIBM Journal of Research and Development, Vol. 41, pp. 81-94.

[104] **Lakowicz, J. R.** Fluorescence anisotropy. *Principles of fluorescence spectroscopy.* s.l. : springer US, 1999, pp. 291-319.

[105] *Silanization and antibody immobilization on SU-8.* **Joshi, Manoj, Richard Pinto, V. Ramgopal Rao, and Soumyo Mukherji.** 6, 2007, Applied surface science, Vol. 253, pp. 3127-3132.

[106] *Photoactivated nanomaterials for biomedical release applications.* **Sortino, Salvatore.** 2, 2012, Journal of Materials Chemistry, Vol. 22, pp. 301-318.

[107] *Watching the Photo- Oxidation of a Single Aromatic Hydrocarbon Molecule.* **Christ, Thomas, Florian Kulzer, Patrice Bordat, and Thomas Basché.** 22, 2001, Angewandte Chemie International Edition, Vol. 40, pp. 4192-4195.

[108] *Photobleaching kinetics of fluorescein in quantitative fluorescence microscopy.* **Song, Loling, E. J. Hennink, I. Ted Young, and Hans J. Tanke.** 6, 1995,

Biophysical journal, Vol. 68, pp. 2588-2600.

[109] *Three-dimensional multi-photon direct laser writing with variable repetition rate.* **Fischer, Joachim, Jonathan B. Mueller, Johannes Kaschke, Thomas JA Wolf, Andreas-Neil Unterreiner, and Martin Wegener.** 22, 2013, Optics express, Vol. 21, pp. 26244-26260.

[110] *Wiring up pre-characterized single-photon emitters by laser lithography.* **Shi, Q., B. Sontheimer, N. Nikolay, A. W. Schell, J. Fischer, A. Naber, O. Benson, and M. Wegener.** 6, s.l. : 6, 2016, Scientific Reports.

[111] *Room temperature stable single-photon source.* **Beveratos, Alexios, Sergei Kühn, Rosa Brouri, Thierry Gacoin, J-P. Poizat, and Philippe Grangier.** 2, 2002, The European Physical Journal D-Atomic, Molecular, Optical and Plasma Physics,, Vol. 18, pp. 191-196.

[112] **Born, Max, and Emil Wolf.** Principles of Optics. s.l. : Cambridge University Press." New York, 1999, p. 704.

[113] *Inroad to modification of detonation nanodiamond.* **Spitsyn, B. V., J. L. Davidson, M. N. Gradoboev, T. B. Galushko, N. V. Serebryakova, T. A. Karpukhina, I. I. Kulakova, and N. N. Melnik.** 2, 2006, Diamond and Related Materials, Vol. 15, pp. 296-299.

[114] *Surface chemistry and properties of ozone-purified detonation nanodiamonds.* **Shenderova, O., A. Koscheev, N. Zaripov, I. Petrov, Y. Skryabin, P. Detkov, S. Turner, and G. Van Tendeloo.** 20, 2011, The Journal of Physical Chemistry C, Vol. 115, pp. 9827-9837.

[115] **Ho, D. N.** *Nanodiamonds. Applications in biology and nanoscale medicine.* s.l. : Springer, 2010.

[116] *Laser dispersion of detonation nanodiamonds.* **Niu, K. Y., Zheng, H. M., Li, Z. Q., Yang, J., Sun, J., & Du, X. W.** 18, 2011, Angewandte Chemie International Edition, Vol. 50, pp. 4099-4102.

[117] *Effect of nanodiamond surface functionalization using oleylamine on the scratch behavior of polyacrylic/nanodiamond nanocomposite.* **Khalilnezhad, Pardis, Seyed Abdolkarim Sajjadi, and Seyed Mojtaba Zebarjad.** 45, 2014, Diamond and Related Materials, pp. 7-11.

[118] *Longitudinal field modes probed by single molecules.* **Novotny, L., Beversluis, M. R., Youngworth, K. S., & Brown, T. G. (.** 23, 2001, Physical Review Letters, Vol. 86, p. 5251.

[119] *In-situ local temperature measurement during three-dimensional direct laser writing.* **Mueller, Jonathan B., Joachim Fischer, Yatin J. Mange, Thomas Nann, and Martin Wegener.** 12, 2013, Applied Physics Letters, Vols. 103,, p. 123107.

[120] *High-resolution inkjet printing of all-polymer transistor circuits.* **Sirringhaus, H., T. Kawase, R. H. Friend, T. Shimoda, M. Inbasekaran, W. Wu, and E. P. Woo.** 5499, 2000, Science, Vol. 290, pp. 2123-2126.

[121] *Properties of a 4Pi confocal fluorescence microscope.* **Hell, Stefan, and Ernst HK Stelzer.** 12, 1992, JOSA A, Vol. 9, pp. 2159-2166.

[122] *Orientation dependence of fluorescence lifetimes near an interface.* **Kreiter, Maximilian, M. Prummer, B. Hecht, and U. P. Wild.** 20, 2002, The Journal of chemical physics, Vol. 117, pp. 9430-9433.

[123] *Dipole radiation near anisotropic low-permittivity media.* **Memarian, Mohammad, and George V. Eleftheriades.** 142 , 2013, Progress In Electromagnetics Research, pp. 437-462.

[124] *Efficient photon coupling from a diamond nitrogen vacancy center by integration with silica fiber.* **Patel, Rishi N., Tim Schröder, Noel Wan, Luozhou Li, Sara L. Mouradian, Edward H. Chen, and Dirk R. Englund.** 2, 2016, Light: Science & Applications, Vol. 5, p. e16032.

[125] *Efficient photon detection from color centers in a diamond optical waveguide.* **Le Sage, D., Pham, L. M., Bar-Gill, N., Belthangady, C., Lukin, M. D., Yacoby, A., & Walsworth, R. L.** 12, 2012, Physical Review B, Vol. 85, p. 121202.

[126] *Efficient photon collection from a nitrogen vacancy center in a circular bullseye grating.* **Li, L., Chen, E.H., Zheng, J., Mouradian, S.L., Dolde, F., Schröder, T., Karaveli, S., Markham, M.L., Twitchen, D.J. and Englund, D.,.** 3, 2015, Nano Letter, Vol. 15, pp. 1493-1497.

[127] *Tip- enhanced near- field optical microscopy.* **Hartschuh, Achim.** 43, 2008, Angewandte Chemie International Edition,, Vol. 47, pp. 8178-8191.

[128] *Stylus ion trap for enhanced access and sensing.* **Maiwald, Robert, Dietrich Leibfried, Joe Britton, James C. Bergquist, Gerd Leuchs, and David J. Wineland.** 8, 2009, Nature Physics, Vol. 5, pp. 551-554.

[129] *Improved cathodoluminescence microscopy.* **Bond, E. F., Diana Beresford, and G. H. Haggis.** 3, 1974, Journal of microscopy, Vol. 100, pp. 271-282.

[130] *Fluorescence spectroscopy and spectral diffusion of single impurity molecules in a crystal.* **Ambrose, W. P., and W. E. Moerner.** 6306, 1991, Nature , Vol. 349, p. 225.

[131] *Nanofabricated solid immersion lenses registered to single emitters in diamond.* **Marseglia, L., Hadden, J.P., Stanley-Clarke, A.C., Harrison, J.P., Patton, B., Ho, Y.L., Naydenov, B., Jelezko, F., Meijer, J., Dolan, P.R. and Smith, J.M.** 13, 2011, Applied Physics Letters, Vol. 98, p. 133107.

[132] *Laser-written parabolic micro-antennas for efficient photon collection.* **Schell, A.W., Neumer, T., Shi, Q., Kaschke, J., Fischer, J., Wegener, M. and Benson, O.** 23, 2014, Applied Physics Letters, Vol. 105, p. 231117.

[133] **A. W. Schell, J. Kaschke, J. Fischer, R. Henze, J. Wolters, M. Wegener, and O. Benson.** Three-dimensional quantum photonic elements based on single nitrogen vacancy-centres in laser-written microstructures. *Scientific Reports.* 2013, p. 3:1577.

[134] *The twelve-line 1.682 eV luminescence center in diamond and the vacancy-silicon complex.* **Goss, J.P., Jones, R., Breuer, S.J., Briddon, P.R. and Öberg, S.,.** 14, 1996, Physical review letters, Vol. 77, p. 3041.

[135] *Light emission by magnetic and electric dipoles close to a plane dielectric interface. III. Radiation patterns of dipoles with arbitrary orientation.* **Lukosz, W.** 11, 1979, JOSA, Vol. 69, pp. 1495-1503.

[136] *Unidirectional emission of a quantum dot coupled to a nanoantenna.* **Curto, Alberto G., Giorgio Volpe, Tim H. Taminiau, Mark P. Kreuzer, Romain Quidant, and Niek F. van Hulst.** 5994, 2010, Science, Vol. 329, pp. 930-933.

[137] *Controlled addressing of quantum dots by nanowire plasmons.* **Gruber, Christian, Primoz Kusar, Andreas Hohenau, and Joachim R. Krenn.** 23 , 2012, Applied Physics Letters, Vol. 100, p. 231102.

[138] *Diamond electro-optomechanical resonators integrated in nanophotonic circuits.* **Rath, P., S. Ummethala, S. Diewald, G. Lewes-Malandrakis, D. Brink, N. Heidrich, C. Nebel, and W. H. P. Pernice.** 25, 2014, Applied Physics Letters, Vol. 105, p. 251102.

[139] *Application specific photonic integrated circuits through generic integration, a novel paradigm in photonics.* **Muñoza, P., J. D. Doménecha, I. Artundoa, C. Habibc, X. J. M. Leijtensd, T. de Vriesd, D. Robbinsd, J. H. den Bestenb, L. R. Chenc, and J. Capmanya.** 2011, In Waves, Vol. 3, pp. 58-64.

[140] *Waferscale nanophotonic circuits made from diamond-on-insulator substrates.*

**Rath, P., Gruhler, N., Khasminskaya, S., Nebel, C., Wild, C. and Pernice, W.H.P.** 9, 2013, Optics express, Vol. 21, pp. 11031-11036.

[141] *Schumann, M., Bückmann, T., Gruhler, N., Wegener, M. and Pernice, W., 2014. Hybrid 2D–3D optical devices for integrated optics by direct laser writing. Light: Science & Applications, 3(6), p.e175.* **Schumann, Martin, Tiemo Bückmann, Nico Gruhler, Martin Wegener, and Wolfram Pernice.** 6, 2014, Light: Science & Applications, Vol. 3, p. 175.

[142] *Tapered fiber coupling of single photons emitted by a deterministically positioned single nitrogen vacancy center.* **Liebermeister, L., Petersen, F., Münchow, A.V., Burchardt, D., Hermelbracht, J., Tashima, T., Schell, A.W., Benson, O., Meinhardt, T., Krueger, A. and Stiebeiner, A.** 3, 2014, Applied Physics Letters, Vol. 104, p. 031101.

[143] *A nanodiamond-tapered fiber system with high single-mode coupling efficiency.* **Schröder, T., Fujiwara, M., Noda, T., Zhao, H.Q., Benson, O. and Takeuchi, S.** 10, 2012, Optics express, Vol. 20, pp. 10490-10497.

[144] *Integrated photonic sensing.* **Thomas-Peter, N., Langford, N.K., Datta, A., Zhang, L., Smith, B.J., Spring, J.B., Metcalf, B.J., Coldenstrodt-Ronge, H.B., Hu, M., Nunn, J. and Walmsley, I.A.** 5, 2011, New Journal of Physics, Vol. 13, p. 055024.

[145] *Matrix of integrated superconducting single-photon detectors with high timing resolution.* **Schuck, Carsten, Wolfram HP Pernice, Olga Minaeva, Mo Li, Gregory Gol'tsman, Alexander V. Sergienko, and Hong X. Tang.** 3, 2013, IEEE Transactions on Applied Superconductivity, Vol. 23, pp. 2201007-2201007.

[146] *Recent advances on integrated quantum communications.* **Orieux, Adeline, and Eleni Diamanti.** 8, 2016, Journal of Optics, Vol. 18, p. 083002.

[147] *Tapered fiber coupling of single photons emitted by a deterministically positioned single nitrogen vacancy center.* **Liebermeister, L., Petersen, F., Münchow, A.V., Burchardt, D., Hermelbracht, J., Tashima, T., Schell, A.W., Benson, O., Meinhardt, T., Krueger, A. and Stiebeiner, A.** 3, 2014, Applied Physics Letters, Vol. 104, p. 031101.

[148] *Numerical simulations of nanodiamond nitrogen-vacancy centers coupled with tapered optical fibers as hybrid quantum nanophotonic devices.* **Almokhtar, M., Fujiwara, M., Takashima, H. and Takeuchi, S.** 17, 2014, Optics express,, Vol. 22, pp. 20045-20059.

[149] *Efficient channeling of fluorescence photons from single quantum dots into*

*guided modes of optical nanofiber.* **Yalla, Ramachandrarao, Fam Le Kien, M. Morinaga, and K. Hakuta.** 6, 2012, Physical review letters, Vol. 109, p. 063602.

[150] *Efficient single-mode photon-coupling device utilizing a nanofiber tip.* **Chonan, Sho, Shinya Kato, and Takao Aoki.** 4, 2014, Scientific reports.

[151] *High Efficiency On-Chip Single-Photon Detection for Diamond Nanophotonic Circuits.* **Kahl, Oliver, Simone Ferrari, Patrik Rath, Andreas Vetter, Christoph Nebel, and Wolfram HP Pernice.** 2 , 2016, Journal of Lightwave Technology, Vol. 34, pp. 249-255.

[152] *Orientation of adsorbed cytochrome c as a function of the electrical potential of the interface studied by total internal reflection fluorescence.* **Fraaije, J. G., J. M. Kleijn, M. Van der Graaf, and J. C. Dijt.** 5, 1990, Biophysical journal, Vol. 57, pp. 965-975.

# Acknowledgements

At the end, I would like to thank all people who helped me for the completion of this thesis.

First and most of all, I would like to sincerely thank Prof. Dr. Martin Wegener for offering me the opportunity working in his group on this topic. During my whole PhD work, he not only greatly supported my work but also shared his professional knowledge, skills and altitude generously and patiently, which makes this period more valuable in my life.

Next, I would like to thank Prof. Dr. Carsten Rockstuhl for agreeing in co-reviewing my thesis.

I also really express my gratitude to PD Dr. Andreas Naber. He supported me a lot on my work and solved plenty of professional problems emerging in my work theoretically and experimentally.

I would also particularly thank Dr. Joachim Fisher, Dr. Johannes Michael Kaschke and Dr. Andreas Wolfgang Schell. They proposed this topic and greatly helped me when I started this work. Dr. Joachim and Dr. Johannes Michael Kaschke helped with the development of the optical setup and the software. They shared their experience and knowledge which gave me an excellent start of this work.

And, I want to appreciate the cooperation with Prof. Oliver Benson, Bernd Sontheimer, Prof. Dr. Wolfram Pernice, Dr. Patrik Rath, and Niko Nikolay. They shared their ideas with me and collaborated to achieve the results presented in this thesis.

I take this opportunity to record my sincere thanks to all members of Wegener group for all the help during my work. Thanks to all the proof readers, who minimized mistakes in my thesis, Vincent Hahn, Jingyuan Qu, Christian Kern, Frederik Mayer, Martin Schumann, Marc Hippler, Tobias Messer, Andreas Wickberg, Tobias Frenzel, Patrick Müller, Münchinger, Alexander and Köpfler, Julian.

I also want to thank secretaries, Renate Helfen, Claudia Alaya, and Mösle, Ursula for doing the paper work. I also want to thank Johann Westhauser to help me with the technical work. Also, great thanks go to the staff of mechanical workshops and to the electronics workshop, Helmut Lay, Michael Hippe, and Werner Gilde who deal with the computer and the network ensuring the untroubled and advanced working environment.

I thank all of you.